



Process-Oriented Evaluation of Stationary Rossby Waves and Their Impact on Surface Air Temperature Extremes in Dynamical Downscaling over North America

Koichi Sakaguchi¹, Seth A. McGinnis², L. Ruby Leung¹, Melissa S. Bukovsky³, Rachel R. McCrary², Ziming Chen¹, Chuan-Chieh Chang¹, and Yanjie Li⁴

Correspondence: Koichi Sakaguchi (Koichi.Sakaguchi@pnnl.gov)

Abstract. Stationary Rossby waves are a crucial component of the general circulation and play a significant role in regional water and energy cycles, as well as in extreme events. However, process-oriented evaluation for stationary Rossby waves is rarely performed for dynamical downscaling simulations. To close this gap, we evaluate three classes of dynamical downscaling approaches, with a focus on stationary Rossby waves and their impact on surface air temperature over North America during Northern Hemisphere summer. The three classes of models differ in the way large-scale forcing is provided: a limited-area model (LAM) constrained only by lateral boundary conditions, represented by RegCM4 from the North American branch of the Coordinated Regional Downscaling Experiment (NA-CORDEX), a LAM with spectral nudging to maintain consistency in large-scale dynamics with the forcing data, represented by the Weather Research and Forecasting (WRF) model simulation in NA-CORDEX, and a global variable-resolution model with smoothly varying grid spacings, represented by the Community Atmosphere Model version 5.4, with the Model for Prediction Across Scales (MPAS) as its dynamical core (CAM-MPAS). With no constraints on the atmospheric dynamics, CAM-MPAS exhibits several mean biases in the upper-level circulations over the Pacific Coast region: a weaker subtropical jet, a northward-shifted mid-latitude jet, and an overestimated southerly flow. With the lateral boundary constraint alone, RegCM4 also exhibits weaker jets and overestimated southerly winds off the West Coast. Rossby ray theory reveals that those wind biases direct incoming Rossby waves northward. The erroneously routed Rossby waves distort the relationship between the accumulation of wave activity over the US West Coast and surface temperature anomalies over the Southern Great Plains, which emerges approximately four days after the convergence of wave activity flux in the ERA-Interim reanalysis. Furthermore, the response of heatwaves to the extreme wave activity flux is not reproduced by the two models, a serious drawback as a dynamical downscaling framework is expected to connect large-scale forcing to local-scale phenomena. The WRF model employing spectral nudging is largely free from the aforementioned problems. A pair of sensitivity simulations suggests that spectral nudging is the key to improving the dynamics of stationary Rossby waves and their impact on surface air temperature. Our results also demonstrate the effectiveness of Rossby wave diagnostics that allow for realistic background flows for assessing the credibility of dynamical downscaling over North America, where

¹Pacific Northwest National Laboratory, Richland, Washington, USA

²NSF National Center for Atmospheric Research, Boulder, Colorado, USA

³University of Wyoming, Laramie, WY, USA

⁴Institute of Atmospheric Physics, Chinese Academy of Sciences, Beijing, China





incoming Rossby waves propagate through complex circulation patterns before traveling across the continent. Evaluating such process chains — from large-scale Rossby waves to local-scale extreme events — requires accounting for the region's unique dynamical features.

1 Introduction

Rossby waves have the largest spatial scales among the atmospheric waves (1000s–10000s km). Their spatial extent makes it possible to connect tropical convection to mid-latitude weather (Wallace and Gutzler, 1981; Ambrizzi et al., 1995; Branstator, 2014). Rossby waves can be "stationary" by having a phase speed equal to the background winds but in the opposite direction, thus their phase (maxima and minima) becomes fixed in space. Since phase speed is inversely proportional to wavenumber, larger waves tend to have greater phase speed. Some large waves become stationary even within the atmospheric jet streams, where vorticity gradients and strong winds can trap and help the waves travel further (Manola et al., 2013; Branstator and Teng, 2017; Wirth, 2020). Such large, stationary Rossby waves are one of the important drivers for regional climate because their associated momentum and energy fluxes modify regional circulation and atmospheric stability (e.g., Weaver and Nigam, 2008; Hoskins and Woollings, 2015; Teng and Branstator, 2017, 2019; Wills et al., 2019; White et al., 2022). Rigorous evaluations of simulated Rossby waves are thus necessary for establishing confidence in regional climate projections. To this end, this study revisits and evaluates the large-scale circulations relevant to Rossby wave propagation to North America, as well as the physical connection between stationary Rossby waves and regional climate, specifically near-surface air temperature (*tas*).

The heatwave over the Pacific Northwest (PNW) in July 2009 is a good example of a relationship between stationary Rossby waves and *tas* anomaly. This event marked the highest maximum temperature in the record across the region (Bumbaco et al., 2013), until it was exceeded by a more recent heatwave in 2021 (White et al., 2023), which falls outside our study period. A spatiotemporal correlation between the upper-level geopotential height anomaly and the daily *tas* anomaly is evident during this month (Fig. 1d-i). Fig. 1a-c illustrate the flux of wave activity (WA), second-order variability of wind fields associated with Rossby waves (Takaya and Nakamura, 2001) (hereafter TN01). The WA flux delineates the flux of perturbation geopotential height in the direction of the group velocity, which is also associated with a negative momentum transport for the mean circulation (Takaya and Nakamura, 2001, section 4). In other words, ahead of the WA convergence, one sees an increase in the perturbation geopotential height and a reduction in mean wind speeds. The region behind the WA divergence experiences a decrease in perturbation geopotential height and an acceleration of the mean winds.

About two weeks before the most intense heatwave on July 29, the PNW region was under a weakly negative height anomaly (Fig. 1d), but the WA flux had already started converging over the region (Fig. 1a). The flux is dominantly meridionally oriented, flowing out northward from the subtropical eastern Pacific, where intense wave activity flux has been converging from the midlatitude North Pacific. Some WA flux appears to originate from the tropical east Pacific region as well. This southerly flow of WA is not obvious from the geopotential height pattern. The WA flux convergence continued and became more intense over the next ten days, during which a positive geopotential anomaly built up over the PNW region (Fig. 1b,e). In response, a positive tas anomaly has emerged (Fig. 1h). The WA flux convergence over the PNW continued, spreading the positive geopotential





anomaly northward to cover Washington state in the United States and the entire Canadian West coast by July 29 (Fig. 1c,f), when a positive tas anomaly > 6°C has extended over most of the PNW region (Fig. 1i). The effect of WA flux divergence through geopotential changes to tas appears to take approximately six days based on the lead/lag correlation. Figure A1a shows that the linear correlation reaches a maximum value of 0.56 at a lag of six days. The evolution of the upper-level geopotential height anomalies follows the typical condition during heatwave events over the region, with the high anomaly centered over Vancouver Island near the Canada-US border (Fig. 1e,f) (Bumbaco et al., 2013). This circulation structure is a part of the East Pacific-North Pacific pattern that is characterized by a southward-shifted and more intense jet across the Pacific (Bell and Janowiak, 1995).

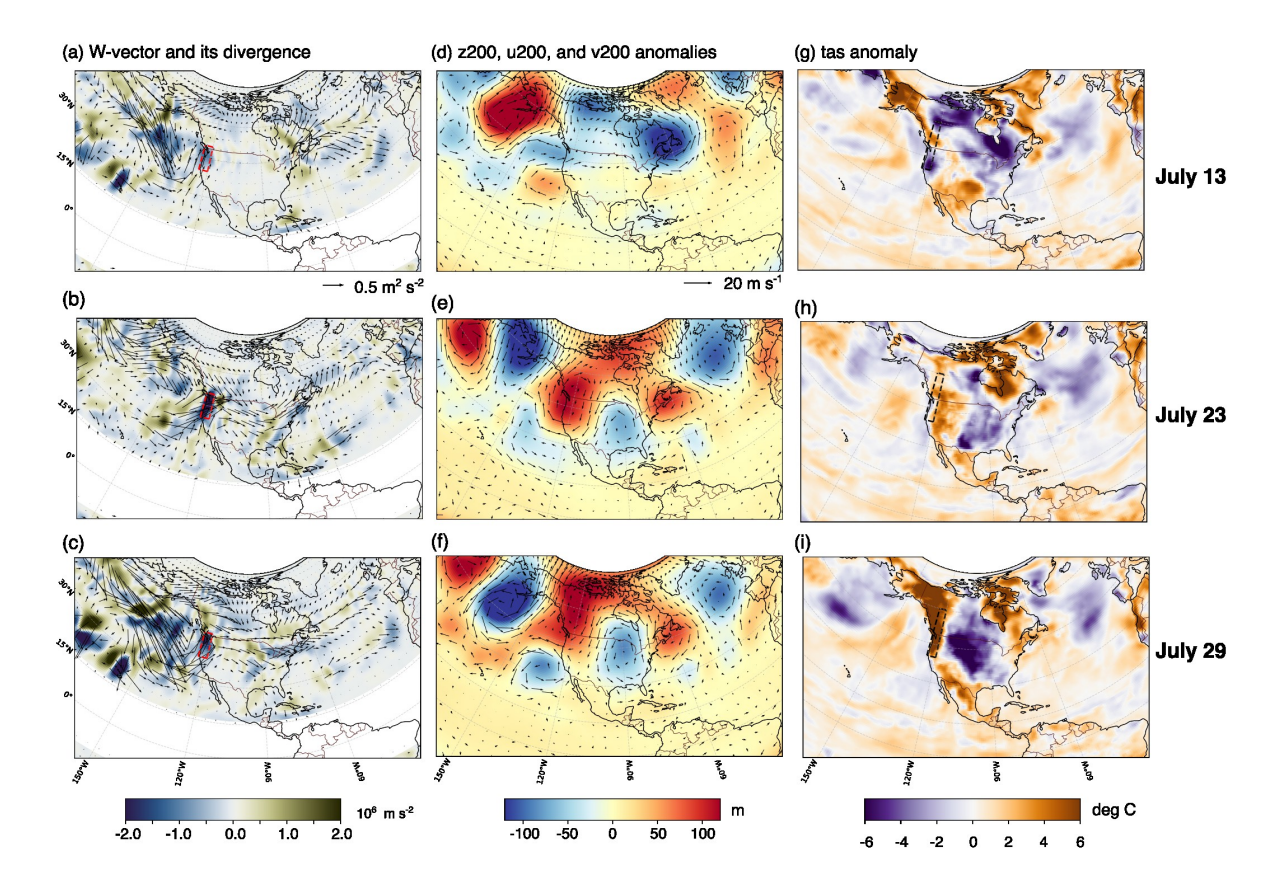


Figure 1. Evolution of stationary Rossby waves and surface air temperature (*tas*) during the 2009 heatwave event: (a-c) the flux (arrows) and divergence (color, blue = convergence, green = divergence) of daily-mean wave activity (WA) flux of derived from the 25-90 day band-passed geopotential height anomalies, (d-f) 200-hPa winds and geopotential height anomalies (25-90 day band-passed), and (g-i) daily *tas* anomaly, all variables from ERA-Interim.

The 2009 heatwave is just one example; significant connections between stationary Rossby waves and regional climate and extremes have been suggested for a long time. Analyzing 30 years of reanalysis data, Schubert et al. (2011) found that merid-



100



ional wind variabilities associated with stationary Rossby waves account for up to 60 % of surface temperature variabilities over large areas in North America. Teng et al. (2013) found that stationary waves with zonal wavenumber-5 patterns often appear 15-20 days before heatwave events in the United States in 12,000 years of atmospheric general circulation model (GCM) simulations. Yuan et al. (2015) investigated the variability and trend of subtropical stationary waves during the NH summer. They found an increasing trend in wave amplitude over the 1979-2013 period, as well as changes in regional moisture fluxes accompanying stationary waves, which affected hydroclimate over several regions, including the central United States. In the last decades, an increasing number of studies investigated how quasi-stationary waves contribute to extreme events (Coumou et al., 2014; Hoskins and Woollings, 2015; Kornhuber et al., 2017; Wolf et al., 2018).

Due to the significance of stationary waves on regional climate, several recent studies have evaluated Rossby waves in GCM simulations and further found connections between the model's skills in simulating Rossby waves and in simulating the surface climate (e.g., Holman et al., 2014; Luo et al., 2022). For example, Simpson et al. (2020) used standard performance metrics, such as spatial correlation and root-mean-square errors of the time-mean eddy streamfunction, to evaluate stationary Rossby waves in two generations of model ensembles from the Coupled Model Intercomparison Project (CMIP) and a large ensemble of a single model. They found improved performance from the CMIP phase 5 (CMIP5) to CMIP6, and the model biases tend to be larger in JJA than in DJF. Other studies used metrics developed based on linear wave theory and vorticity budget to evaluate simulated Rossby waves. Nie et al. (2019) evaluated Rossby wave sources in the CMIP5 models, and Henderson et al. (2017) evaluated the teleconnection between North America and Madden-Julian Oscillation using the so-called stationary wavenumbers. Some studies have taken a step further to use more complex diagnostics of Rossby waves, such as the WA flux and Rossby wave ray tracing, to find close connections between near-surface climate and Rossby wave propagation biases in GCMs (Garfinkel et al., 2022; Choi and Stan, 2024). However, few studies have evaluated large-scale stationary Rossby waves in regional, dynamical downscaling simulations.

For limited-area models (LAMs), previous studies focused on atmospheric circulations with smaller spatiotemporal scales than stationary Rossby waves. Using the "Big-Brother Experiment" in which a smaller domain simulation is forced by the output from the larger-domain simulation using the same model, Denis et al. (2002b), Denis et al. (2003), and Dimitrijevic and Laprise (2005) evaluated the simulated atmospheric circulations on a monthly time scale. These studies found that lateral boundaries (LBs) do not significantly affect modeled sea-level pressure and relative vorticity; however, the vorticity fields exhibit some deviations from the driving model at higher atmospheric levels. Using a similar experimental design but with an idealized dry test case, Park et al. (2014) found unphysical inertia-gravity waves excited at the LBs. The artificial waves become stronger with longer LB update time periods, particularly when they are substantially longer than the LAM timestep, which is usually the case in climate-scale model integration. Miguez-Macho et al. (2004) documented how the interactions between the simulated flow and specified flows at LBs distort large-scale circulations in regional simulations over North America, and also demonstrated the usefulness of spectral nudging for the waves with synoptic and larger scales to remove the large-scale flow biases. Imberger et al. (2020) investigated the impact of the LB update frequency, size of the LB relaxation zone, and spectral nudging in the case study of a fast-propagating, strong mid-latitude storm. They found that the update frequency is most effective in mitigating reductions in storm intensity through LBs. Castro et al. (2007) and Chang et al. (2015) investigated how



110

125

130



the modes of large-scale climate variabilities via Rossby waves are simulated in regional downscaling by Empirical Orthogonal Functions, focusing on the teleconnections between tropical sea surface temperature (SST) and the North American Monsoon. They found that spectral nudging helps reproduce large-scale climate variabilities, but the dynamics and kinematics of Rossby waves were not their focus. Scarcity of Rossby wave evaluation in regional simulations may be related to an assumption that the large spatiotemporal scales of stationary Rossby waves are well resolved by the host GCM grid and sub-daily (e.g., six-hourly) frequency updates of LB conditions. However, this assumption is not necessarily valid.

A common numerical treatment of LB conditions is to blend the specified forcing with the state simulated by LAMs (e.g., Davies, 1976). Staniforth (1997) noted that such blending does not retain the balance within the flow, such as geostrophy. Deviation from the geostrophic balance excites inertia-gravity waves to restore the balance (Holton, 2004). The excitation of inertia-gravity waves would bring the state closer to geostrophic balance, but the LB treatment occurs at every time step; thus, the vicinity of the boundaries may always experience artificial imbalance. Such a disruption would distort the propagation of incoming Rossby waves, and the persistent divergence produced by the unphysical inertia-gravity waves (Park et al., 2014) may also contaminate the amplitude of the incoming Rossby waves.

Another modeling framework for dynamical downscaling is global variable-resolution (VR) models. One such model, the Model for Prediction Across Scales (MPAS, Skamarock et al. (2012)), is developed on an unstructured grid that can smoothly change grid spacing over a specified region. This model has been shown not to have the aforementioned issues associated with LBs (Park et al., 2014). However, the amplitude, pathways, and frequency of Rossby waves arriving in North America may be unrealistic. This is because for those waves originating from the tropics, the strength and spatial scales of the wave source are linked to the amplitude and profile of diabatic heating in the organized tropical convection, which is known to be difficult for GCMs to realistically simulate (Dai, 2006; Bacmeister et al., 2014; Bogenschutz et al., 2018; Park and Lee, 2021; Zhou et al., 2022; Chang et al., 2025). Furthermore, GCMs have long-standing biases in the location and strength of the jet (Harvey et al., 2020; Simpson et al., 2020). For dynamical downscaling using LAMs, one can choose host GCMs with small biases in those aspects. For dynamical downscaling with a global VR model, the model must exhibit good skills in both global-scale and regional-scale processes.

There is thus a clear need to evaluate stationary Rossby waves in dynamical downscaling simulations; however, a process-oriented evaluation has not been carried out to assess Rossby waves simulated by different modeling frameworks. To fill this gap, we evaluate three classes of dynamical downscaling approaches that have distinct representations of large-scale forcing. The first class is a standard regional climate simulation with a LAM, represented by the Regional Climate Model version 4 (RegCM4) simulation available from the North American branch of the Coordinated Regional Downscaling Experiment (Mearns et al., 2017) (NA-CORDEX). The second class is also a LAM simulation, but employing spectral nudging to constrain the large-scale atmospheric dynamics; the WRF simulation in NA-CORDEX is one such dataset. The third class is a global VR model that utilizes the MPAS dynamical core within the Community Atmosphere Model (CAM), referred to as CAM-MPAS. This model's regional refinement and simulation design follow the NA-CORDEX protocol (Sakaguchi et al., 2023). We will demonstrate that these three classes of models exhibit distinct biases in the upper-level circulations and Rossby wave



140

145

150

155

160

165



propagations. We also provide reviews and technical details of the diagnostics throughout the text and in the appendices for those interested in more background on Rossby wave theory.

2 Data and Methods

2.1 Downscaling and evaluation dataset

We use two simulations from the "Evaluation" experiment in NA-CORDEX (Diez-Sierra et al., 2022b), one using the RegCM4 model and the other using the WRF model. Both models are configured on 25-km grids following the NA-CORDEX protocol (Fig. 2b) (Diez-Sierra et al., 2022a). We also analyze another downscaling simulation conducted with the CAM-MPAS model on a global VR grid with a 100-km coarse domain refined smoothly to 25-km grid spacing over North America (Fig. 2a).

The RegCM model is a widely used regional climate model with a long history (Giorgi and Anyah, 2012). Downscaled data from the hydrostatic version of the fourth-generation RegCM4 are available from NA-CORDEX on both the 50 km and 25 km grids (Mearns et al., 2017; Bukovsky and Mearns, 2020; McGinnis and Mearns, 2021). Multiple options are available for the cumulus, boundary-layer, and land surface components (Giorgi et al., 2012), and each scheme is selected based on the performance of test simulations over the CONUS region, particularly in the warm-season precipitation (Arritt and Bukovsky, personal communication).

The WRF model is a regional model for weather and climate applications (Skamarock et al., 2008) and has been extensively used to study the present-day and future state of North American climate with a wide range of model resolutions and configurations (e.g., Chang et al., 2015; Liu et al., 2017; Chen et al., 2019; Srivastava et al., 2023). Version 3.5.1 was used for the NA-CORDEX experiment (50 km and 25 km). The model physics mostly follows those adopted by Castro et al. (2012), who focused on the warm-season climate of the western CONUS and the North American monsoon. Spectral nudging is applied to the temperature, winds, and geopotential height fields at the scales larger than approximately 1000 km to retain synoptic-scale variability in the driving GCM or reanalysis data (Castro et al., 2005, 2012; Hu et al., 2018).

CAM-MPAS is an experimental model in which the dynamical core is ported from the MPAS-Atmosphere version 4 to the CAM model within a beta version of the CESM2. The technical description of the model and downscaling experiments are provided in Sakaguchi et al. (2023). Briefly, MPAS is a global dynamical core that solves the fully compressible non-hydrostatic equations of motion on an unstructured grid (Skamarock et al., 2012). The unstructured grid can be configured as a global quasi-uniform resolution grid or a VR grid where one or more regions of interest have finer grid spacing than the rest of the globe. Advantages of the global VR model over LAMs include the absence of LBs and the consistent dynamical and physical schemes in the downscaling (high-resolution) domain and the coarse-resolution domain, which can avoid artificial shocks or gradients created by the LBs in LAMs.

All models use the ERA-Interim reanalysis product for initial and boundary conditions, including six-hourly updates to the LBs and daily updates to SST and sea ice fraction (SIC) at the bottom (surface) boundary. RegCM4 does not have a specific sea ice scheme, so SIC from ERA-Interim is not used. CAM-MPAS uses SST and SIC only since there are no lateral boundaries;





therefore, the large-scale circulations are not constrained. Table 1 lists the model characteristics and configurations. Table B1 compares the physics parameterizations used by the three models.

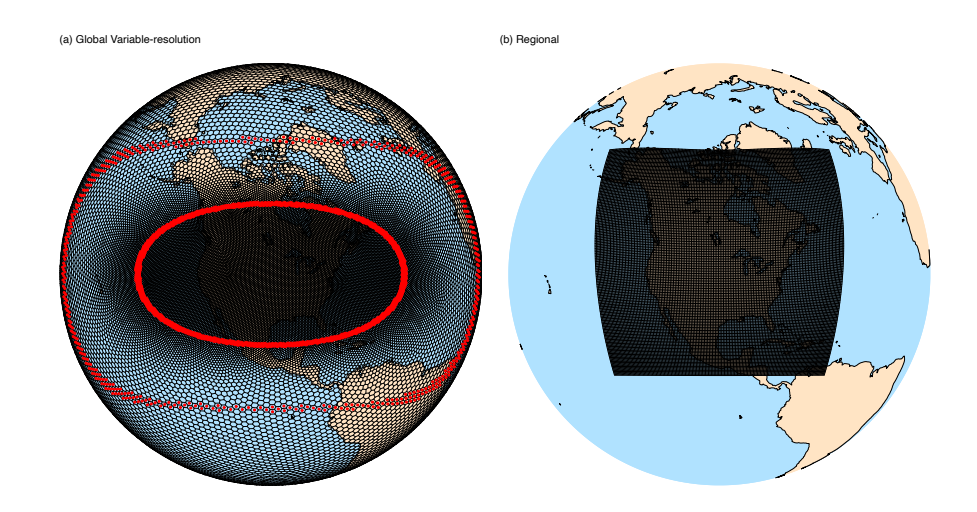


Figure 2. Model mesh examples: (a) global variable-resolution mesh for CAM-MPAS, (b) regional mesh for WRF. The mesh used by RegCM4 is visually similar to that of WRF (hence not shown), except it covers a slightly larger area.

The reference data we use is ERA-Interim, which drives the NA-CORDEX simulations for the "Evaluation" experiment. As discussed by Laprise et al. (2008), we expect that dynamical downscaling adds value primarily in the small-scale processes while maintaining the large-scale flow provided from the driving data. If this tenet is true, incoming Rossby wave signals are not affected by LBs or other model details; Rossby wave metrics calculated from the driving data (ERA-Interim) and from downscaling simulations within the LAM domain should be very close to each other. On the other hand, if numerical aspects of the downscaling model affect the circulations, such as artificial sources of divergence over the time scale of stationary Rossby waves, or the model exhibits mean biases in the general circulations (e.g., jet strength/width/positions), then we would see deviations in the Rossby waves between the driving data and the downscaling simulations. We are aware that this logic ignores a potential upscale effect from the downscaling simulation on the stationary Rossby waves. We will briefly discuss this assumption in Section 4; however, such upscaling signals cannot be easily quantified without a priori designed experiments (e.g., Denis et al., 2002b; Leung et al., 2013; Sakaguchi et al., 2016), and this is left for future work.

180 2.2 Data preparation

The NH summer season (JJA) in the 30-year period from 1980 to 2010 is analyzed, except for the CAM-MPAS simulation, which starts at 1990. Most analyses are performed using daily-mean variables at 200 hPa (zonal and meridional winds, geopotential height). This particular pressure level is chosen primarily because it is a standard pressure level available in the CORDEX archives (CORDEX, 2009). Note that grid boxes adjacent to the LBs, or "sponge/buffer/relaxation zone", where the



185

190

195

200



Table 1. Characteristics of the three downscaling models. The sponge zone width in CAM-MPAS refers to the transition zone. All models solve compressible mass and momentum equations. SST: sea surface temperature, SIC: sea ice fraction.

Configuration	RegCM4	WRF	CAM-MPAS
	25 km	25 km	25 km
Model domain	Regional	Regional	Global
Horizontal grid	Cartesian, B-grid	Cartesian, C-grid	Unstructured, C-grid
Number of grid columns	123,825	96,036	137,218
Vertical grid	Sigma	Terrain-following hydrostatic pressure	Terrain-following height
Vertical levels	18	28	32
Domain top (hPa)	50	50	2
W momentum eqn.	Hydrostatic	Non-hydrostatic	Non-hydrostatic
Time step (s)	50	150	600 (Physics)
			85 (dynamics)
Driving ocean BC variables	SST	SST,SIC	SST,SIC
Spectral nudging	No	Yes	No
Lateral boundary treatment	Nudging with exponential weights	Linear relaxation	Smoothly varying $\triangle x$
Horizontal sponge zone width	24 (grid points)	10 (grid points)	≈ 25 (degrees)

external forcing and model-predicted variables are blended (Appendix B1), have already been removed in the NA-CORDEX data (Table 1). This post-processing is designed for the usual use case of regional climate assessment within the model domain; for this study, it poses a challenge. This is because we *patch* the outside of the LAM domain with ERA-Interim data to produce spatially continuous fields, on which Rossby wave propagations are diagnosed. Without the relaxation zone that blends LAMs predictions and ERA-Interim data, our patched diagnostic approach exhibits stronger gradients between the model and ERA-Interim data than with the relaxation zone. We used a brief WRF simulation to evaluate the impact of removing the buffer zone, which was found not to significantly alter the analysis results within the model domain (Fig. B2). However, within the blending zone, the strength and spatial pattern of derived quantities (e.g., vorticity, divergence, and WA fluxes) change, and overall, they are notably noisier without the blending zone (Fig. B2a,b,d,e). The noise and spurious WA fluxes can be reduced to some extent by spatial smoothing applied over the relaxation zone (Fig. B2c, f). We tested several smoothing methods and present the figures that utilized a Gaussian filter within the buffer zone when the noise is significant. We do not attempt to evaluate Rossby wave sources/sinks along the LBs; those crucial aspects will be assessed in future work.

Prior to the patched analyses, all the data are regridded to a global 0.7° latitude-longitude grid using the *patch* method available from the Earth System Modeling Framework (ESMF) library (Balaji et al., 2018). The 0.7° grid is nearly identical to the original ERA-Interim grid and is coarser than the downscaling datasets. We still remap the ERA-Interim data to this grid to more fairly compare variability and extremes with the models, since remapping can smooth the fields and affect those



210

220

225

230



statistics (Sakaguchi et al., 2023). The patch method first estimates the grid corner values on the source grid using the secondorder polynomials, then weight-averages the corner values to obtain the final estimate on a target point value on the destination grid; therefore, the computation is more expensive than the commonly used bilinear method (Zienkiewicz and Zhu, 1995). The patch method estimates the values and their derivatives more accurately than the bilinear method (Balaji et al., 2018), which is desirable for calculating Rossby wave diagnostics that involve spatial derivatives.

It is critical to rotate the grid-relative u and v winds to the Earth-relative (eastward and northward) winds in the RegCM4 and WRF data before regridding. For the WRF model, the NCAR Command Language (NCL: NCAR (2017)) provides a function for wind rotation (wrf_uvmet). For RegCM4, we wrote an NCL function to rotate winds onto the Rotated Mercator projection, which is available in Sakaguchi (2025). It is often necessary to spatially smooth the variables, especially for winds at relatively high resolution. In most cases, we used a suite of spherical harmonic functions available in NCL: vhaeC, tri_trunC, and shaeC.

2.3 Diagnostic framework

2.3.1 Rossby wave ray theory

Wirth et al. (2018) reviewed diagnostics to study the dynamics of Rossby waves, particularly the frameworks to identify and track so-called Rossby wave packets. Wave energy, momentum, and other information propagate with the wave packets at the group velocity, not with individual wave crests/troughs (Vallis, 2017, Chapter 6). One of the commonly used diagnostics is the ray theory, which traces the trajectory of a wave packet from a specified source location. The potential or absolute vorticity equations are linearized by decomposing the variables into the base (or background or reference) state, which does not vary in time during the lifetime of the wave packet, and the perturbation from the base state (wave motions). Assuming a wave-like solution, we can obtain an algebraic relationship among the frequency, wavenumbers, and base states (the *wave dispersion relationship*), which leads to a set of ordinary differential equations for the time evolution of the wavenumbers and frequency. Knowing this kinematic information at t=0 and the base state, we can calculate the group velocity and predict where the wave packets will travel at t=1. At the new location, we solve for the wavenumbers again, yielding a new group velocity. Repeating the process gives us the evolution of wavenumbers and group velocities across space and time. Vallis (2017) provides a general introduction to ray theory for Rossby waves.

Hoskins and Karoly (1981) first applied the ray theory to stationary Rossby waves. Their ray theory assumes that the meridional wind in the base state (\overline{v}) is zero, and the zonal wind (\overline{u}) is a function of latitude only. Despite these strong assumptions, their result reproduced many aspects of the Rossby wave propagations inferred from statistical analyses and numerical model results. However, this assumption is hard to justify given our focus on regional climate over North America, as seen in the 2009 heatwave example in the Introduction section. Therefore, we adapt the ray theory developed by Li et al. (2015) and Zhao et al. (2015) (hereafter LZ2015). Unlike earlier Rossby wave ray-tracing methods, LZ2015 allows a base state that varies in both the zonal and meridional directions, with non-zero \overline{u} and \overline{v} . The input for the LZ2015 ray theory consists of the background winds $\overline{u}(x,y)$ and $\overline{v}(x,y)$, the wave source location, and the initial zonal wavenumber k_0 . Given those inputs, LZ2015 solves the following equations:





$$\frac{d_g k}{dT} = -k \frac{\partial \overline{u}}{\partial X} - l \frac{\partial \overline{v}}{\partial X} - \frac{1}{K^2} \left(l \frac{\partial \overline{\eta}_x}{\partial X} - k \frac{\partial \overline{\eta}_y}{\partial X} \right) \tag{1}$$

235

240

245

250

255

260

$$\frac{d_g l}{dT} = -k \frac{\partial \overline{u}}{\partial Y} - l \frac{\partial \overline{v}}{\partial Y} - \frac{1}{K^2} \left(l \frac{\partial \overline{\eta}_x}{\partial Y} - k \frac{\partial \overline{\eta}_y}{\partial Y} \right) \tag{2}$$

where l is the meridional wavenumber (m^{-1}) , $K = \sqrt{k^2 + l^2}$ is the total wavenumber, $\overline{\eta}$ denotes the background absolute vorticity (s^{-1}) $\overline{\eta} = \overline{\zeta} + f$, f is the Coriolis parameter, and $\overline{\zeta}$ is the vertical component of the background relative vorticity. The operators $d_g/dT = \partial/\partial T + u_g\partial/\partial X + v_g\partial/\partial Y$ represent the total derivative describing the rate of change following the wave packet moving at the group velocity. Expressions for the group velocity are given in the Appendix C. The coordinate variables T, X, and Y are the zonal, meridional, and time coordinates for a local, wave-scale motion that has substantially smaller scales than those for the mean state (t,x,y); this scale separation allows us to treat wavenumbers as constant within the local coordinate (making eqns. 1 and 2 linear). To maintain consistency with the assumed scale separation, climatological mean fields are smoothed by truncating wavenumbers larger than 10 after spectral decomposition using spherical harmonics, before being passed to the ray tracing algorithm as the background state. The frequency must be specified in the ray tracing code, and is set to zero for our analysis, so that the ray theory solves the trajectories of stationary Rossby waves.

After running the ray tracing algorithm, we can visually compare wave ray trajectories in the background state from ERA-Interim and those from the model simulations. To make model evaluation more quantitative than visual inspection of rays, we compare probabilities of Rossby wave propagation over each grid point, obtained by tracing a large number of rays. For example, if 5,000 Rossby wave rays are initiated in a source region with slightly different input parameters, and 50 of them pass a grid box, then the probability of 0.01 is assigned to the grid box. To create an ensemble ray tracing, we start rays every two grid boxes within a source region (≈ 20 to 40 degrees wide in x and y directions), which results in ≈ 150 to 300 source points per region. For each source point, we initiate Rossby waves with 12 different k_0 (1 – 12). We also consider three background states: the climatological winds for June, July, and August. Permuting the source points, 12 initial zonal wavenumbers, and three base states yields 5,000 to 10,000 ray trajectories from each source region.

We note that this is a rather arbitrary approach to creating an ensemble of Rossby rays, since our base state and choice of k_0 may ignore important characteristics of Rossby waves in a particular region or time period. For instance, the preferred wavelengths of stationary waves excited over the Indian Monsoon region and the Tibetan Plateau appear to differ [wavenumbers 6-7 for the former and 4-5 for the latter (Joseph and Srinivasan, 1999; Park et al., 2013)]. To more accurately quantify the probabilities of ray trajectories beyond model evaluations, one may consider a broader range of parameter space (Li et al., 2019) and/or specify the parameter ranges based on a priori knowledge of the wave sources and time period of interest (Garfinkel et al., 2022; Chang et al., 2023a). Here, our tenet is that, given the same set of parameters and specifications for the base state, dynamical downscaling models can reproduce the probability distributions of stationary Rossby waves in the original forcing data if the relevant large-scale dynamics are faithfully retained.



265

270

275

280

285

290



2.3.2 Wave activity flux

In the introduction, we used the diagnostic derived by Takaya and Nakamura (1997, 2001) to visualize the flux of WA, which is a linear combination of kinetic energy and enstrophy, and is also related to the momentum exchange between the mean circulation and perturbations. Similar to LZ15, TN01 used a horizontally non-uniform background with non-zero meridional winds to derive their WA budget equation, making it an appealing tool for regional climate studies (Schneidereit et al., 2012; Sakaguchi et al., 2016; Chen et al., 2023; Zhang et al., 2024). TN01 obtained the following conservation equation for WA from the quasi-geostrophic (QG) potential vorticity equation:

$$\frac{\partial \mathbf{M}}{\partial t} + \nabla \cdot \mathbf{W} = D_T$$

$$\mathbf{M} = \frac{1}{2}(A + E)$$
(3)

where \mathbf{M} ($m \, s^{-1}$) is the wave activity density, \mathbf{W} is WA flux ($m^2 \, s^{-2}$), A and E are the quantities proportional to perturbation vorticity and kinetic energy, and D_T represents non-conservative diabatic and friction terms ($m \, s^{-2}$). Since WA flux is denoted by \mathbf{W} in TN01, we refer to their WA flux as the W-vector as well. All quantities are derived from the base-state and perturbation geopotential height. The actual expression for the W-vector is provided in the Appendix C2. The vertical components of the W-vector and kinetic energy (hence \mathbf{M}) involve vertical derivatives; thus, data at multiple pressure levels with sufficient resolution are required. Such high vertical-resolution data at a daily frequency are not always available from model archives such as NA-CORDEX and are therefore not included in the analysis. As a result, we infer the source/sink of WA by the convergence/divergence of the horizontal components of the W-vector.

We noted that the W-vector is not sensitive to different levels of spatial smoothing to the background state (not shown), presumably because of the underlying QG framework. Insensitivity to the background smoothness is an advantage for a diagnostic metric. On the other hand, the QG assumption appears to limit the validity of the W-vector in low-latitude regions, where we often observe unphysical variability in the W-vector. Also, unless the model simulation is an idealized one with a specified wave source, the W-vector at a given time and location includes contributions from all waves from different sources (at the specified phase velocity), which may complicate interpretation. On the other hand, the ray theory by LZ15 is applicable over the tropics and deals with a single wave packet from a specified location, making the dynamical interpretation more straightforward. However, the barotropic, non-divergent vorticity equation underlying the LZ2015 does not consider the influence of divergence on Rossby wave propagation (Li, 2020), which is included in the W-vector diagnosis. The ray theory is more computationally involved than the W-vector due to time integration and does not diagnose the wave amplitude and momentum forcing. Therefore, the W-vector and wave-ray diagnostics complement each other, enabling a better understanding of Rossby wave dynamics.





3 Results

3.1 Evaluation of surface air temperature

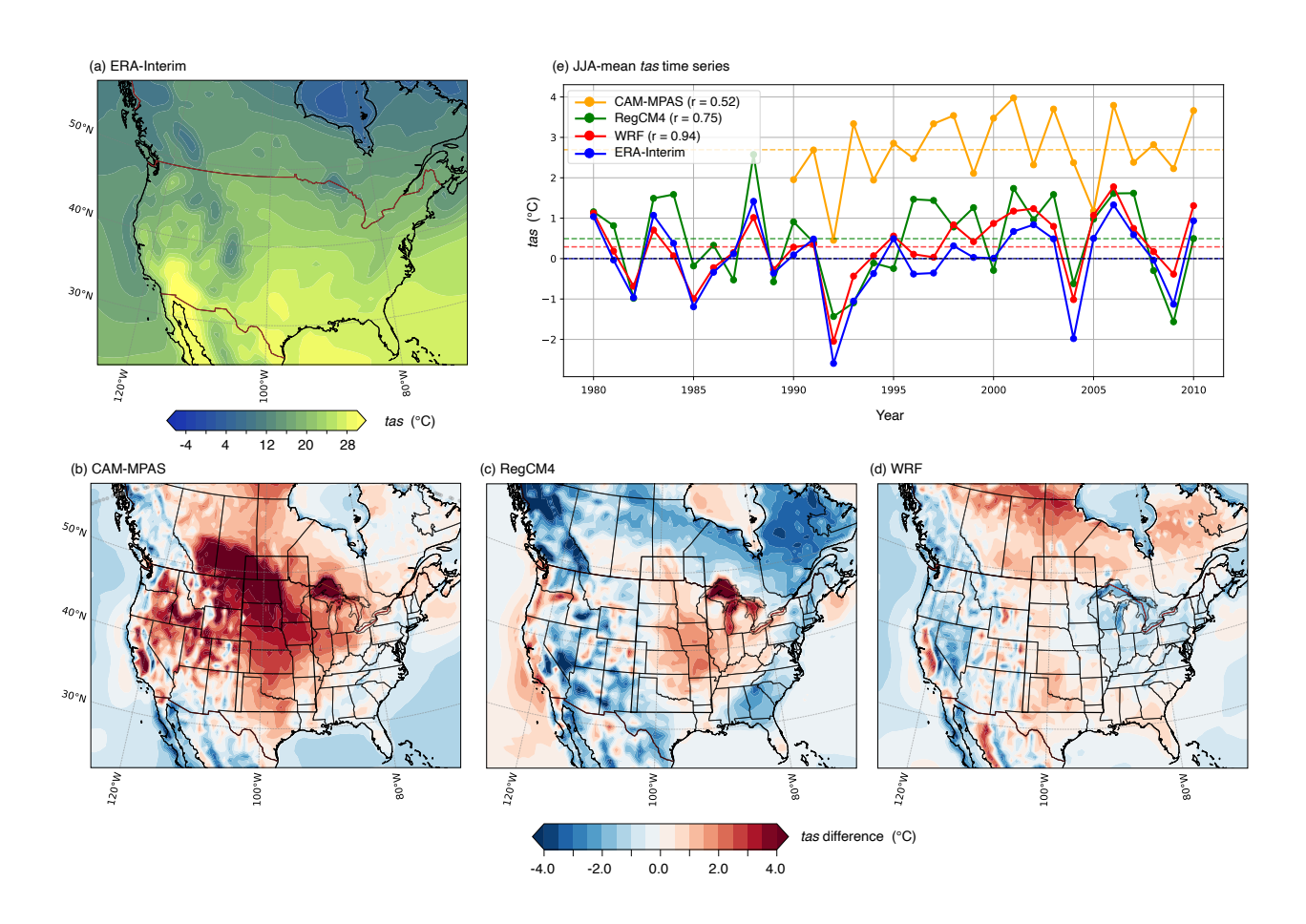


Figure 3. JJA-mean *tas* over North America in ERA-Interim (a) and *tas* difference between ERA-Interim and (b) CAM-MPAS, (c) RegCM4, and (d) WRF. The panel (e) shows the time series of JJA-mean *tas* anomaly in each year, averaged over the central North America (the black box in (b)-(d)). The mean bias against ERA-Interim is added to the anomaly time series and shown by the colored dashed lines. The legend text includes the linear correlation (r) between the model and the ERA-Interim time series.

We begin with the evaluation of *tas* in the dynamical downscaling simulations. Figure 3b-d shows the JJA-mean *tas* biases of the three models against ERA-Interim, showing rather distinct spatial patterns across the models. CAM-MPAS and WRF exhibit a warm bias over Canada, whereas RegCM4 tends to have a cold bias there. Over the western CONUS, CAM-MPAS tends to simulate higher *tas* while RegCM4 and WRF tend to simulate lower *tas* than ERA-Interim. An exception is central North America, where all three models exhibit warm biases to varying degrees, consistent with previous studies (Morcrette et al., 2018; Sy et al., 2024). CAM-MPAS has by far the worst bias centered around the U.S.-Canada border. The notably higher



305

310

315

330



bias of CAM-MPAS implies the importance of LB constraint for simulating *tas*, assuming that physics parameterizations in each model perform equally well. In the RegCM4 simulation, the highest bias over land occurs in the South Central region. The highest bias of WRF is over Canada and further south in SGP.

To assess the timing and magnitude of seasonal anomalies, we also plot the time series of JJA-mean *tas* anomalies relative to the all-year JJA climatology in each dataset (Fig. 3e), averaged over the central North America region (black box in Fig. 3b-d). The model mean bias against ERA-Interim is added to the anomaly time series (also indicated by the horizontal dashed lines). Without the LB constraint, the time evolution of *tas* anomaly in CAM-MPAS is not expected to precisely follow that of ERA-Interim, except for the years with substantially strong external forcing such as the cold anomaly in 1992 after the Pinatubo eruption in the previous year (Robock and Mao, 1995); the impact is felt by CAM-MPAS through the anomalously cold SST, but not through the aerosols since the CAM-MPAS model used prescribed aerosol forcing based on the year 2000 condition (the RegCM4 and WRF simulations do not consider aerosol effects either). RegCM4, with the LB constraint, produces a reasonable correlation with ERA-Interim (0.75). In some years, however, *tas* anomaly in RegCM4 deviates significantly from that in ERA-Interim (e.g., 1995-1999). WRF with spectral nudging achieves the highest correlation of 0.94 with ERA-Interim, and also with the smallest mean bias over the central North America region (2.7, 0.5, and 0.3 °C for CAM-MPAS, RegCM4, and WRF, respectively).

Figure 4 compares simulated standard deviations (σ_{model}) of monthly mean tas of each grid box to those in ERA-Interim (σ_{ERAI}) as the ratio ($R_{\sigma} = \sigma_{model}/\sigma_{ERAI}$). ERA-Interim shows the strongest variability in the PNW region in the United States (Fig. 4a). CAM-MPAS is able to capture this variability center as indicated by R_{σ} being close to one over the region (Fig. 4b). However, it overestimates the tas variability in western Canada and the central U.S. RegCM4 overestimates the variability over most of North America, particularly over western Canada, and northern and southern central U.S, and the east coast (Fig. 4c). The contrast in the RegCM4 skills between the mean and variability indicates that the LB forcing can constrain the time-mean but not necessarily the temporal variability of tas. The WRF simulation again shows very good agreement with ERA-Interim (Fig. 4d).

3.2 JJA climatology of large-scale circulations

Acknowledging that not only the upper-level dynamics but also the local land-atmosphere interactions (Bukovsky et al., 2017; Ma et al., 2018) and the upscale growth of convective systems (Qin et al., 2023) play crucial roles in *tas* bias, we focus on the role of the seasonal to sub-seasonal scale upper-level circulations through the lens of Rossby wave dynamics. This section reviews some key aspects of the JJA climatology of the upper-level circulations relevant to stationary Rossby waves. The evaluation of the model-simulated upper-level circulations over North America follows it.

As in other seasons, the JJA-mean zonal winds are characterized by the extratropical and subtropical jets but with lower wind speeds and less zonally uniform structure (Fig. 5a). The extratropical jet is nearly circum-global except for the discontinuities over the eastern Pacific and Atlantic oceans, where the subtropical jet extends from ≈ 20 °N latitude to merge with the midlatitude jet. Since jet streams serve as wave guides (Manola et al., 2013; Branstator and Teng, 2017; Wirth, 2020), we expect that Rossby waves propagate from the Pacific Ocean to North America along the mid-latitude as well as the subtropical jets.





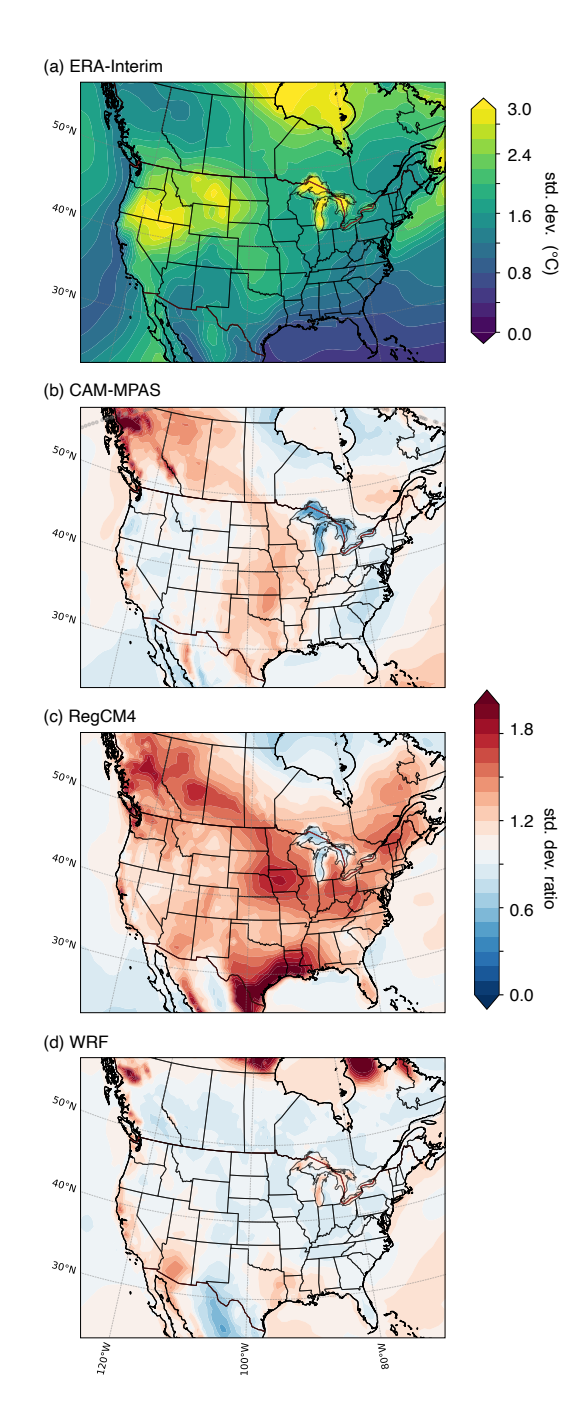


Figure 4. JJA monthly standard deviations of *tas* in ERA-Interim (a) and the ratio of the standard deviations ($\sigma_{model}/\sigma_{ERAI}$) in (b) CAM-MPAS, (c) RegCM4, and (d) WRF.



340

345

350



When Rossby waves enter the East Pacific and the West Coast of North America, they encounter complex mean wind patterns, where the traditional assumptions for the base state in Rossby wave dynamics — namely, zonally uniform flow with zero meridional winds — are not valid. Indeed, over the Western U.S., the mean zonal and meridional wind speeds are comparable; the former range from 12 to $20 \ ms^{-1}$, while the latter can be as high as $8 \ ms^{-1}$ (Fig. 5b). Therefore, the meridional wind's role in Rossby wave dynamics should not be ignored in this region.

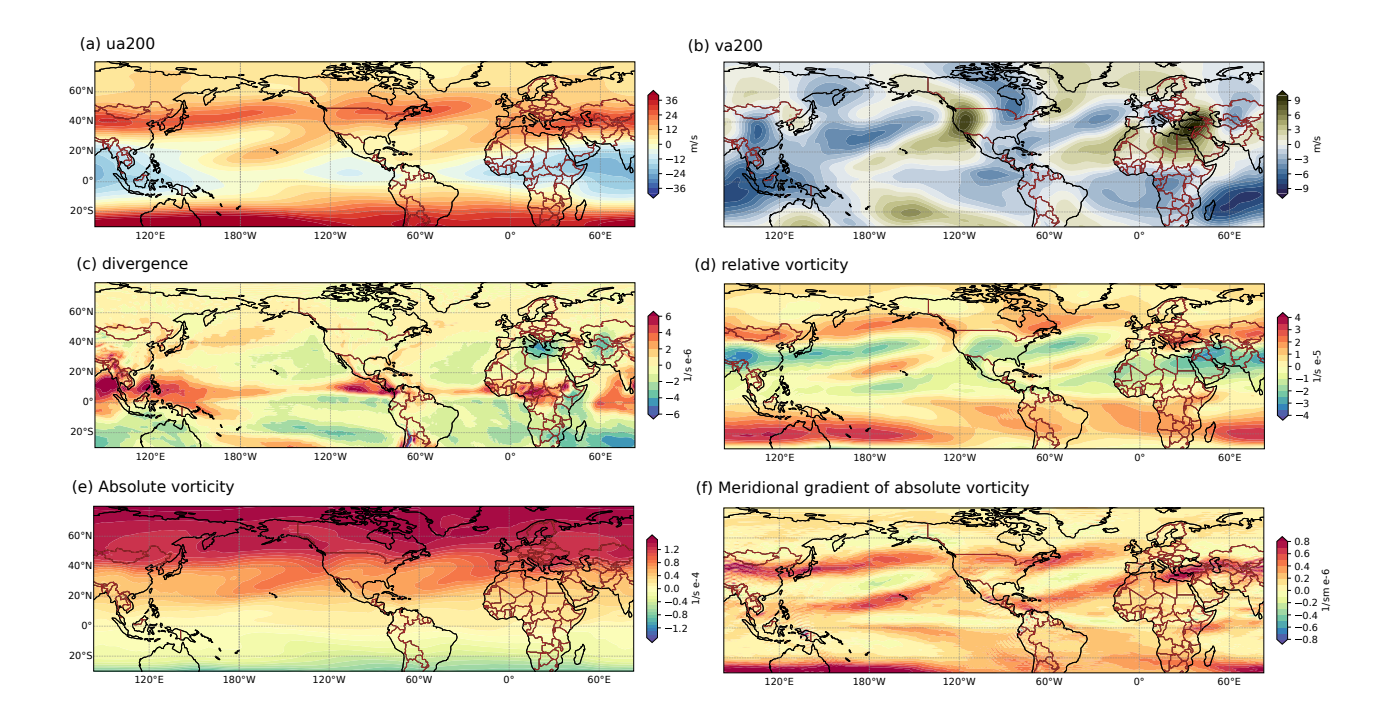


Figure 5. The 30-year JJA-mean winds at the 200 hPa level in the ERA-Interim data: (a) zonal wind, (b) meridional wind, (c) divergence, (d) relative vorticity, (e) absolute vorticity, and (f) meridional gradient of absolute vorticity.

Vorticity and divergence are essential for Rossby wave dynamics and are also shown in the figure (Fig. 5c,d). One aspect of the jet being a waveguide stems from the strong horizontal shear at its edges, which creates relative vorticity and its gradient. Also, the interaction between vorticity and divergence creates vorticity ($\eta(\nabla \cdot \mathbf{v})$), often called Rossby Wave Sources (RWS) (Sardeshmukh and Hoskins, 1988). In JJA, local maxima and minima of the mean relative vorticity near the jet create the meridionally banded structure over the Pacific and Atlantic oceans. The relative vorticity maxima near the subtropical jets are also strong enough to produce zonal anomalies of the *absolute* vorticity (Fig. 5e). As a result, two sharp meridional gradients of absolute vorticity, or the regions of strong restoring force for Rossby waves, exist upstream of North America from the northern and tropical Pacific (Fig. 5f). A notable divergence anomaly is found in the southern flank of the jet over the North Pacific, associated with the storm track. In the tropics, strong divergence is co-located with intense precipitation. Upper-level convergence exists over the Mediterranean and Middle East regions in association with the Asian Monsoon (Rodwell and Hoskins, 1996). Those are potential source regions for Rossby waves propagating to North America.





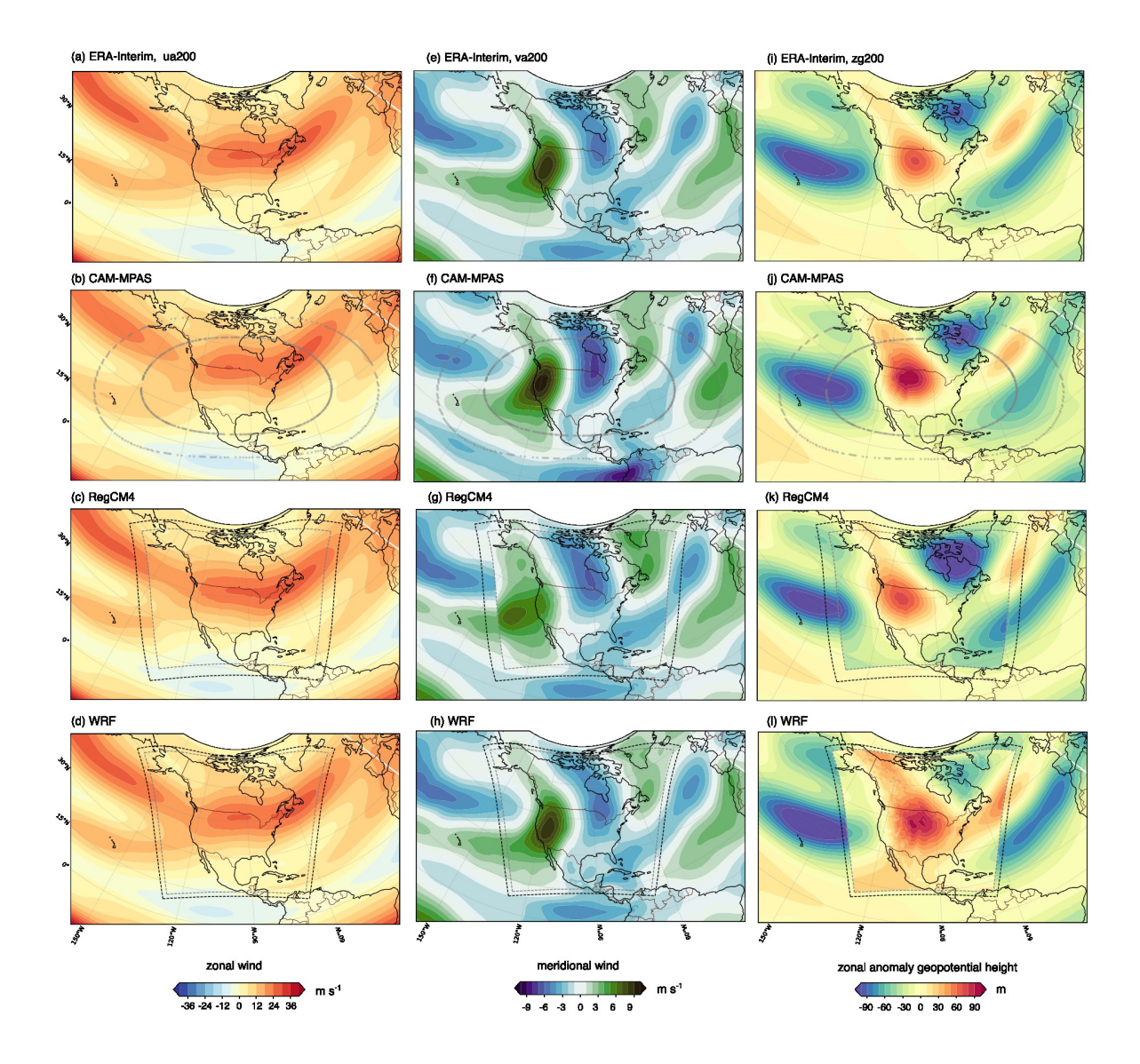


Figure 6. The JJA-mean zonal winds (left column), meridional winds (middle column), and zonal anomaly geopotential height (right column) at the 200 hPa level over the NA-CORDEX domain, in ERA-Interim (a,e, i), CAM-MPAS (b,f,j), RegCM4 (c,g,k), and WRF (d,h,l). In the second row for CAM-MPAS, the gray markers denote the approximate boundaries between the high-resolution domain, transition zone, and low-resolution domain of the variable-resolution grid. In the bottom two rows for RegCM4 and WRF, the black dashed lines denote the original model domain boundary, and the gray dashed lines denote the boundaries of the post-processed NA-CORDEX data, which excludes the blending zone near the lateral boundaries (24 and 10 grid points for RegCM4 and WRF, respectively; see also Table 1 and Appendix B1). For RegCM4 and WRF, the regional model data are shown within the NA-CORDEX data domain, and ERA-Interim data are used outside the domain, including the blending zone.



355

360

365

375

380



For evaluating the upper-level circulations in the downscaling simulations, we focus on three variables: the mean 200-hPa zonal winds (*ua200*), meridional winds (*va200*), and zonal anomalies of geopotential heights (*zg200*)(Fig. 6). As explained in Section 2.2, the modeled fields from the two LAMs are patched with the same fields of ERA-Interim outside the model domain, a visualization also used by Denis et al. (2002b). We use the full fields here instead of the differences between the simulations and ERA-Interim to emphasize the overall spatial patterns and unphysical discontinuities (difference plots are provided in Fig. B1). Ideally, for LAMs, the mean circulation across the LBs appears seamless. This is the case with the WRF simulation (Fig. 6d,h,l), where its spatial patterns are identical to those from the ERA-Interim even inside the model domain; the contour plot for the difference from ERA-Interim confirms negligible bias (Fig. B1). The geopotential height is slightly and uniformly higher within the WRF domain than ERA-Interim, but identifying the sources of *zg200* bias in WRF is left for future work.

The overall patterns simulated by RegCM4 look reasonable, but discontinuities are apparent along the boundaries (Fig. 6c, g, k). Inside the model domain, the subtropical jet entering California is weaker than ERA-Interim, and the *va200* and *zg200* patterns are shifted to the west. These patterns are time-invariant stationary waves that exist in the *mean* circulation, which we distinguish from quasi-stationary waves defined as the perturbation on the mean. CAM-MPAS captures the general structure of the upper-level circulations without artificial boundary effects (Fig. 6b, f, j); however, the jet core is weaker and located more northwestward than ERA-Interim, while the meridional wind speeds are overestimated (also see Figure B1a,d). Consistent with the overestimated *va200* speeds, the *zg200* zonal anomaly over North America is too high compared to ERA-Interim (Fig. 6i,j). In other words, the amplitude of the time-mean stationary waves is too strong. The position of the positive maxima of *zg200* anomaly coincides with the spatial structure of the mean warm bias in *tas* (Fig. 3b), indicating the contribution of the upper-level mean wind bias to the *tas* mean bias. On the other hand, in the case of RegCM4, the mean bias in the upper-level winds and warm bias in *tas* do not spatially overlap.

3.3 Model biases in Rossby wave propagations

The mean wind biases shown above imply that the waveguide structure for Rossby waves is also biased in the model simulations. To verify, we use the ray theory by LZ2015. To trace Rossby wave rays, we need to specify the locations of the wave sources. Previous studies suggest several remote sources of Rossby waves reaching North America during the summer, including the East Asian and Indian Monsoon regions, the western Pacific, the Tibetan Plateau, and the Mediterranean. (e.g., Ting, 1994; Ambrizzi et al., 1995; Trenberth et al., 1998; Wang et al., 2001; Lau and Weng, 2002; Ding and Wang, 2005; Wang et al., 2007; Lin, 2009; Li et al., 2015, 2019). Most of them found Rossby waves propagating along the mid-latitude jet, but Rossby waves can travel along the subtropical jet from wave sources in the central and eastern tropical/subtropical Pacific to North America (Li et al., 2019). Some of those waves are initiated during the Madden–Julian Oscillation phases 5 and 6, travel across North America, and break over the Atlantic Ocean, which are shown to suppress tropical cyclone activities (Chang et al., 2023a). A closely related subseasonal variability, the boreal summer intraseasonal oscillation (BSISO), is also found to enhance convective heating during particular phases, which triggers Rossby wave trains that tend to place a high-pressure ridge over the Pacific Northwest region (Lubis et al., 2024). Chen et al. (2023) found that the CMIP6 models project wave sources



385

390

395

400

405

410

415



in the tropical/subtropical eastern Pacific to intensify under the greenhouse gas forcing, exerting a more substantial influence on the surface temperature anomalies over western North America.

Ensemble ray tracing is performed as described in Section 2.3.1 for the source locations suggested by previous studies and by our preparatory analyses (Appendix C3). Results from five source locations are shown in Fig. 7 using the ERA-Interim climatological winds as the base state. Stationary Rossby waves excited in the northern North Pacific (NP) (Fig. 7a) and eastern tropical/subtropical Pacific (EP) (Fig. 7b) have significantly higher probabilities of propagating over North America than those originating from other areas. Waveguides extending from the eastern subtropical Pacific (20°-30°N) to North America are evident for the waves originating from these two regions.

Most waves excited in the West Pacific region travel southeast across the equator owing to the tropical easterly zonal wind and the monsoonal southerly meridional winds (Li et al., 2019). Rays from the Indian Monsoon region travel west as equatorial Rossby waves; some rays travel further west across the Atlantic Ocean, as seen in Lin (2009). The Tibetan Plateau generates Rossby waves that travel west; some of these waves arrive in North America from the east, while others turn east over North Africa and propagate along the jet stream. Some of those results may appear inconsistent with previous studies, and it is possible that wave activities originated from the other locations to reach North America, particularly in other seasons (Wang et al., 2020; Zhang et al., 2024), through non-linear processes such as Rossby wave breaking and associated wave reflection (Abatzoglou and Magnusdottir, 2006), or by the interactions of propagating Rossby waves and the background divergent circulation (Sardeshmukh and Hoskins, 1988; Li, 2020), which are not included in the linear ray theory. Nonetheless, one-point correlation maps for meridional winds are consistent with the ray tracing result, such that statistically significant lead/lag correlations with the grid points over North America are found only when the base points are specified in the NP and EP regions (and Caspian Sea but with negative lags, thus winds over North America leads the winds over Caspian Sea; see Appendix C3). With those results, we consider it reasonable to focus on the upwind source regions of NP and EP for evaluating regional downscaling simulations.

Sub-samples of individual ray trajectories from these two regions are shown in Fig. 8 to illustrate actual wave rays and their relationship to the initial zonal wavenumber (k_i) and background circulations. The figure uses climatological July winds as the base state, but the result is qualitatively similar to those obtained with June or August climatological flows (not shown). Rossby waves excited over the NP region with smaller k_i (i.e., longer wavelengths) tend to travel south/southeast toward the subtropical eastern Pacific, then turn east/northeast to reach North America. The climatological flow patterns immediately south of the NP source region have the northerly meridional winds of $\approx -5 \, ms^{-1}$ with comparable or even weaker zonal winds (Fig. 5a,b). Also, the meridional group velocity is inversely proportional to the second power of the wavenumber; thus, smaller wavenumbers favor larger group velocity (eqn. C11). Those two aspects likely facilitate southward propagation from NP. On the other hand, those initiated with larger k_i tend to propagate along the mid-latitude jet and travel across North America near the U.S.-Canada border (Fig. 8c).

Located more southeastward, the EP region is situated within the northward meridional background winds (Fig. 5b). Consistently, the waves excited here with smaller k_i first propagate north, and turn around at the northern edge of the mid-latitude jet (Fig. 8e,f). Similar to the waves from the NP region, waves initiated with larger k_i tend to be trapped within the mid-latitude





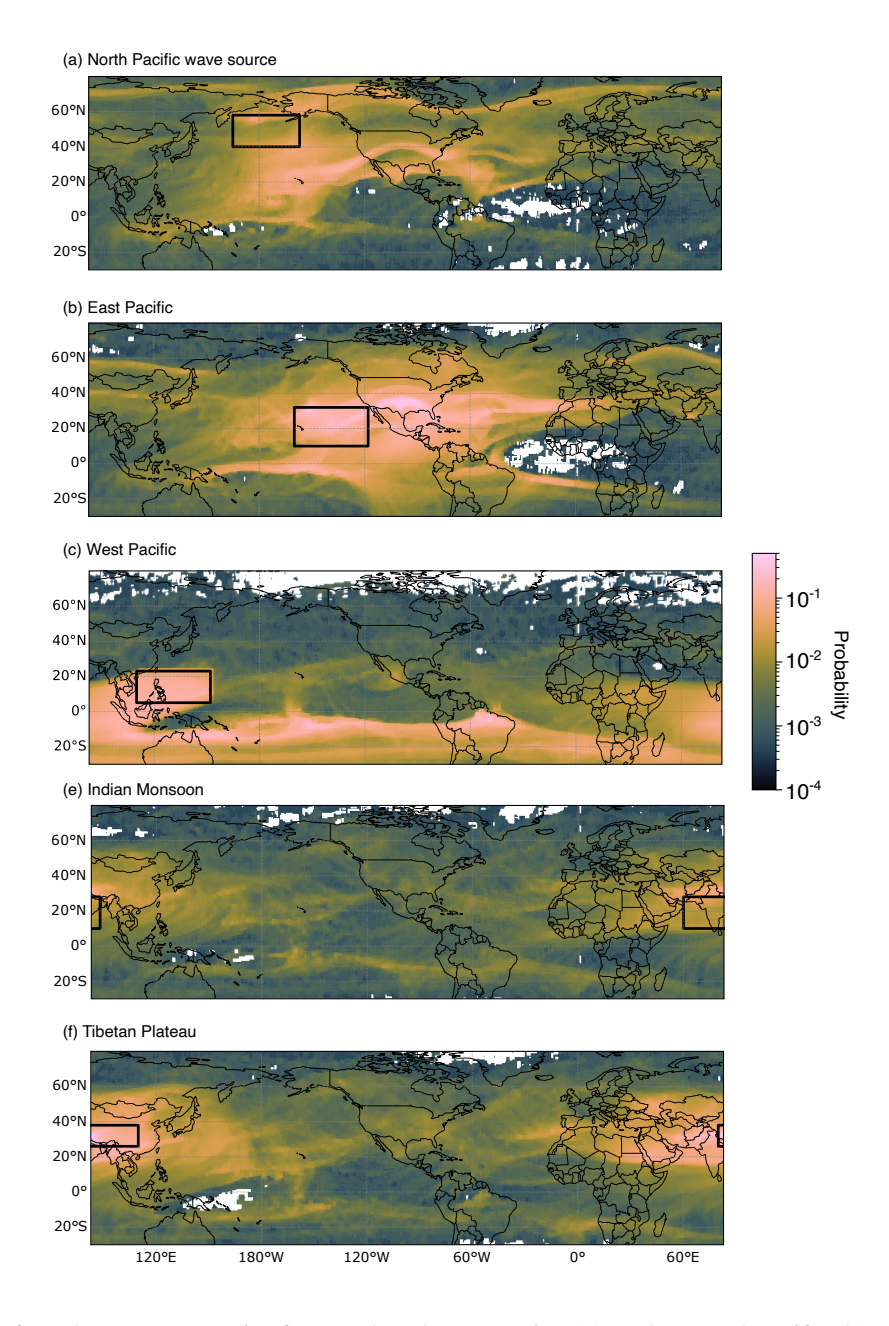


Figure 7. Probability of Rossby wave propagation from a selected source region: (a) northern North Pacific, (b) eastern subtropical Pacific, (c) western tropical Pacific, (d) East Asian Monsoon, (e) Indian Monsoon, and (f) Tibetan Plateau. Probability is calculated for each grid box as the fraction of rays reaching the grid box over the total number of rays traced from a source region. The base-state wind fields are the 1980-2010 monthly climatologies for June, July, and August from ERA-Interim.





jet and propagate more zonally. For both source regions, waves with even larger k_i are not able to propagate across North America (Fig. 8c,d, g,h) (Li et al., 2019)). The result illustrates the sensitivity of Rossby ray propagation to the base state, thereby highlighting the profound impact of mean circulation bias on modeled Rossby wave propagation.

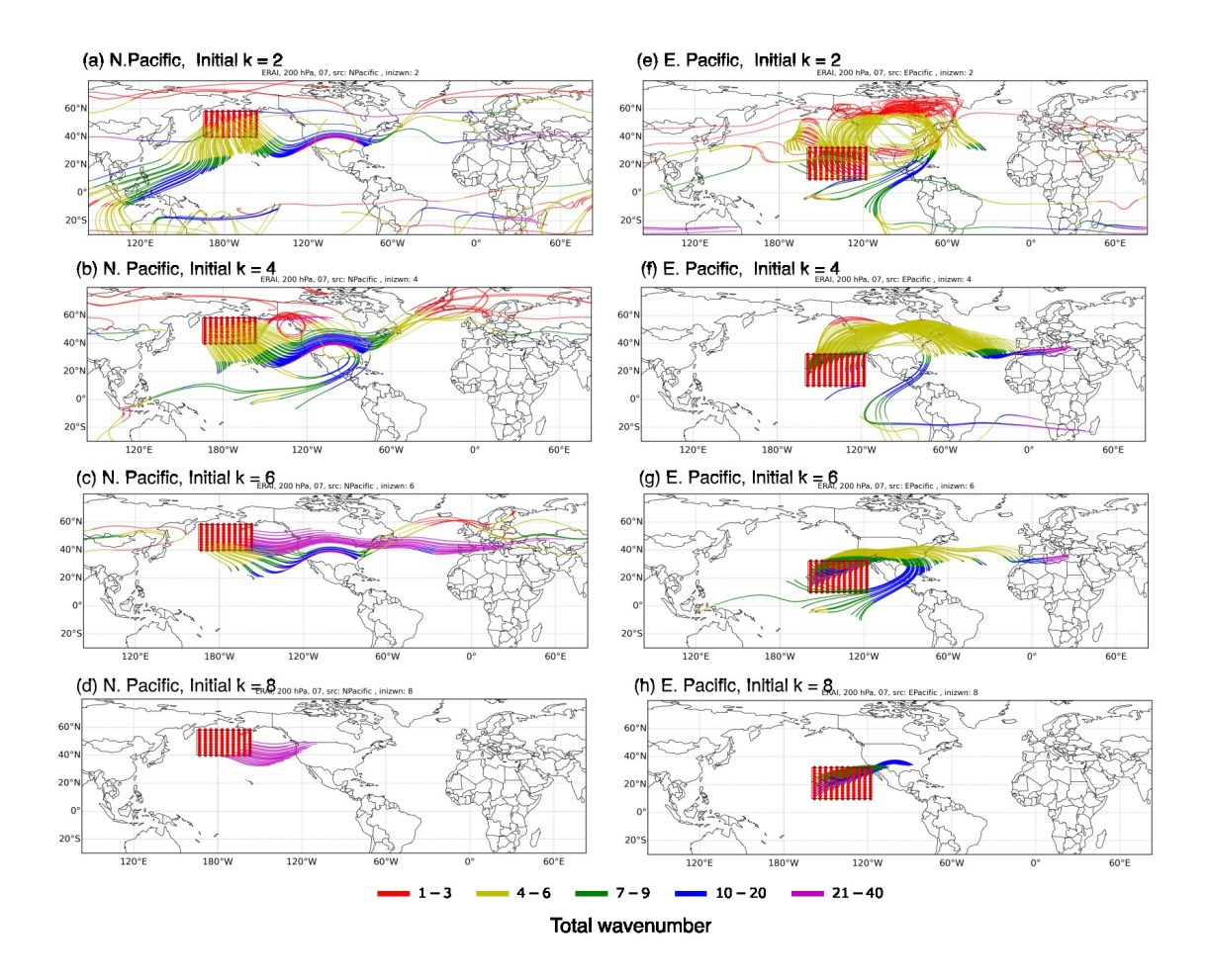


Figure 8. Samples of Rossby wave rays using the climatological July circulation from ERA-Interim as the base state. Each panel shows rays initiated from different source regions and with a specific initial zonal wavenumber (k): (a) the North Pacific source region with initial k=3, (b) also from the North Pacific source region but with initial k=8, (c) the East Pacific source region with initial k=2, (d) also from the East Pacific source region but with initial k=6, (e) the Tibet source region with initial k=1, (b) also from the Tibet source region but with initial k=9. Line colors represent time-dependent total wavenumber K (equation C10), and red dots show the source point location. Rays are terminated when the total wavenumber reaches 40 (wavelength of $\approx 1,000$ km, assuming that they are not small-amplitude perturbations at the geostrophic scale anymore (wave-breaking).

We evaluate the downscaling models by the ratios of the ray propagation probabilities $(R_p = p_{model}/p_{ERAI})$ (Fig. 9). The ray probabilities in the WRF simulation are almost identical to those in the ERA-Interim $(R_p \approx 1 \text{ in Fig. 9 g,h})$, as expected from the small bias in the upper-level circulations. For the other two models, biases in jet and meridional wind speeds lead to



440

445

450

455



significantly different wave-propagation patterns compared with ERA-Interim. For the waves initiated in the NP region, CAM-MPAS overestimates the probabilities over Canada and northern CONUS, and underestimates them over the southern part of CONUS (Fig. 9c). This is likely the result of the northward-shifted mid-latitude jet and overestimated southerly winds over the West Coast (Fig. B1a,d), which promote more zonal propagations at higher latitudes instead of traveling to the south. Such propagations are seen for the waves initiated with relatively small zonal wavenumbers (Fig. 10a for $k_i = 4$). For those waves, the mean circulation patterns in CAM-MPAS support longer-lived, circumglobal propagation that passes over North America twice, contributing to higher propagation probabilities. Such long-lived waves are rare for the same initial zonal wavenumbers with the ERA-Interim base state. For the waves from the EP region, stronger southerly winds over the West Coast region likely allow more waves travel north, but the slightly weaker and wider jet in CAM-MPAS appears to be a less effective waveguide, spreading the rays more widely over North America, particularly to the south of the jet where CAM-MPAS simulates higher propagation probabilities (Fig. 9d).

The Rossby wave probabilities in RegCM4 show some similarity with those in CAM-MPAS (Fig. 9e,f), likely due to the two models sharing the mean circulation biases over the western part of the NA-CORDEX domain (Fig. B1b,g). We can see more dense lines of wave rays emanating north from the EP source region (west of 120 °W) in the RegCM4 simulation than in ERA-Interim (Fig. 10b v.s. Fig. 8e), where stronger southerly winds are noted in the RegCM4 simulation (Fig. B1g). At the same time, the overestimated southerly winds appear to limit the southward wave propagation from the NP region, thus shifting the probabilities northward over North America (Fig. 9e). The mean wind patterns over North America in RegCM4 allow waves from the EP region with larger k_i to travel farther than in the ERA-Interim base state, for example, for the initial zonal wavenumber of eight (Fig. 10c v.s. Fig. 8h). Those waves also contribute to the higher probabilities from the EP region. LB effects are not apparent in the RegCM4 ray-tracing results. This is due to the smoothing of the base state *after* the RegCM4 and ERA-Interim data are patched onto the global grid, thereby effectively weakening discontinuities at the lateral boundaries.

Overall, biases in the large-scale circulations in CAM-MPAS and RegCM4 tend to increase wave-propagation probabilities in the northern part of North America, particularly in the RegCM4 base state. Additionally, the probabilities for Rossby waves around 40°N over CONUS from the NP region are underestimated, whereas both models overestimate those from the EP region. Those two biases would not simply cancel each other out, because Rossby waves propagating from the NP region tend to have higher wavenumbers (shorter wavelengths) over North America than those from the EP region (Fig. 9c, g). The smaller waves from the NP region may be more susceptible to breaking. In contrast, those from the EP region in wavenumbers four to six may have higher probabilities of resonating with Rossby waves of similar wavelengths but different frequencies (Petoukhov et al., 2013; Coumou et al., 2014). Those non-linear processes are not part of our diagnostics, though.

The shifted Rossby wave propagations in CAM-MPAS and RegCM4 may disrupt the spatiotemporal correlations between Rossby waves and surface climate, as seen in the 2009 heatwave example in the Introduction. In the two model simulations, the biases in Rossby wave probabilities and *tas* variabilities both exhibit large magnitudes over the Pacific Northwest, suggesting a connection between the two biases. We explore the connection in the following sections.





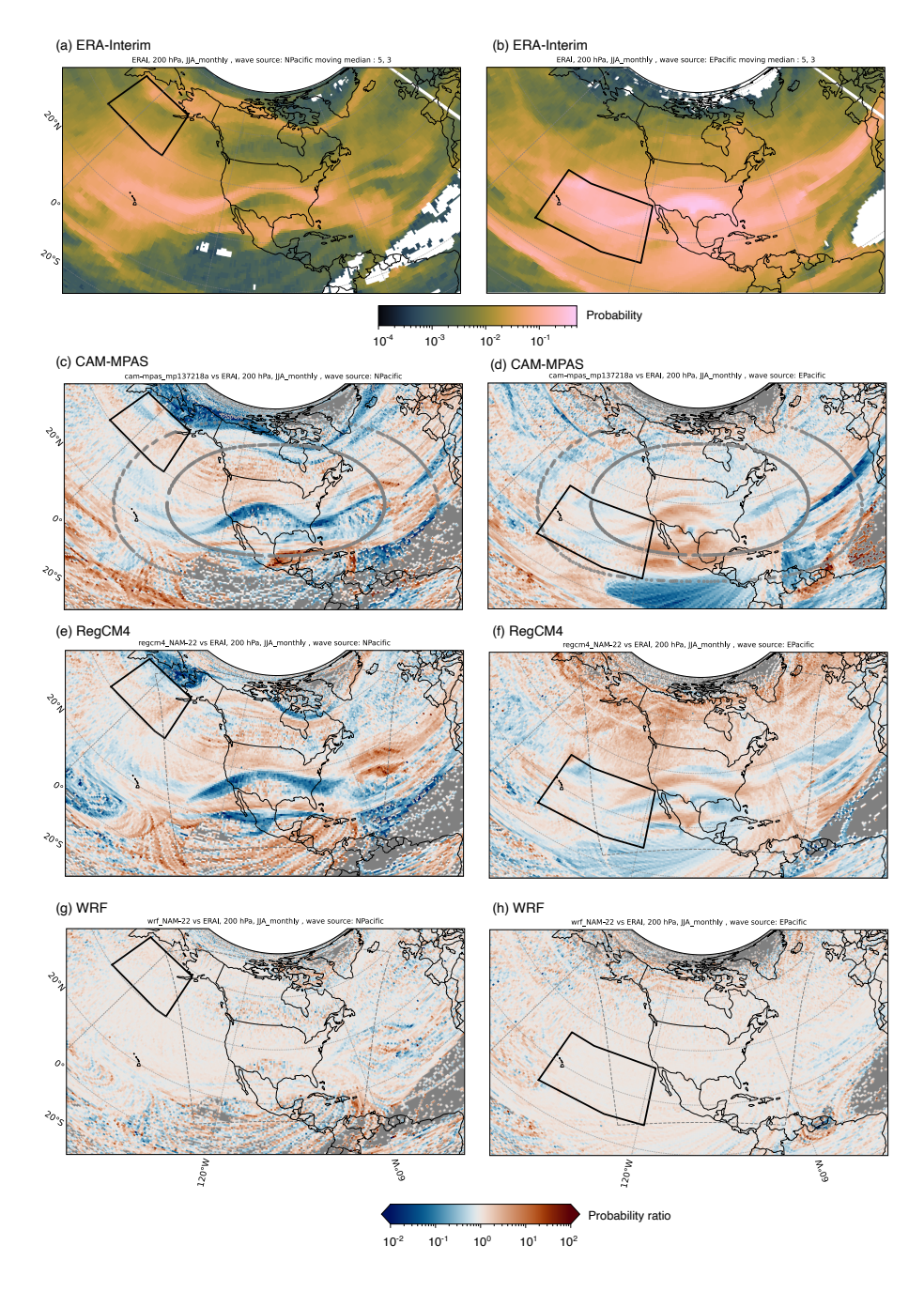


Figure 9. Probability of Rossby wave propagation from the North Pacific and East Pacific source regions obtained from ERA-Interim (a, b), and the ratio of the probabilities as $R = P_{model}/P_{ERAI}$ for CAM-MPAS (c, d), RegCM4 (e, f) and WRF (g, h). $R = 1 = 10^0$ means the equal probabilities of ray propagation in the model and ERA-Interim. A five-point running average is applied before plotting to reduce noise, primarily over the regions of low probabilities.





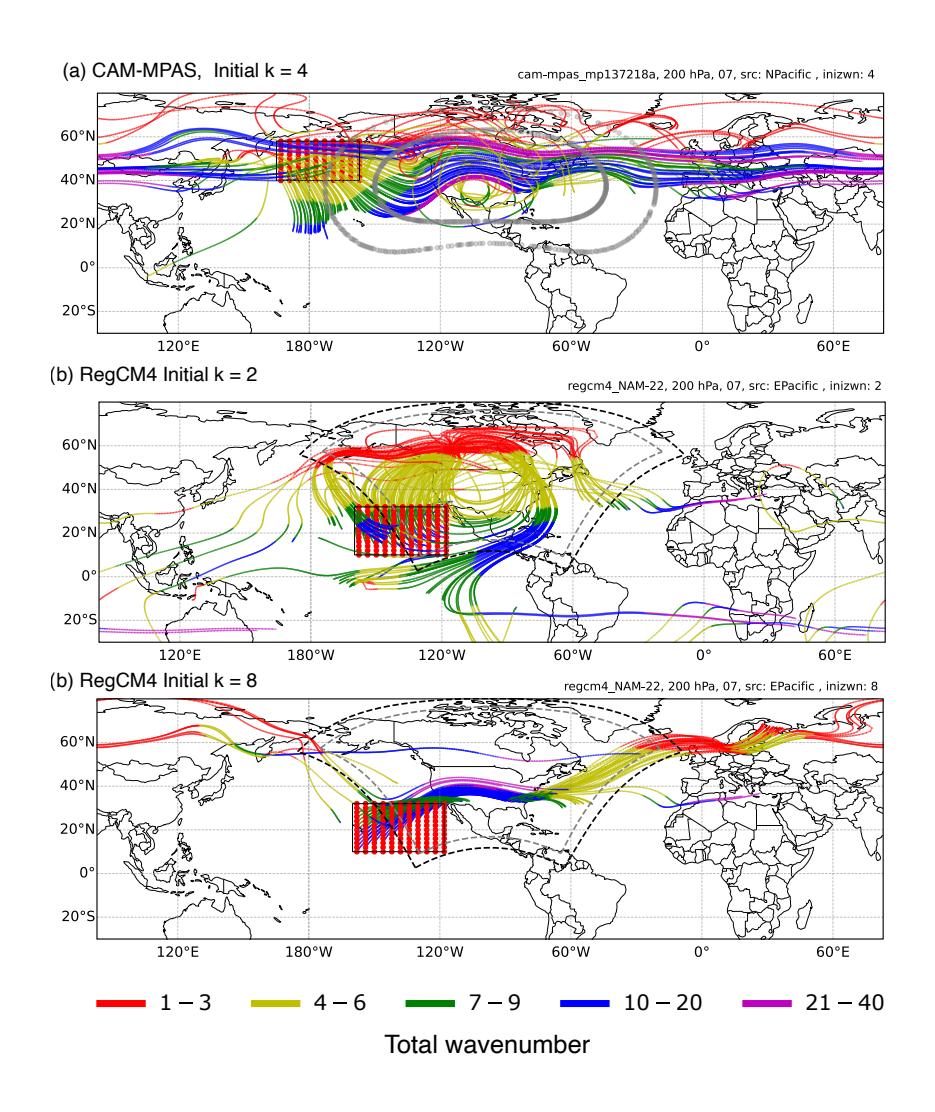


Figure 10. Samples of Rossby wave rays using the climatological July circulation from the downscaling models as the base states. (a) CAM-MPAS for waves initiated in the North Pacific source region with initial k=4, (b) RegCM4 for waves from the East Pacific source region but with initial k=2, and (c) RegCM4 with initial k=8. Line colors represent time-dependent total wavenumber K (equation C10), and red dots show the source point location. Rays are terminated when the total wavenumber reaches 40 (wavelength of $\approx 1,000$ km, assuming that they are not small-amplitude perturbations at the geostrophic scale anymore (wave-breaking).



460

465

470

480

490



3.4 Wave activity flux and surface air temperature

Calculation of the WA flux by TN01, or W-vector, requires the base and perturbation (wave) geopotential fields. We define stationary Rossby waves as the time-filtered daily-mean perturbation from the 30-year (20-year for CAM-MPAS) daily climatology (base state). A band-pass time filter is used to extract the variations within the 25–90-day frequency range. Also, the phase velocity is set to zero in the W-vector terms. The W-vector is calculated for each day and then averaged to produce the 30-year JJA climatology for visualization purposes.

From a global point of view, the area with the most vigorous stationary Rossby wave activity in the JJA season is the Pacific Ocean, followed by the Atlantic Ocean, both characterized by large flux and strong divergence of the W-vector (Fig. 11a). We interpret the areas of divergence as indicating WA sources. Vigorous WA fluxes from the NP and EP wave sources converge on the West Coast of North America, then propagate across the continent to diverge out from the East Coast, in general agreement with the 2010 heatwave case (Introduction). The pathways from the two source regions agree with the ray theory result, including the initial southward propagation from the NP region.

Figure 11 compares the W-vector patterns over North America in the downscaling models and ERA-Interim. The most notable feature is the bands of strong divergence/convergence pairs along the LBs in the RegCM4 simulation (Fig. 11c), which strongly suggests inconsistency between ERA-Interim and RegCM4 circulations, even considering the removed relaxation zone (Section 2.2). Although some spuriously large W-vectors emanating from LBs should be ignored, those downwind over the Pacific coastal area and the Pacific Northwest region are calculated fully from the model data, thus reliable. There, the W-vector in RegCM4 is oriented more zonally than in ERA-Interim, and some of the WA flux appear to originate at the LB rather than from the NP and EP regions. Not only the coastal region, but also the WA fluxes over the central U.S. differ between RegCM4 and ERAI; RegCM4 simulates a more northerly W-vector, while ERA-Interim suggests a more zonally propagating flux. The W-vectors in the WRF simulation are almost identical to those from ERA-Interim (Fig. 11d); subtle linear structures in the divergence pattern parallel to the lateral boundaries may be due to the removal of the relaxation zone in the W-vector calculation. The global VR simulation of the CAM-MPAS model does not suffer from such artifacts (Fig. 11b). However, the zonal propagation of the W-vector is shifted northward from the U.S. to Canada, creating an anticyclonic rotation over the central U.S., possibly due to the overly strong positive geopotential anomaly (Fig. 6j). With this northward shift, the Wvector divergence over the East Coast of the U.S., as seen in ERA-Interim, is replaced with weak convergence in CAM-MPAS. In addition, the W-vector divergence in CAM-MPAS is overly strong near the coastlines and mountain ranges on the West Coast compared to other models and ERA-Interim. We have examined the variance spectra of surface topography, vertical velocity, and horizontal winds, but there is no indication that the topography and wind kinetic energy in CAM-MPAS differ significantly from those in other models (Fig. B3). Topography-related processes in the CAM-MPAS downscaling simulations will be investigated in future work, which may help explain the strong WA flux divergence over the mountainous region.

How are the differences in the WA flux patterns reflected in the regional climate? We first look at the lead/lag correlations between the five-day running mean zg200 anomalies across North America and the divergence of the W-vector averaged over the West Coast region, where we see strong convergence in the climatology of ERA-Interim (Fig. 11a). Since the W-vector





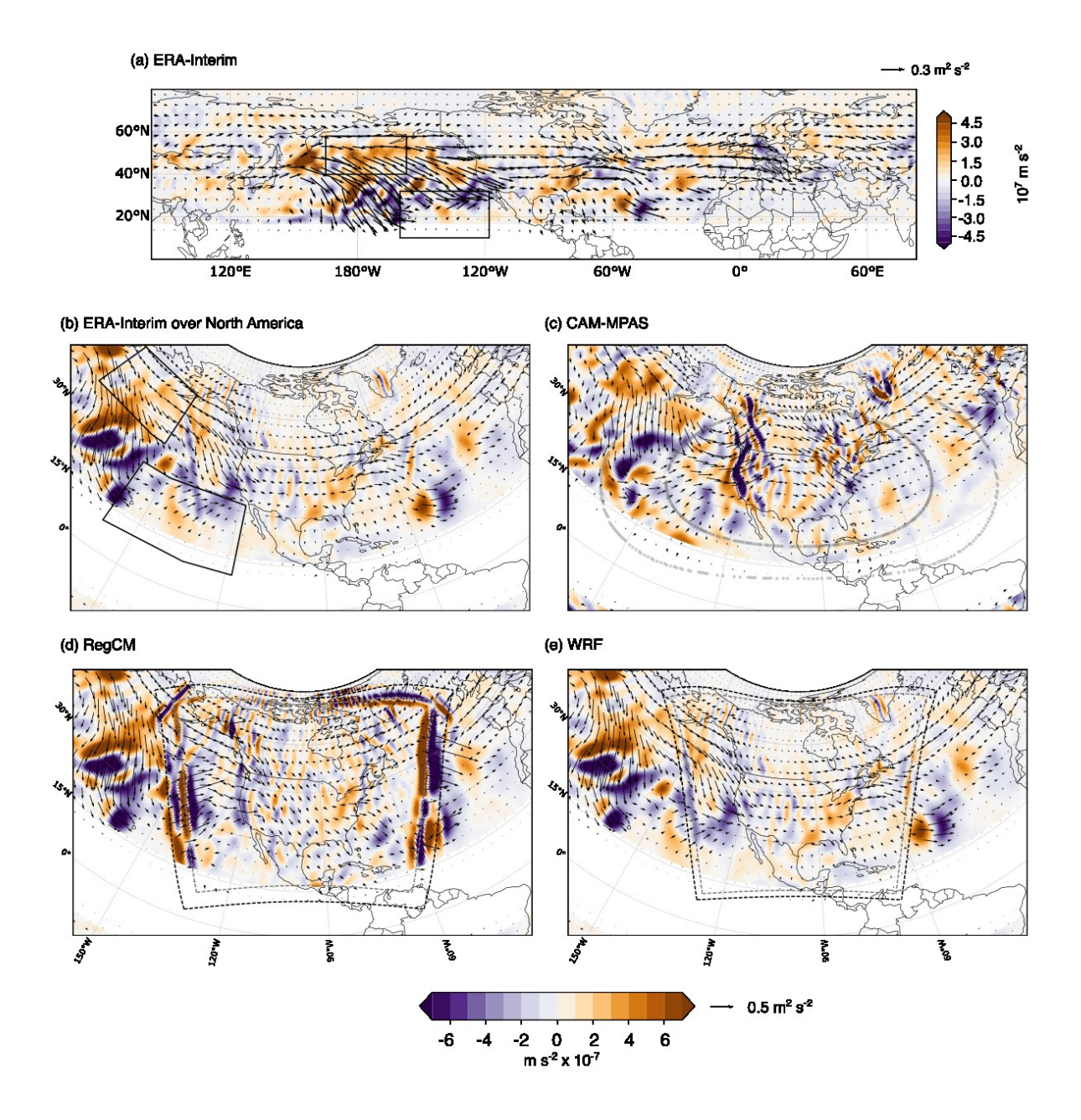


Figure 11. JJA climatology of horizontal components of the W-vector (arrows) and its divergence (color) at the 200 hPa level in (a, b) ERA-Interim, (c) CAM-MPAS, (d) RegCM4, and (e) WRF. The regions between 10°S and 10°N are masked because the Quasi-geostrophic assumption for the W-vector is not generally valid. The black boxes represent the source locations used for the ray tracing in Section 3.3. Note that the vector scale and color limits are different between (a) and the other panels. In the RegCM4 result, a Gaussian filter is applied to the relaxation zone.



495

500

505

515

520

525



is calculated from the geopotential anomalies band-passed for 25-90 day variabilities, this assessment essentially examines correlations across time scales (5 days vs. 25-90 days) and across space between the West Coast and the rest of North America. Each time series consists of daily data spanning 30 years (20 years for CAM-MPAS) of JJA seasons. The statistical significance is determined following Li et al. (2019) using the two-tailed Student's t-test against the null hypothesis of zero correlation, taking into consideration the autocorrelation of each time series in determining the degrees of freedom (eqn. 1 in Pyper and Peterman (1998)).

In ERA-Interim, statistically significant negative correlations appear upstream over the Gulf of Alaska and positive correlation just off the U.S. West Coast around lag -2 (Fig. 12a), that is, zg200 anomalies off the U.S. West Coast for a given day is positively correlated with W-vector divergence over the West Coast happening two days later (or the higher zg200 anomalies off the U.S. West Coast are, the stronger WA flux divergence will be in two days later over the West Coast). CAM-MPAS can reproduce the correlation pattern, albeit weaker than ERA-Interim (Fig. 12b). RegCM4 misses the negative correlation over the Gulf of Alaska, extending the area with a positive correlation northwest toward the Gulf of Alaska (Fig. 12c). WRF with the spectral nudging can capture this lag-2 correlation pattern (Fig. 12d). At lag+4, statistically significant negative correlation appears over the SGP in ERA-Interim, creating a clear wave pattern (Fig. 12e). This negative correlation means that W-vector convergence (negative values) over the West Coast leads to a positive zg200 anomaly over SGP four days later. WRF generally captures this lag+4 correlation pattern, but without statistical significance over SGP (Fig. 12f). The other two models struggle to reproduce the lag+4 correlation (Fig. 12f,g)

The *tas* response to the W-vector divergence closely follows the *zg200* response. Again, we calculate lead/lag correlations between five-day running mean *tas* anomalies at each grid point and the daily W-vector divergence averaged over the West Coast region (Fig. 13). In ERA-Interim, areas of statistically significant negative correlations appear over SGP around a lag of -2, with the maximum extent occurring when the *tas* anomaly is lagged by four days (lag+4). It suggests that the *tas* over the SGP tends to be higher than normal when the WA flux converges over the West Coast, particularly 4–8 days earlier. Focusing on the lag+4 result, WRF is the only model to simulate the significant negative correlation over SGP and the overall structure of the lead-lag correlation (Fig. 13b,f). CAM-MPAS simulates a weak negative correlation over SGP but misses the statistical significance (Fig. 13d). Also, the correlation patterns over the Pacific Northwest, western Canada, and Alaska do not agree with those in ERA-Interim. Similarly, RegCM4 misses the negative correlation center over SGP, and also simulates unrealistic negative correlation over the eastern Pacific (Fig. 13e). The inability to reproduce the W-vector – *tas* correlation in these two models is likely one reason for the biases of the mean and/or variability of *tas* over SGP (Figs. 3 and 4).

It is also possible to correlate the W-vector divergence and the *errors* in the simulated *tas*. Figure 14a presents the lead-/lag correlations between the W-vector divergence averaged over the West Coast region in the RegCM4 simulation and the difference in the daily mean *tas* between RegCM4 and ERA-Interim at each grid point. In this case, we observe statistically significant correlations over SGP at lag +4. This correlation and the lack of correlation between *tas* anomaly and the W-vector divergence (Fig. 13c) together suggest that accurately receiving Rossby wave signals through LBs and maintaining the large-scale forcing patterns are essential for LAMs to reproduce the cross-scale forcing from Rossby waves to *tas* in the driving reanalysis or GCM data. Another example is based on the observation that the W-vector convergence is significantly overesti-





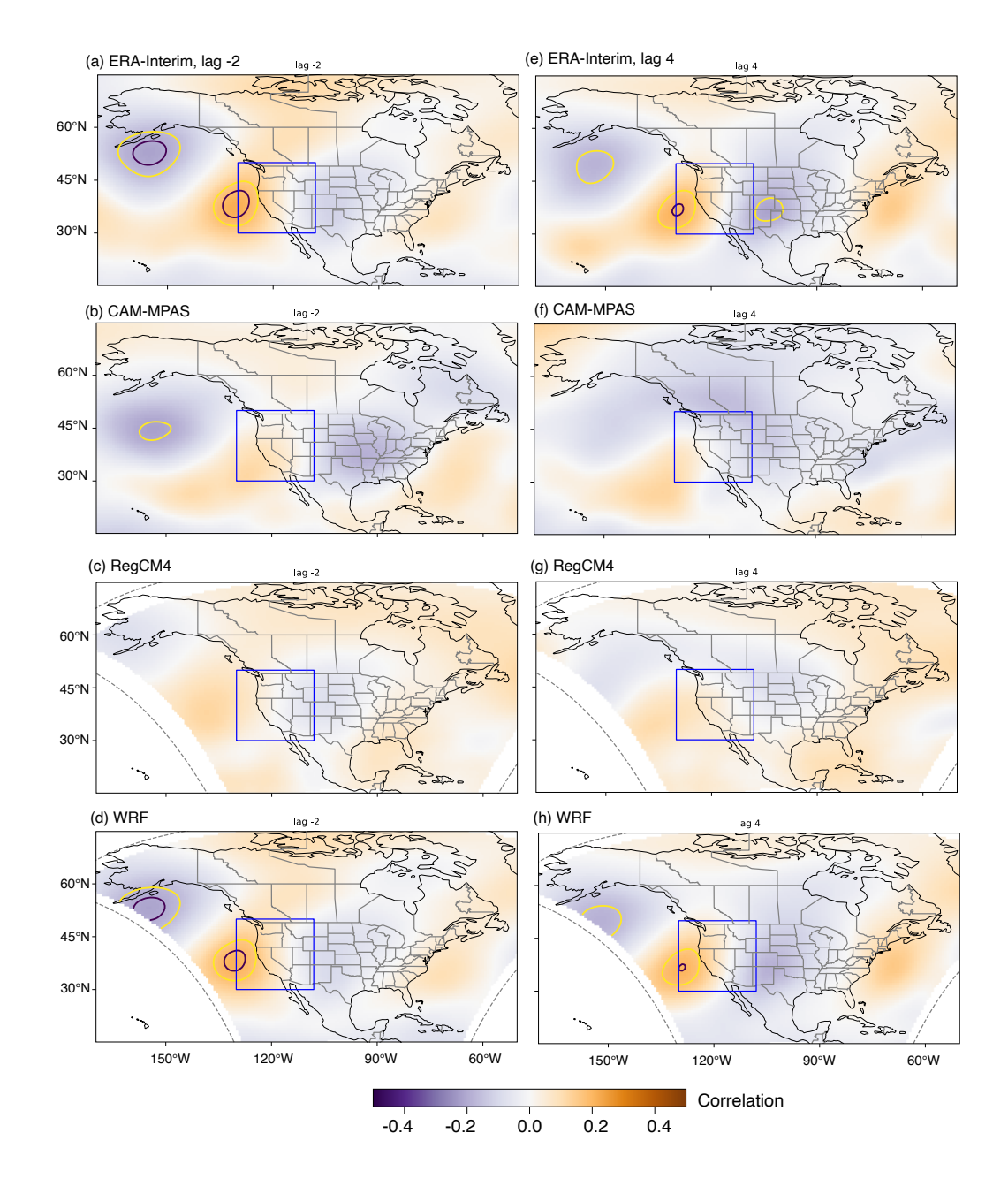


Figure 12. The lead-lag correlation between W-vector divergence averaged over the West Coast (blue box) and the five-day running mean zg200 at each grid box. Negative lags mean that the zg200 time series leads and is shifted earlier by that amount —e.g., by 2 days in panel (a)— before the correlation is calculated against the time series of W-vector divergence. With positive lags, zg200 lags the W-vector divergence, i.e., the zg200 time series is shifted later by that amount. Yellow and black contours indicate areas with statistically significant correlations at $\alpha = 0.10$ and $\alpha = 0.05$ levels, respectively.





530

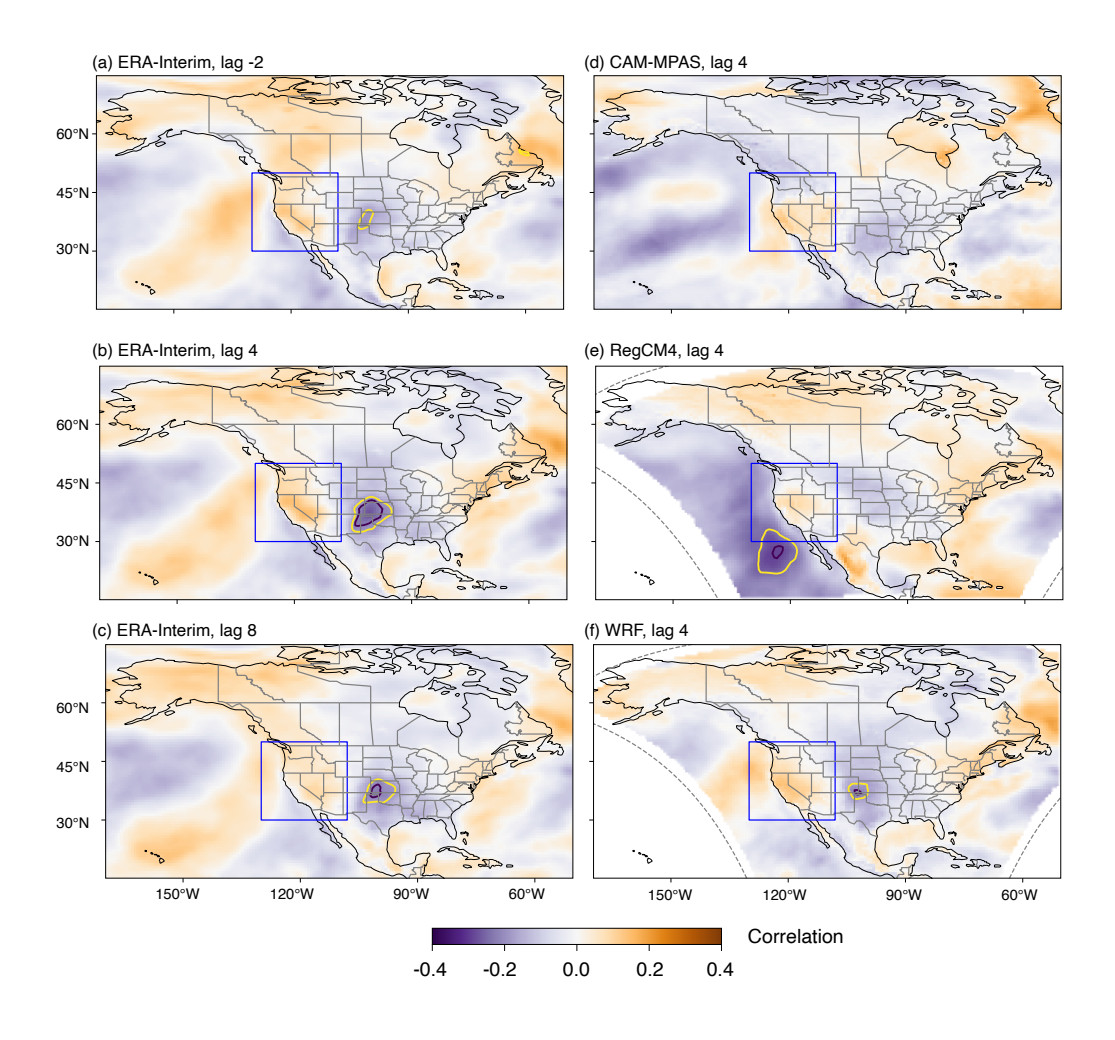


Figure 13. Same as Fig. 12, but for the lead-lag correlations between the W-vector divergence averaged over the West Coast (blue box) and the five-day running mean (*tas*) anomaly at each grid box.

mated by CAM-MPAS over British Columbia in Canada (Fig. 11). The lead/lag correlations between the W-vector divergence averaged over British Columbia and *tas* errors in CAM-MPAS exhibit significant positive correlation in the same region, which also overlaps the overestimated *tas* variability by the same model (Fig. 4b). Across North America, the correlations show a wave-like structure resembling the Pacific-North America pattern, with significant correlations emerging over the Four Corners and Florida; however, those areas do not show systematic *tas* errors in the mean or standard deviations. Part of these *tas* errors is attributable to out-of-sync temporal evolutions between ERA-Interim and global, free-running CAM-MPAS, which has its own internal variabilities. Nonetheless, this result suggests error propagation from the biased mean wind patterns through erroneous propagations and convergence of Rossby waves WA to errors in the modeled *tas*.





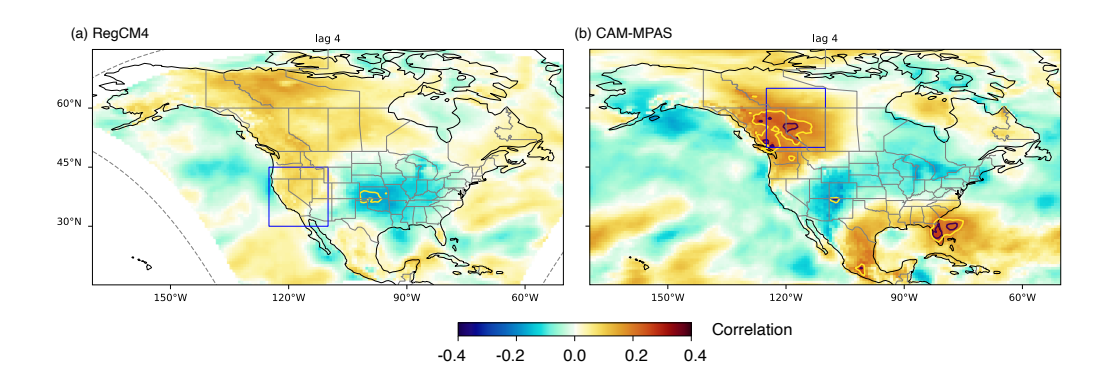


Figure 14. Similar to Fig. 13, but for the lead-lag correlations between the W-vector divergence averaged over the West Coast region in RegCM4 (a) and Canadian Pacific Northwest region in CAM-MPAS (b) and the simulation errors (model minus ERA-Interim) in the five-day running mean (*tas*) at each grid box.

3.5 Rossby wave and heatwaves

535

540

545

550

555

In this final subsection, we demonstrate a connection between stationary Rossby wave forcing and heatwave (HW) events, and assess how the downscaling simulations replicate the connection identified in ERA-Interim. We diagnose HW events using the criteria outlined in Barriopedro et al. (2023) (their Appendix A2). Specifically, an HW event is a period of three or more consecutive days with the daily maximum *tas* exceeding the 95th percentile of the reference period (1981-2010, except for CAM-MPAS, for which we use 1990-2010). All seasons are included in HW identification, and the seasonal cycle is not removed; thus, this criterion favors warm-season occurrences (Barriopedro et al., 2023). Figure 15a shows the spatial distributions of the average fraction of HW days per JJA season (i.e., the number of HW days during one JJA season = 92 days). ERA-Interim indicates two local maxima, one over the southwestern U.S. and the other over the SGP, where $\approx 15 \%$ of JJA days, or about 14 HW days, are expected each summer.

The same HW definition is applied to the downscaling simulations, also shown in Fig. 15. CAM-MPAS is able to simulate the overall spatial patterns with two local maxima over the southwestern and south-central U.S., but overestimates the number of HW days during the summer across most of North America, except in the eastern part, where it simulates fewer HW events. RegCM4 also simulates too many HWs in the JJA season across North America, except for SGP, where it underestimates the number. The HW distributions simulated by WRF agree best with those in ERA-Interim.

How does the HW distribution change during the days with strong Rossby wave forcing? We examine the days when the WA flux convergence $(-\nabla \cdot \mathbf{W})$ over the West Coast region (the same region used for the lead/lag correlations) exceeds the top 90th percentile of all years. The bar graphs in Fig. 16 show how those extreme days are distributed across years. Those top 10 percentiles are not uniformly distributed but instead exhibit variability on a 3–4 year timescale, according to the ERA-Interim data. A notable absence of extreme convergence days from 2004 to 2008 is followed by an abnormally high peak in 2009 (Fig. 16a), when unusually persistent upper-level circulations brought intense HWs to the Pacific Northwest,



560

565



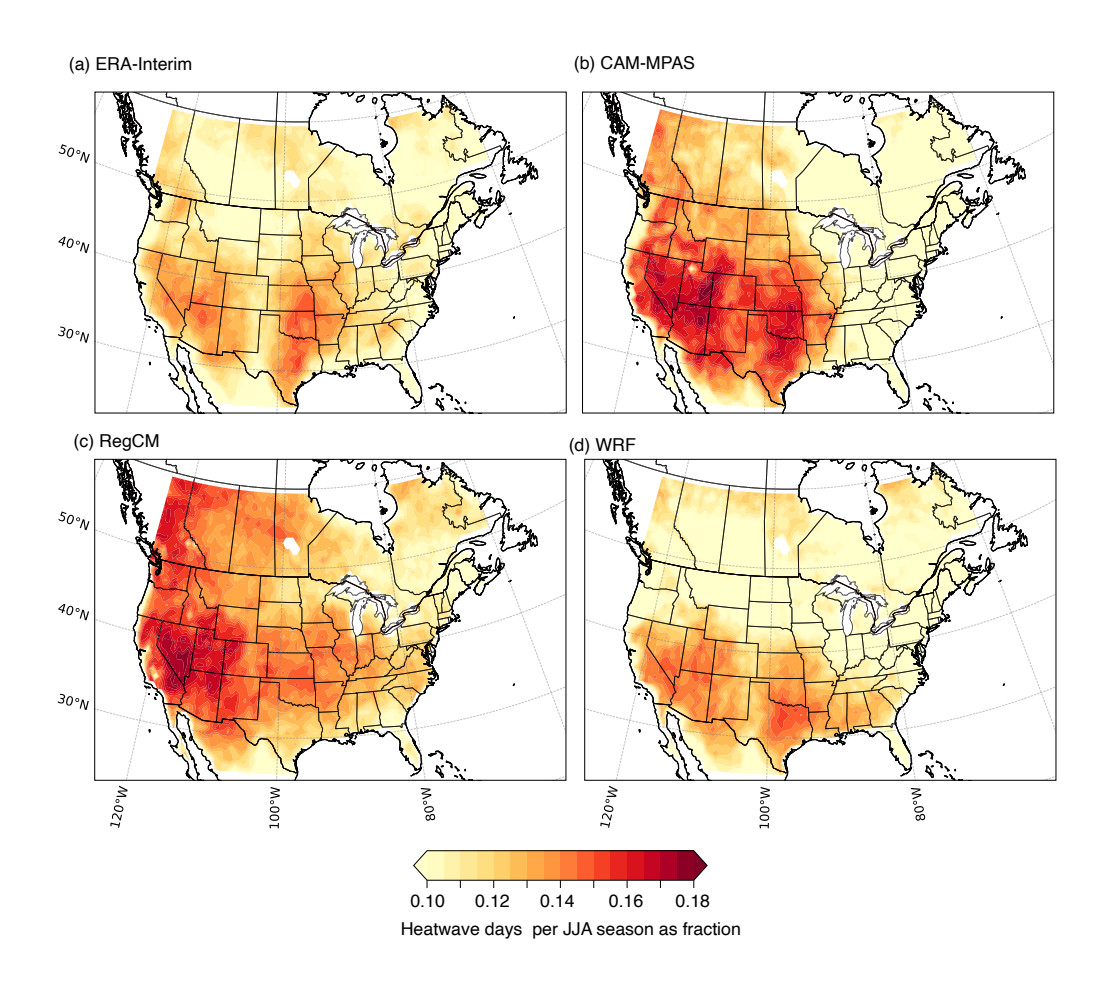


Figure 15. Fraction of the days (HW days per JJA (92) days) identified as HWs in (a) ERA-Interim, (b) CAM-MPAS, (c) RegCM4, and (d) WRF.

as illustrated in the Introduction. We expect LAMs to reproduce this temporal distribution reasonably well, since the western inflow boundary conditions provide the WA flux variability. Again, it is the case with WRF, but not necessarily with RegCM4 (Fig. 16c,d), although RegCM4 is able to capture the 2009 peak. Free-running CAM-MPAS does not simulate the 2009 peak or other clusters in sync with ERA-Interim (Fig. 16b), indicating the significant roles of biased waveguide locations and/or the atmosphere's internal variability on the WA flux variability, which is not well constrained by the prescribed SST. The spatial structure of the W-vector during the extreme case is generally similar to the climatological pattern (Fig. 11), so the model bias on the propagation pathways in the previous section applies to the extreme convergence days (not shown). In terms of the magnitude of extreme (top 10th percentile) W-vector convergence (indicated by the black markers in the figure), all models agree well with ERA-Interim: the average magnitude of the extreme convergence is -27, -26, -27, and -25 $(10^{-8} \ m^2 \ s^{-1})$ in ERA-Interim, CAM-MPAS, RegCM4, and WRF, respectively.







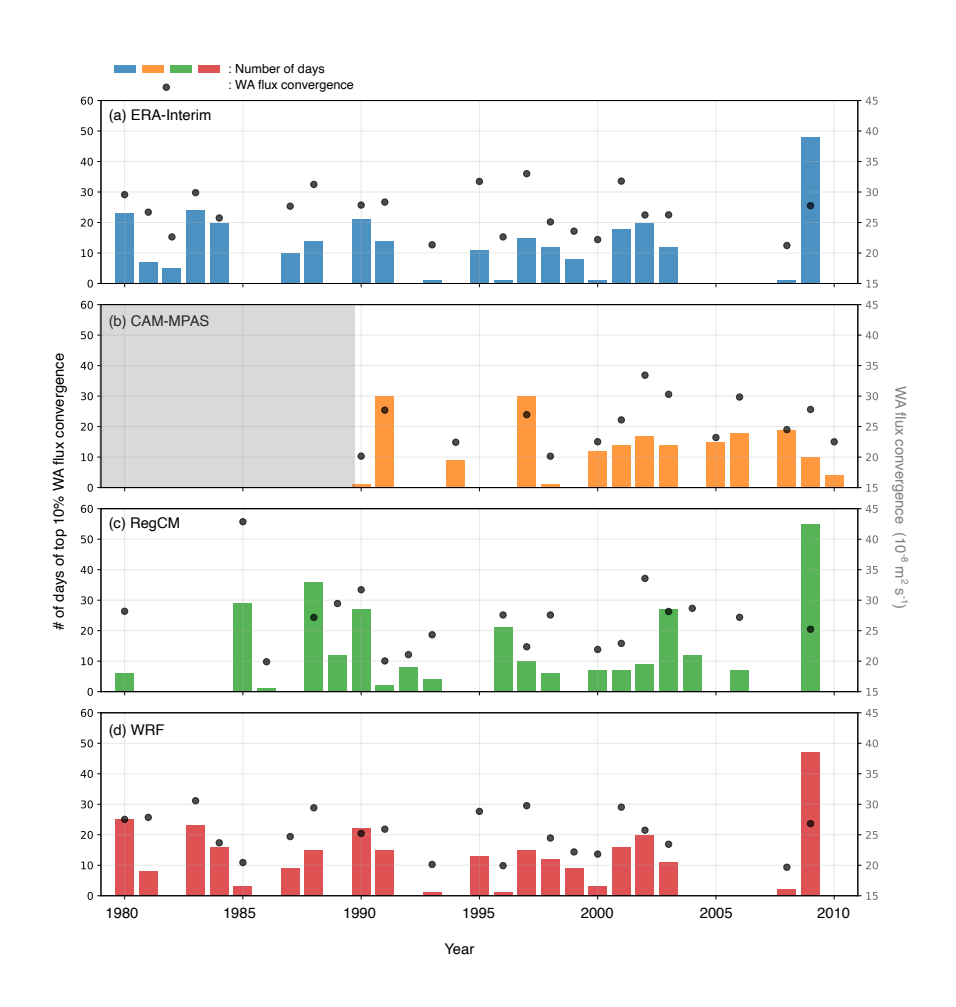


Figure 16. The bar graphs with the left y-axis show the distribution of the number of days with the top 10 % strongest convergence of WA flux convergence over the West Coast area (blue boxes in Figs. 12 and 13) in (a) ERA-Interim, (b) CAM-MPAS, (c) RegCM4, and (d) WRF. The black circles represent the average magnitude of the extreme WA flux convergence in each JJA season, with the right y-axis. In panel (b), the first 10 years are grayed out since CAM-MPAS data are not available for this period.





Calculating the fraction of HW days only on the days with extreme W-Vector convergence over the West Coast area in the ERA-Interim data, we see significantly higher HW fractions over the Midwest and the South Central U.S. and southern Canadian Prairies, and lower fractions in the northern Canadian Prairies, Quebec, and the Southwestern U.S. (Fig. 17a). That is, extremely rapid accumulations of WA over the West Coast region have a statistically significant impact on HW occurrences over those broad regions across North America. Note that the HW fraction is roughly doubled over the Central Plains from $\approx 0.12 - -0.15$ with all the samples to $\approx 0.2 - -0.3$ during the extreme WA flux convergence. Examining the composite means of the HW day fractions in the downscaling simulations, the WRF simulation yields the best agreement with ERA-Interim, although it does not accurately capture the reduced HW occurrences over the southwestern U.S. In CAM-MPAS, the higher HW fractions are seen over British Columbia and Quebec, the Southwest, and some parts of the Great Plains. Those responses differ from what ERA-Interim describes, and are somewhat similar to the areas with overestimated variability of tas by CAM-MPAS (Fig. 4b). In RegCM4, HW surge with the extreme WA flux is more concentrated over the southern part of CONUS, possibly related to the more northerly WA flux downwind over the West Coast and Great Plains in RegCM4 compared to the easterly WA flux in ERA-Interim (those during the extreme convergence not shown, but similar to Fig. 11). More in-depth analysis is required to conclude how the modeled HW response to WA flux is linked to the overall mean and/or variability biases of tas. Nonetheless, this diagnosis reveals a connection between extreme Rossby wave forcing and the occurrence of HWs over North America, which is accurately reproduced only by the WRF model with spectral nudging.

4 Discussions

580

585

590

595

Before summarizing our main findings, we report preliminary investigations into two outstanding questions arising from the presented results. First is the reason for the striking differences between the two LAMs, RegCM4 and WRF, in the upper-level circulations and stationary Rossby waves presented above. The two differ in many ways: numerical grid discretizations, hydrotstatic vs. non-hydrostatic dynamical core, width and weight functions of the LB buffer zones, and every component of physics parameterizations (Tables 1 and B1). Here, we focus on the impact of spectral nudging adopted in the WRF simulation for NA-CORDEX. We conducted two sensitivity simulations with WRF version 4.6.1. The only difference between the two sensitivity simulations is whether spectral nudging is used ("Nudge") or not ("NoNudge"). The model configuration is identical to that used for the NA-CORDEX WRF simulations (Chang et al., 2015; Diez-Sierra et al., 2022a), except for using the hybrid sigma-pressure vertical coordinate that is the default option since WRF version 4.0, instead of the traditional sigma coordinate used in the NA-CORDEX simulation (Skamarock et al., 2019). It is not expected that the different vertical grid (with the same resolution) will impact the following result. Both simulations are initialized at 2010/03/01 00:00 UTC, and run for nine months to 2010/11/30 23:00 UTC. Only the results from the JJA months are presented. We need the periods before and after JJA to apply the 25-90-day band-pass filters to define the quasi-stationary perturbations, as done in the main result to calculate the W-vector.

Figure B4a,b compares the JJA-mean biases of the two simulations in *ua200* against ERA-Interim. Consistent with the main result, the Nudge experiment shows little difference from ERA-Interim, while NoNudge simulates a weaker and shifted



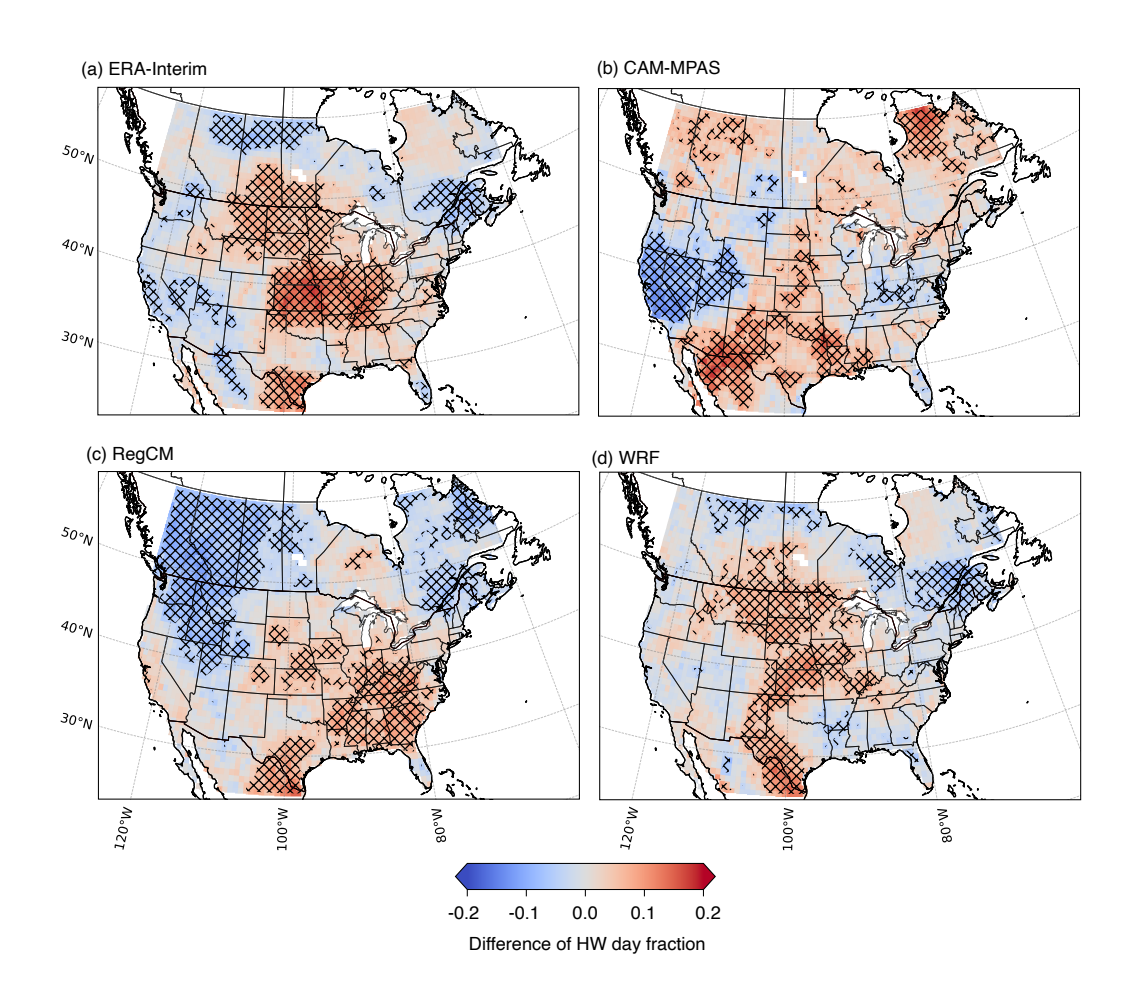


Figure 17. Difference in the fraction of the HW days, as the difference between the fraction calculated only during the extreme W-vector convergence over the Western Coast area and during the rest of the samples in (a) ERA-Interim, (b) CAM-MPAS, (c) RegCM4, and (d) WRF. The cross-hatch indicates that the difference is statistically significant at the 0.05 level.



600

605

620

625

630



mid-latitude jet during this particular summer. W-vector is calculated from the sensitivity simulations using the single-season JJA mean as the base state (Figure B4c,d). The NoNudge experiment produces artificial W-vector divergence/convergence pairs along the LBs, similar to the RegCM4 result, while the Nudge experiment shows no such artifacts. The two simulations exhibit distinct patterns of the W-vector convergence over the West Coast region, likely the combined result of the biased mid-latitude jet and artificial LB effect. In the Nudge experiment, the W-vector converges over a larger area that encompasses the Southwest, the northern Rockies, and the Pacific Northwest. On the other hand, the NoNudge simulation directs WA fluxes into lower latitudes with little convergence over the Pacific Northwest. Although the simulation length is limited for a rigorous evaluation of Rossby waves, the result strongly supports the notion that spectral nudging is the dominant factor in the differences between RegCM4 and WRF. This interpretation is consistent with previous studies demonstrating the effectiveness of spectral nudging in maintaining large-scale circulations from the forcing data and their impact on the near-surface climate. (Miguez-Macho et al., 2004; Alexandru et al., 2009; Castro et al., 2012).

Another question is the possibility of upscale effects on the mean winds simulated by CAM-MPAS and RegRM4 (Figs. 6 and B1). Both models simulate stronger southerly winds and weaker mid-latitude and subtropical jets off the West Coast of CONUS than in ERA-Interim, which direct Rossby waves northward to higher latitudes (Figs. 9 and 11). Since the two models have finer spatial resolutions than ERA-Interim, and their dynamics are not constrained by nudging, momentum and vorticity sources that are not well-resolved by ERA-Interim may be better represented by the two models. The impact of the Rockies and organized convection on Rossby waves over North America has been noted by previous studies (Ting, 1994; Stensrud, 2013; Rodwell et al., 2013).

The impact of different spatial resolutions can be assessed by comparing the more recent reanalysis product, ERA5 (Hersbach et al., 2020), to ERA-Interim, as ERA5 has a similar grid spacing to the models examined (≈ 25 km). The JJA-mean ua200 and zg200 from ERA5 are compared to those from ERA-Interim in Fig. B5a,b, from which it is clear that the resolution differences make negligible contributions to those mean fields. We also look at one-season average differences in va200 and zg200 between the NoNudge WRF simulation and ERA-Interim. If higher resolution is responsible for the upper-level wind differences, the NoNudge simulation might exhibit stronger southerly winds and a weaker jet, as in CAM-MPAS and RegCM4. Figures B4a and B5c,d tell us that this is not the case. The va200 difference shows weaker southerly winds off the West Coast in the WRF NoNudge experiment, which is the opposite of those by CAM-MPAS and RegCM4. The seasonal means of ua200 and zg200 in NoNudge do not exhibit the same spatial patterns as those in CAM-MPAS or RegCM4. Therefore, it is unlikely that physically oriented upscale effects are the main reasons for the mean circulation differences between ERA-Interim and the two models.

In our main results, quantifying large-scale biases is a common practice; we believe the novelty lies in tying circulation biases to stationary Rossby waves and further to near-surface air temperature and heatwaves. Some of the diagnostics we use could be helpful as part of climate model diagnostics packages (e.g., Eyring et al., 2020; Zhang et al., 2022; Stan et al., 2025). One use case is to identify GCMs with good skills in simulating wave sources and waveguides toward North America (e.g., (Goldenson et al., 2023)). Another application is obviously the evaluation of a dynamical downscaling framework, and we expect metrics to depend on the specific regions. For North America, we recommend using ray theory to track Rossby waves



635

640

645

650

655

660

665



from the North Pacific and the Eastern tropical/subtropical regions, which "translate" the biases in the mean circulation into the likelihood of Rossby wave propagations over North America. Another useful diagnosis is the divergence/convergence of WA flux over the West Coast. Among available WA formulations, the WA budget equation derived by TN01 does not require a time average to define the perturbation component. This means we can evaluate time series of W-vector convergence, which can then be correlated with other variables, such as *tas*.

Despite the insights we can gain from those diagnostics, they also have limitations that need to be overcome to become part of such diagnostic packages. As stated earlier, ray tracing involves integrating ordinary differential equations over time, which makes this technique computationally more intensive than typical evaluation metrics. W-vector diagnostics involve a more straightforward calculation, but their challenge lies in the complexity of the underlying theory rather than the numerical coding and data requirements for comprehensively analyzing three-dimensional budget terms. The LZ2015 ray theory also shares the former challenge of complexity in the underlying theory, but its publicly available repository includes documentation that clarifies how the model data is used by the diagnostics and references to relevant literature (Yang, 2025; Yang and Li, 2025). Other, simpler diagnostics exist for Rossby waves (e.g., Rossby wave sources and stationary wavenumber; see Appendix C), but they often involve more stringent assumptions, some of which may not be valid for studying regional climate. We hope this study provides valuable guidance, particularly for those interested in the North American climate.

Finally, all diagnostics we applied are based on the linear framework, thus excluding the effect of interactions with transient eddies (Teng et al., 2019) on stationary wave propagation, waves with finite (larger) amplitude Huang and Nakamura (2017), and eventual wave-breaking (Zhang and Wang, 2018), despite the crucial roles they play in extreme events (Nakamura and Huang, 2018; Chang et al., 2023b).

5 Conclusions

It is well known that not only global but also regional models exhibit warm *tas* bias during the summer over the central CONUS (Morcrette et al., 2018). While the role of physics parameterizations is significant on the surface warm bias, a recent study by Luo et al. (2022) found that biases in the upper-level stationary waves cause significant errors in the simulated surface temperature and precipitation. Investigating the sensitivity of WRF simulations to model resolution, convective parameterizations, and use of spectral nudging, (Gao et al., 2017) found that the SGP warm biases in the model are rather insensitive to the model resolution or the convective parameterization, but they were largely alleviated using spectral nudging that constrains the model to provide realistic moisture transport to the SGP region. Our results reiterate the importance of the model's ability to accurately simulate large-scale circulations, specifically the stationary Rossby wave, for dynamical downscaling over North America. We evaluate three distinct dynamical downscaling approaches to incorporate large-scale forcing: 1) a standard regional climate simulation with a LAM, represented by the RegCM4 simulation, 2) a LAM simulation with spectral nudging to constrain the large-scale atmospheric dynamics, represented by the WRF simulation, and 3) a global VR model that simulates large-scale circulations on its global grid. The first two model data are obtained from the NA-CORDEX model archive (Mearns et al., 2017), while the CAM-MPAS data is produced by our previous work following the NA-CORDEX protocol (Sakaguchi



680

685

690

695

700



et al., 2023). We evaluate the consistency of the large-scale circulations across the model domain boundaries by patching the LAM data and the driving data, ERA-Interim, onto a single global grid, on which the upper-level circulation and Rossby wave propagation are diagnosed.

We observe a striking contrast between RegCM4 and WRF in their consistency with the large-scale circulations of ERA-Interim. A pair of short WRF simulations with and without spectral nudging suggests that the spectral nudging applied in the NA-CORDEX WRF simulation is the primary reason for the difference between the two models. Specifically, in the RegCM4 simulation without spectral nudging, the mid-latitude and subtropical jets over the eastern North Pacific are weakened, and the time-mean geopotential patterns are shifted westward, resulting in stronger southerly meridional winds over the same region.

Furthermore, discontinuities in the time-mean circulation structure are apparent along LBs. The global model CAM-MPAS also suffers from mean circulation biases over the NA-CORDEX domain, featuring a weaker and northward-shifted mid-latitude jet, a weaker subtropical jet over the eastern North Pacific, and an overly strong positive geopotential anomaly that is centered over the Pacific Northwest, which also results in stronger southerly meridional winds over the West Coast area. CAM-MPAS's upper-level geopotential bias is found to overlap with the area of highest mean bias in tas.

A linear ray theory by LZ15 proves useful for linking those circulation biases to Rossby wave paths entering North America, owing to the relaxed assumption about the meridional winds in the mean background state. In the CAM-MPAS simulation, overestimated southerly winds and weaker zonal jets allow more Rossby waves to propagate northward from the low-latitude eastern Pacific to the Pacific Northwest, particularly to British Columbia. RegCM4 exhibits the same tendency as CAM-MPAS, overestimating the probability of Rossby wave passage over the Pacific Northwest and the eastern half of Canada. The WRF model with spectral nudging reproduces the Rossby wave propagation patterns in ERA-Interim.

Another diagnostic to complement the ray theory is the flux of kinetic energy and momentum flux associated with Rossby wave packets, combined as wave activity (WA). The formulation by TN01 (W-vector) also allows a non-uniform background state and non-zero meridional winds, showing WA propagation patterns consistent with the LZ15 ray theory. ERA-Interim suggests that WA flux tends to converge over the West Coast of North America, and the temporal evolution of WA flux convergence is correlated to that of *tas* anomaly over SGP. CAM-MPAS and RegCM4 cannot reproduce this correlation because of a biased mean circulation, leading to different Rossby wave propagation into North America: either to higher latitudes (CAM-MPAS) or at a different angle (RegCM4). We further find a relationship between extreme Rossby wave forcing (the top 10 percentile of WA flux convergence over the West Coast region) and HW occurrences across North America. This relationship is also not well simulated by CAM-MPAS and RegCM4.

The Rossby wave diagnostics used here translate large-scale circulation biases into Rossby wave propagation and their influence on the surface climate. This physical connection across space and scales is disrupted by biases in the mean circulation patterns in the global VR model, or by the failure to faithfully retain large-scale forcing in the LAM dynamical downscaling. For the large spatiotemporal scales of stationary Rossby waves, spectral nudging that constrains only the larger spatial scales helps the model reproduce nearly all aspects of Rossby wave dynamics and their impact on temperature anomalies across North America. The implications for dynamical downscaling over North America are: 1) the host GCMs and global VR models need to be able to simulate the wave sources in the eastern hemisphere (e.g., diabatic heating from organized convection) as well as



705

710



the mean wind patterns over the Pacific and North America to provide correct waveguide into North America and 2) Spectral nudging is beneficial for dynamical downscaling using LAMs to avoid numerical artifacts from the LB treatment on incoming Rossby waves as well as to maintain the large-scale circulation patterns on which Rossby waves propagate. Although our analysis focuses on the connection between Rossby waves and surface temperature, model biases in wave activity could also affect precipitation in the simulations, as seen in the common dry biases over the SGP. The latter can be further explored in the future using similar Rossby wave and wave activity diagnostics discussed in this study.

Code availability. The scripts used for post-processing, analysis, and visualization are available from the Zenodo archive at https://doi. org/10.5281/zenodo.17458434 (Sakaguchi, 2025). The LZ15 ray tracing code is updated by Yang and Li (2025) and available from https://github.com/yinan-codes/Rossby-wave-ray-tracing.

Data availability. The ERA-Interim (European Centre for Medium-Range Weather Forecasts, 2009) is available at https://doi.org/10.5065/D6SJ1JCH. The D6CR5RD9 on the NSF NCAR's Geodata Science Exchange, so are the NA-CORDEX data at https://doi.org/10.5065/D6SJ1JCH. The CAM-MPAS data is described at https://doi.org/10.25584/PNNL.data/1895153 and more easily downloadable through the National Energy Research Scientific Computing Center (NERSC) Science Gateway. The post-processed data used in the study is also available from the NERSC Science Gateway.





Appendix A: 2009 heatwave

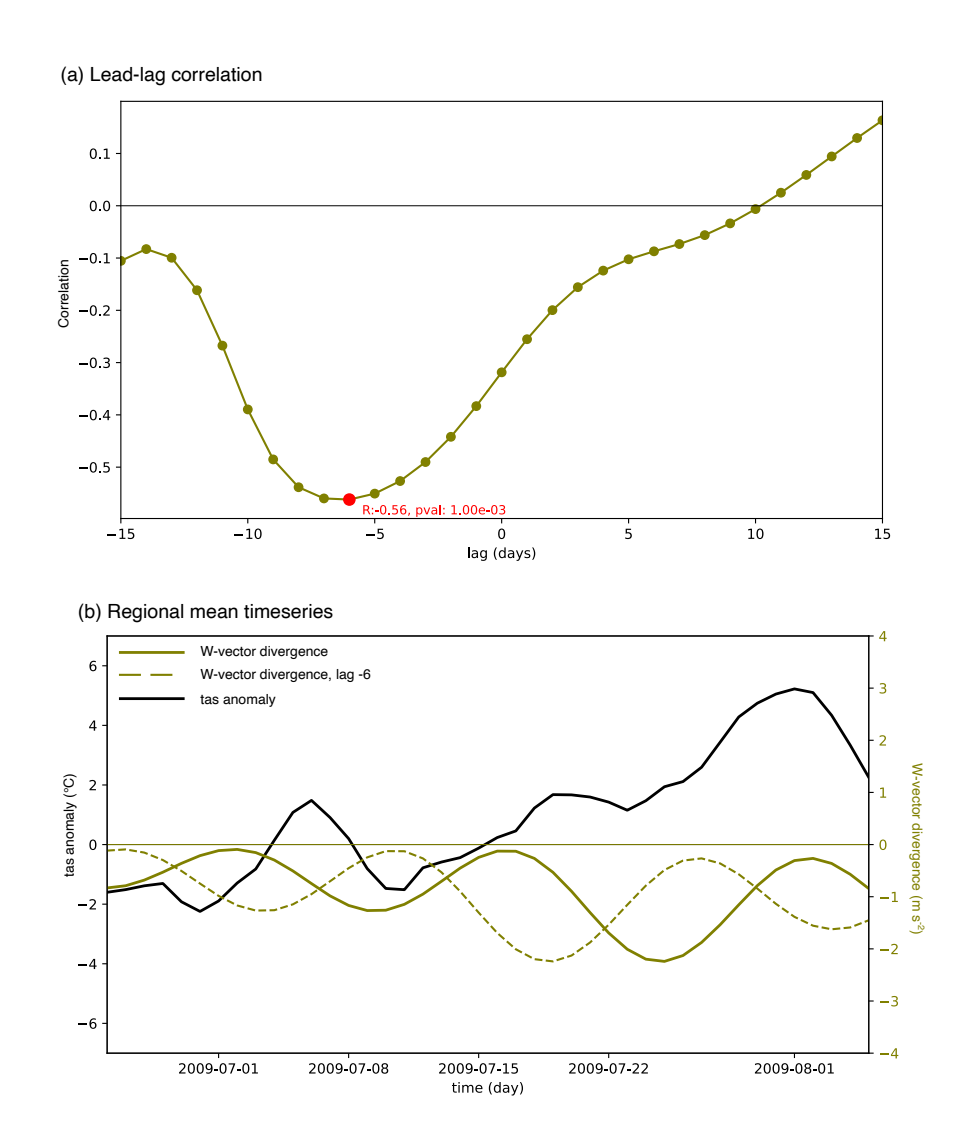


Figure A1. (a) lead-lag correlations between *tas* averaged over the Canada-U.S. Pacific Northwest [shown by a box with black dashed line Fig. 1g-h] and the divergence of WA flux averaged over the U.S. Pacific Northwest [the red dashed-line box in 1a-c] and (b) time series of the regional-average *tas* anomaly (black), WA flux divergence (green), and the WA flux divergence shifted by six days earlier, corresponding the lag -6 at which the lag correlation reaches the absolute maximum (the lowest negative correlation).





Appendix B: Additional information for model evaluations

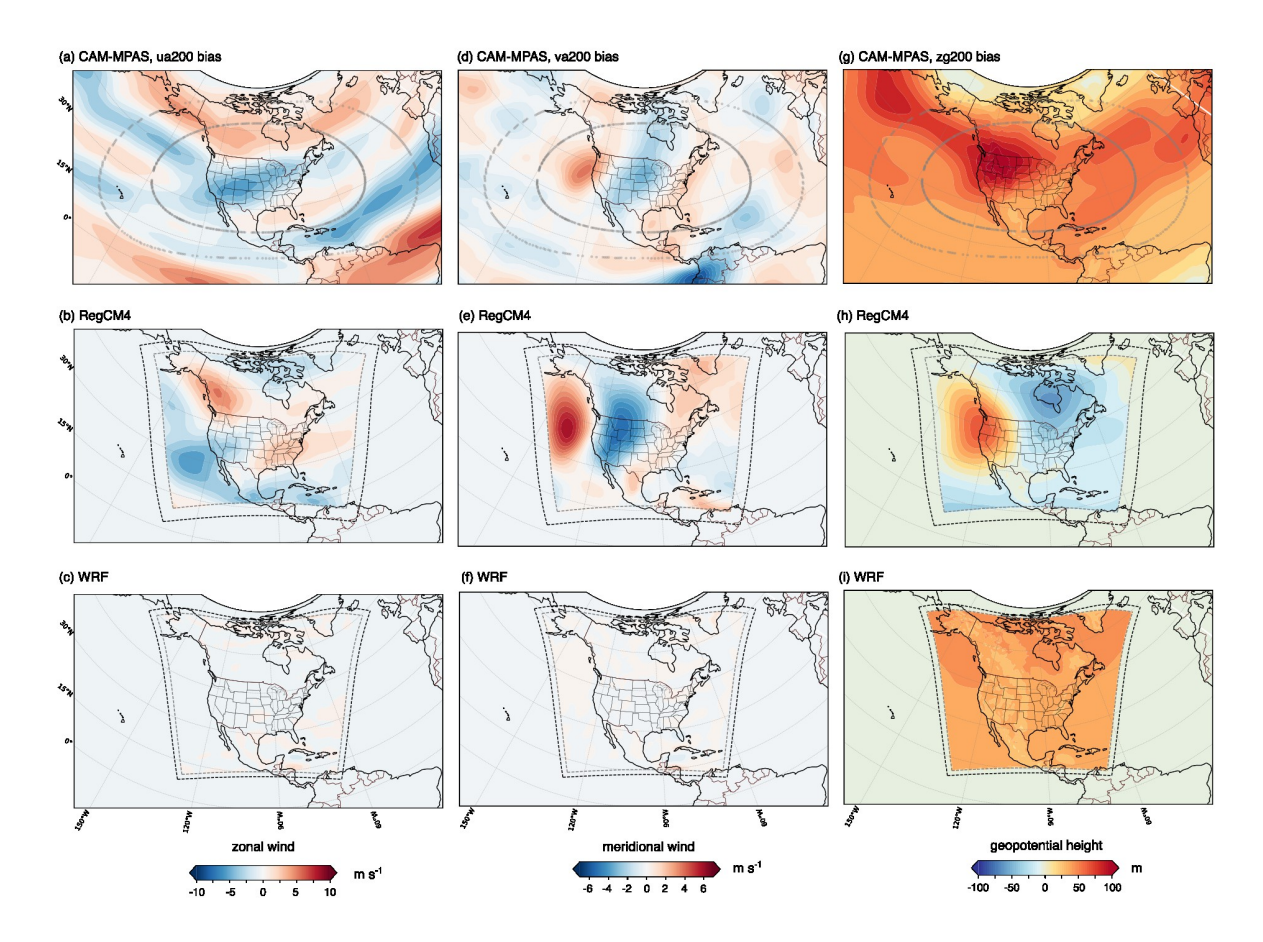


Figure B1. The JJA-mean zonal wind biases against ERA-Interim in (a) CAM-MPAS, (b) RegCM4, and (c) WRF. Corresponding meridional wind biases in (d, e, f) and geopotential biases in (g, h, i).



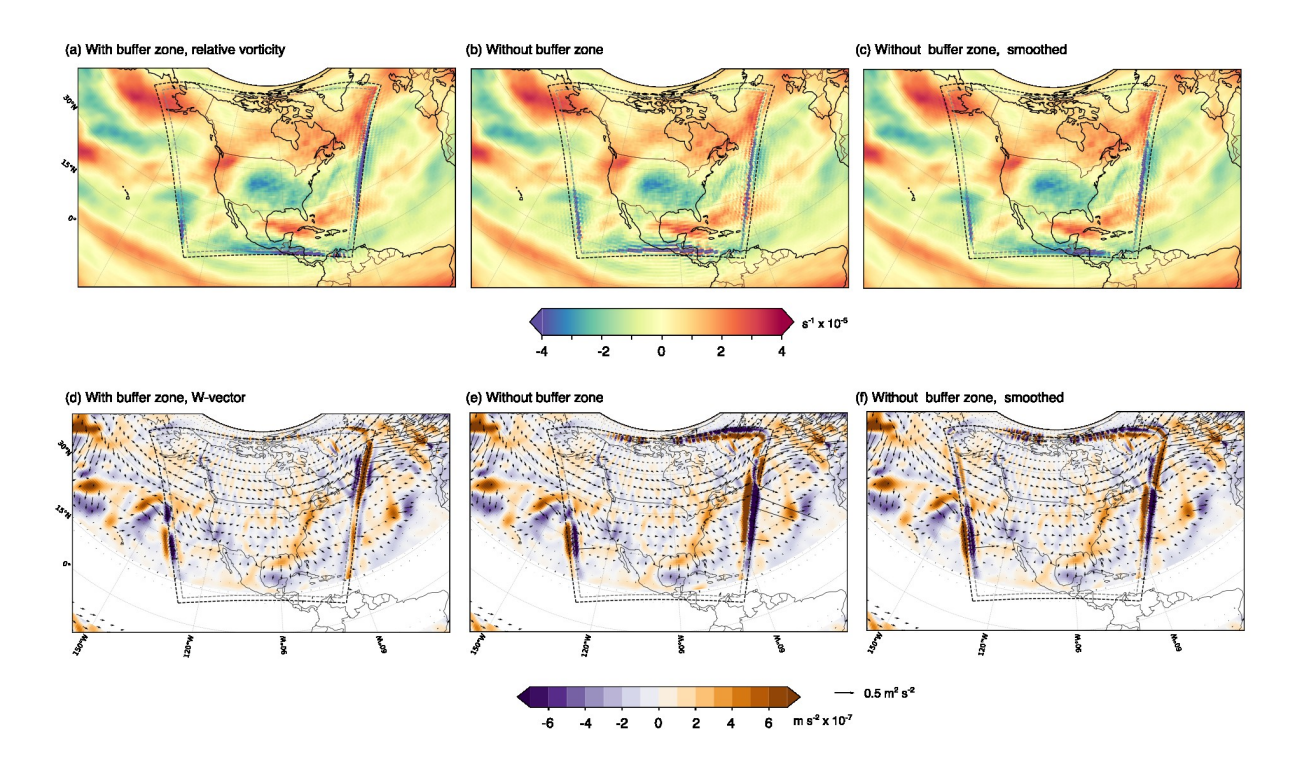


Figure B2. Illustration of the blending zone impact on derived diagnostics. The top row shows the JJA-mean vorticity calculated after remapping to the global grid and patching outside the domain with the ERA-Interim data, and bottom row shows W-vector and its divergence, using the model output with the buffer zone (a, d), without the buffer zone (b, d), and without buffer zone but Gaussian filter is applied to the (remapped) grid points located in the buffer zone (c, f).





Table B1. Physics parameterizations used in the three downscaling models. For the references for each parameterization, readers are referred to Diez-Sierra et al. (2022a) for RegCM4 and WRF, and Sakaguchi et al. (2023) for CAM-MPAS.

Component	RegCM4	WRF	CAM-MPAS
Land Surface	BATS	NOAH	CLM4
Subgrid land surface tiles	No	No	Yes
Boundary Layer	Modified Holtslag	MYJ	MU
Cloud microphysics	SUBEX	WSM3	MG2
Deep convection	Grell	Kain-Fritsch	Zhang-McFarlane
Shallow convection	ı	Kain-Fritsch	UW
Longwave Radiation	CAM	RRTM	RRTMG
Shortwave Radiation	CAM	Goddard	RRTMG
Aerosols	approprie	no aerosols	nrescribed





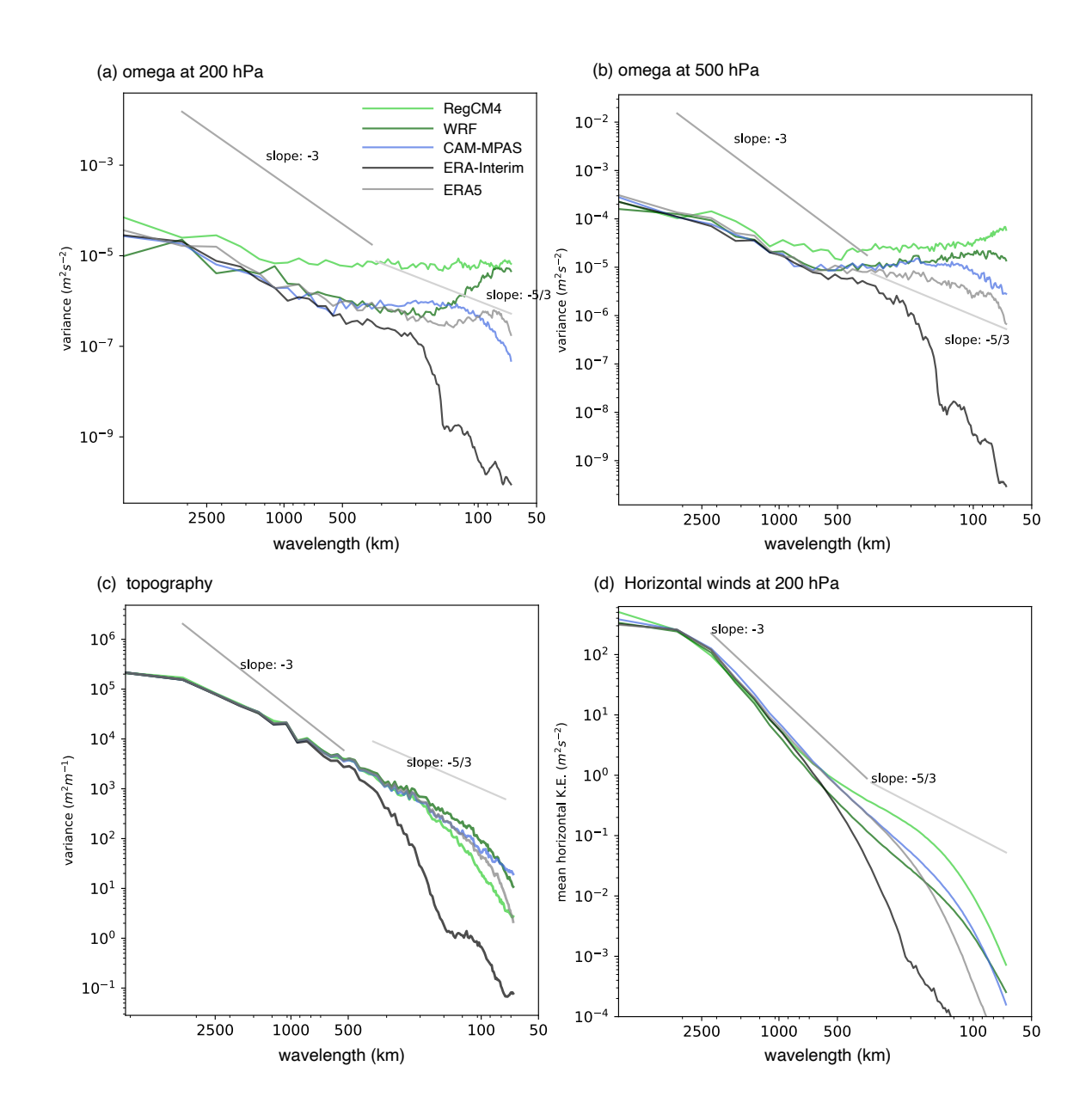


Figure B3. Power spectra of (a) pressure vertical velocity (ω , $Pa~s^{-1}$) at the 200 hPa level, (b) ω at 500 hPa, (c) surface topography, and (d) horizontal winds at the 200 hPa level. All variables are regridded to the WRF native grid with 25 km grid spacing, then the Discrete Cosine Transform is used to calculate the spectra (Denis et al., 2002a) .



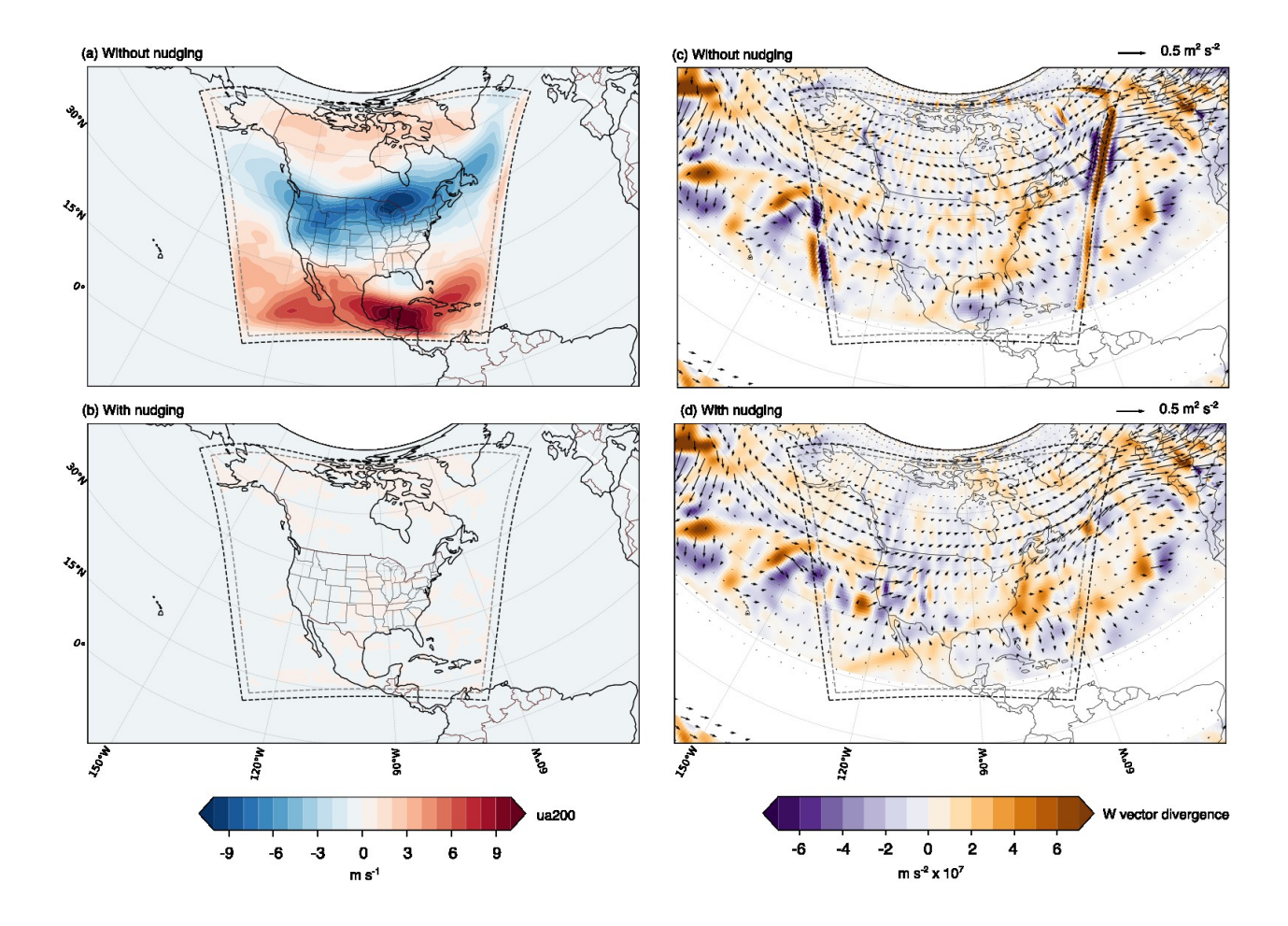


Figure B4. The effect of spectral nudging with the WRF model in the JJA-mean zonal wind bias against ERA-Interim (left column) and horizontal component of W-vector and its divergence (right column), all at the 200 hPa level: (a,c) without spectral nudging, (b, d) with spectral nudging.





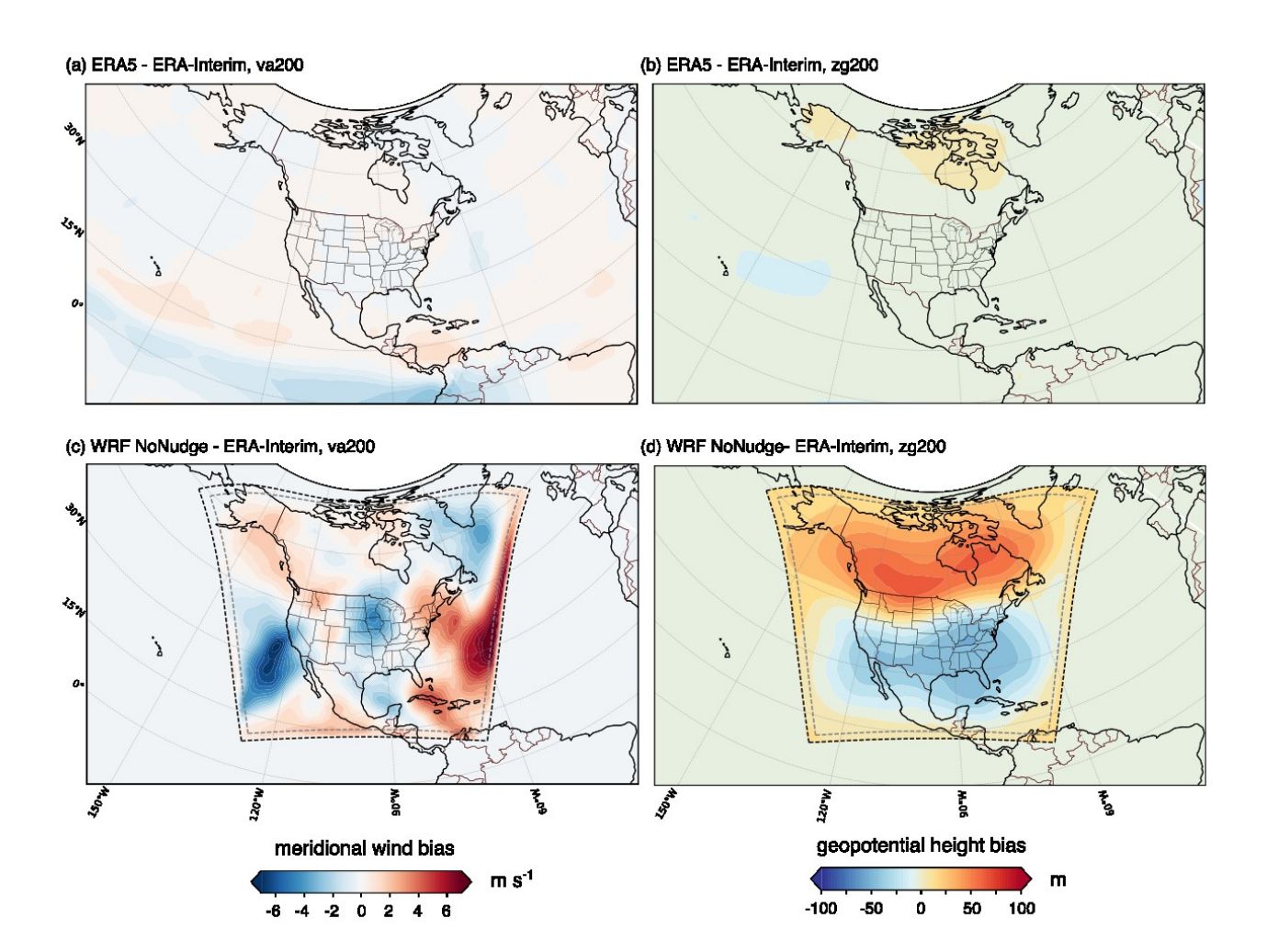


Figure B5. Differences between ERA5 and ERA-Interim in the JJA-mean (a) va200 and (b) zg200, as well as the differences between the WRF simulation without spectral nudging and ERA-Interim in (c) va200 and (d) zg200. The 1980-2010 JJA climatology is used in (a) and (b), while the 2010 JJA season only is used in (c) and (d).





B1 Lateral boundary treatment in RegCM4 and WRF

This subsection introduces the configurations of the LB buffer zone in the RegCM4 and WRF simulations for NA-CORDEX.

Both models follow the LB treatment proposed by Davies (1976), with several options for the shape and coefficients of the weighting functions to blend the model-predicted values and the large-scale forcing data. The RegCM4 and WRF simulations for NA-CORDEX differ in several of those options, as summarized below from Mearns et al. (2017) and Diez-Sierra et al. (2022a).

On the outermost grid point, referred to as the specified zone in Skamarock et al. (2008), all the prognostic variables are strictly those provided from the forcing data after interpolation in time and space (Fig. B6a). The specified zone is a single grid box in both RegCM4 and WRF simulations. The next n_{relax} grid points constitute the relaxation zone, where additional terms are included in the prognostic equations (eqn. 6 in Giorgi et al. (1993) and eqn. 6.1 in Skamarock et al. (2008)):

$$\left(\frac{\partial \alpha_m}{\partial t}\right)_n = (\text{advection, source/sinks, and other physical terms}) + \dots F(n)F_1(\alpha_f - \alpha_m) - F(n)F_2\nabla^2(\alpha_f - \alpha_m)$$
 (B1)

where α_m and α_f are the model-simulated and forcing values for a prognostic variable α , respectively, and n is the gridbox index from the boundary (n=1 for the specified zone, and $n=n_{spec}+n_{relax}$ for the last grid box within the relaxation zone). In this formulation, model-predicted values are relaxed toward the external data by Newtonian relaxation (the second-to-last term) and the differences between the modeled and large-scale forcing values are smoothed by the diffusion-like term (the last term).

 F_1 and F_2 are constants that depend on the timestep and grid spacing. F_1 is exactly the same in the two models as

735
$$F_1 = \frac{0.1}{\Delta t}$$

where Δt denotes the model time step (s). F_2 is slightly different; RegCM4 uses the following form

$$F_2 = \frac{(\Delta s)^2}{50\Delta t}$$

where Δs denotes the grid spacing (km). For WRF, it is given as

$$F_2 = \frac{1}{50\Delta t}$$

F(n) is a weighting function that gradually reduces its magnitude from the outer-most to the inner-most grid boxes within the relaxation zone. Both RegCM4 and WRF offer the options of linear and exponential functions. The WRF simulations for NA-CORDEX use a linear weighting function with $n_{spec} = 1$ and $n_{relax} = 10$:

$$F(n) = \frac{n_{spec} + n_{relax} - n}{n_{relax} - 1} = -\frac{11}{9}n$$

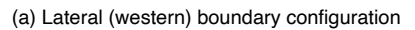
, while the RegCM4 simulations use an exponential function:

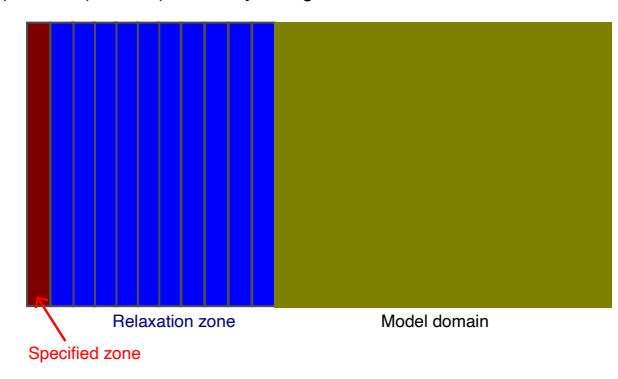
745
$$F(n) = exp\left(-\frac{(n-2)}{N_I}\right)$$
.

The coefficient $N_I = N_I(z)$ varies with height so that the model receives stronger large-scale forcing at higher altitudes (Giorgi et al., 1993). Fig. B6b shows three examples of RegCM4's exponential weight function for $N_I = 1, 3, 6$, along with the linear function in WRF.









(b) Weighing coefficients, F(n)

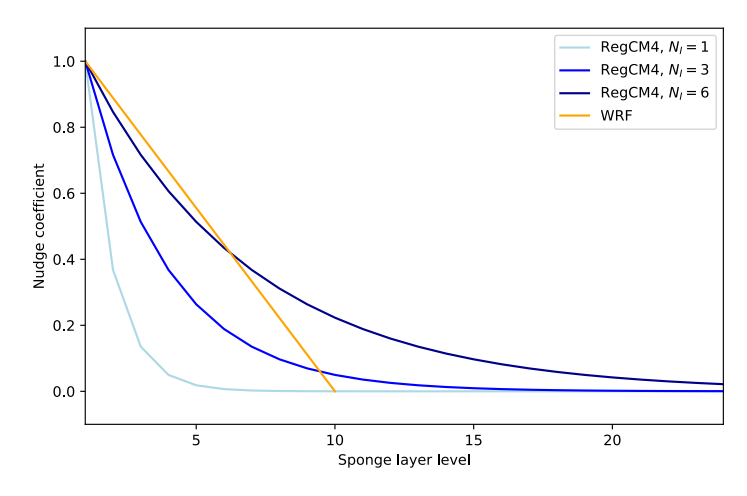


Figure B6. Illustration of the lateral boundary conditions in the RegCM4 and WRF configurations for NA-CORDEX: (a) an example configuration of specified and relaxation zones in the western boundary with $n_{relax} = 10$, and (b) weighting coefficients (F(n)) in RegCM4 and WRF. Three curves are shown for RegCM4 corresponding to $N_I = 1, 3, 6$.





Appendix C: Rossby wave

750 C1 Linear wave theory

We provide a brief review of the linear wave theory to help readers without a strong background in this topic understand the Rossby wave diagnostics. The materials follow sections 7.7 and 10.5 in Holton (2004), chapter 6 in Vallis (2017), and more complex cases in Li et al. (2015).

The dynamics of Rossby waves are studied in terms of the conservation law for quasi-geostrophic potential vorticity (e.g., Takaya and Nakamura, 2001; Li, 2020) since the restoring force for Rossby waves is the gradient of potential vorticity. For studying Rossby wave propagation in the atmosphere away from strong divergence, it is also common to use the vorticity equation in the barotropic atmosphere (i.e., a single layer with constant density in x and y, thus non-divergent circulations), which is:

$$\frac{\partial \eta}{\partial t} + u \frac{\partial \eta}{\partial x} + v \frac{\partial \eta}{\partial y} = 0 \tag{C1}$$

where η denotes the absolute vorticity $\eta = \zeta + f$, $f = 2\Omega \sin \phi$ is the Coriolis parameter, and ζ is the vertical component of relative vorticity. The friction is ignored. Strictly speaking, this single-level (barotropic or shallow-water) vorticity equation is applicable for the middle ($\langle \approx 300hPa \rangle$) or near the top of the troposphere ($>\approx 150hPa \rangle$), where wave structure is nearly vertically uniform (equivalent barotropic) (Sardeshmukh and Hoskins, 1988; Jin and Hoskins, 1995; Holton, 2004; Neduhal et al., 2024). At the same time, one needs to consider that outflows from the tropical convective systems to excite Rossby waves, and subsequent wave propagation to the middle latitudes, take place primarily in the upper troposphere ($\approx 100-300$ hPa) (Jin and Hoskins, 1995; Neduhal et al., 2024). Our analysis of the 200-hPa level is chosen primarily for the availability of high-frequency outputs from NA-CORDEX at three pressure levels: 200, 500, and 850 hPa (CORDEX, 2009), but it seems to be a reasonable compromise.

It is also common to use streamfunction, instead of vorticity, to study Rossby waves (Chen and Chen, 1990). The vorticity budget terms are noisy and not straightforward to visually interpret (Kang and Held, 1986). Streamfunction is a scalar from which rotational winds are obtained by differentiation:

$$u = -\frac{\partial \psi}{\partial y}$$

$$v = \frac{\partial \psi}{\partial x}$$
(C2)

, and we can write vorticity in terms of streamfunction

$$\zeta = \frac{\partial v}{\partial x} - \frac{\partial u}{\partial y}$$

$$= \frac{\partial^2 \psi}{\partial x^2} + \frac{\partial^2 \psi}{\partial y^2} = \nabla^2 \psi$$
(C3)

775 Then equation C1 becomes:

$$\left(\frac{\partial}{\partial t} + u\frac{\partial}{\partial x} + v\frac{\partial}{\partial y}\right)(\nabla^2 \psi + f) = 0 \tag{C4}$$





All the diagnostics we use are based on a linear perturbation framework, in which Rossby waves are defined as small perturbations (a') from the background (mean) state (\overline{a}):

$$u = \overline{u} + u'$$

$$v = \overline{v} + v'$$

$$\psi = \overline{\psi} + \psi'$$

$$\zeta = \overline{\zeta} + \zeta'$$

$$\overline{\zeta}_a = \overline{\zeta} + f = \nabla^2 \overline{\psi} + f$$
(C5)

780 then equation C4 becomes:

785

$$\left(\frac{\partial}{\partial t} + \overline{u}\frac{\partial}{\partial x} + \overline{v}\frac{\partial}{\partial y}\right)\nabla^2\psi' + u'\frac{\partial\nabla^2\overline{\psi} + f}{\partial x} + v'\frac{\partial\nabla^2\overline{\psi} + f}{\partial y} = 0$$

$$\left(\frac{\partial}{\partial t} + \overline{u}\frac{\partial}{\partial x} + \overline{v}\frac{\partial}{\partial y}\right)\nabla^2\psi' - \frac{\partial\psi'}{\partial y}\frac{\partial\overline{\zeta}_a}{\partial x} + \frac{\partial\psi'}{\partial x}\frac{\partial\overline{\zeta}_a}{\partial y} = 0.$$
(C6)

To study Rossby wave propagation from the source to remote locations, the above equation needs to be cast in spherical coordinates or other map projections to account for the Earth's spherical geometry. Here, we keep the simple Cartesian coordinates and refer the readers to previous studies for the equation in the appropriate coordinates (e.g., Hoskins and Karoly, 1981; Li et al., 2015). This partial differential equation for ψ' has parameters that vary in space, which prevents us from solving it analytically. To obtain an approximate analytical solution, we assume the mean state varies much more slowly than the wave disturbances, thus treating the mean state as constant locally (WKB approximation), and also assume plane wave solutions in the form of:

$$\psi' = A(X, Y, T) exp[i(kx + ly - \omega t)] \tag{C7}$$

where T, X, and Y are the local or wave-scale coordinates with substantially smaller scales of variations than those for the mean state (t, x, y). A is the amplitude, k is the zonal wavenumber, k is the meridional wavenumber, and k is the angular frequency. k is a function of time and space. By substituting equation C7 to equation C6, we can obtain the following dispersion relation:

$$\omega = \overline{u}k + \overline{v}l + \frac{\overline{\eta}_x l - \overline{\eta}_y k}{k^2 + l^2} \tag{C8}$$

where we have used subscripts x and y to denote partial differentiation with respect to x and y. Rearranging equation C8, we define the total wavenumber

$$K^2 = k^2 + l^2 = \frac{\overline{\eta}_y k - \overline{\eta}_x l}{\overline{u}k + \overline{v}l - \omega} \tag{C9}$$

For stationary waves with $\omega = 0$, the total wavenumber is

$$K^2 = k^2 + l^2 = \frac{\overline{\eta}_y k - \overline{\eta}_x l}{\overline{u}k + \overline{v}l} \tag{C10}$$



805

810



800 The x- and y-components of group velocity are obtained from the dispersion relationship (with the quotient rule of differentiation):

$$u_g = \frac{\partial \omega}{\partial k} = \overline{u} + \frac{((k^2 - l^2)\overline{q}_y - 2kl\overline{q}_x)}{K^4}$$

$$v_g = \frac{\partial \omega}{\partial l} = \overline{v} + \frac{2kl\overline{q}_y + (k^2 - l^2)\overline{q}_x}{K^4}$$
(C11)

Equation C10 tells that wavenumbers k and l depend on themselves and the mean state. Therefore, as a wave packet travels through a varying mean state, its wavenumbers also change. Their time evolution is governed by the conservation of the number of waves (Whitham, 1960):

If we assume that the background (mean) circulations are represented by the zonal mean zonal winds (constant over longitudes) and zero meridional winds, then the dispersion relationship is

$$\omega = \overline{u}k - \frac{\overline{\eta}_y k}{k^2 + l^2} \tag{C12}$$

and the group velocities are given by:

 $u_g = \overline{u} + \frac{2\overline{q}_y k^2}{K^2}$ $v_g = \frac{2\overline{q}_y k l}{K^2}.$ (C13)

For stationary waves $\omega = 0$ in this zonally uniform background case, we have a stationary wavenumber as

$$K_s^2 = \frac{\overline{\eta}_y}{\overline{u}}$$

, which is widely used in literature to depict Rossby waveguides (e.g., Hoskins and Ambrizzi, 1993; Henderson et al., 2017; Hoskins and Woollings, 2015).





815 C2 W vector

Based on the equations C2, C3, and C5, the horizontal component of the wave activity flux by TN01, or the "W-vector" are written as:

$$\mathbf{W}_{x} = \frac{1}{2|V|} \left[\overline{u} \left(\frac{\partial \psi'^{2}}{\partial x} - \psi' \frac{\partial^{2} \psi'}{\partial x^{2}} \right) + \overline{v} \left(\frac{\partial \psi'}{\partial x} \frac{\partial \psi'}{\partial y} - \psi' \frac{\partial^{2} \psi'}{\partial x \partial y} \right) \right]$$

$$\mathbf{W}_{y} = \frac{1}{2|V|} \left[\overline{u} \left(\frac{\partial \psi'}{\partial x} \frac{\partial \psi'}{\partial y} - \psi' \frac{\partial^{2} \psi'}{\partial x \partial y} \right) + \overline{v} \left(\frac{\partial \psi'^{2}}{\partial y} - \psi' \frac{\partial^{2} \psi'}{\partial y^{2}} \right) \right]$$
(C14)

where $|V| = \sqrt{\overline{u}^2 + \overline{v}^2}$. This is the form of W-vector on the pressure coordinate (eqn. C5 in TN01). Here, the mean winds (\overline{u} and \overline{v}) are the time-mean *geostrophic* winds, and the perturbation winds (and the associated streamfunction: u', v' and ψ') are the deviation of *geostrophic* winds from the mean winds.



825

830

835

845

850



C3 Sources of Rossby waves propagating to North America

To apply ray tracing in section 3.3, it is necessary to specify the locations of the wave sources. Following previous studies, we used lead/lag correlation maps of the daily mean perturbation meridional winds va200', using the same background state and the perturbation winds for the W-vector diagnosis. The base point is placed in one of the eight source regions: North Pacific, East Pacific, West Pacific, East Asian Monsoon, Indian Monsoon, Tibetan Plateau, Caspian Sea, and Red Sea. The time series of va200' after area-averaging over the base location (indicated by the box in Fig. C1) is correlated to the same variables at all the other grid points, varying the lags from -15 to +15 days.

Among the eight source locations examined, statistically significant correlations in the grid points over North America are found for the North Pacific and East Pacific (Fig. C1 a,b), suggesting that those two are the critical wave sources for stationary Rossby waves traveling to North America. However, the figure indicates other *indirect* wave sources from which wave signals reach those two sources. For example, from the East Asian Monsoon region (Fig. C1 d), statistically significant signals first appear to its west. The signal becomes stronger over three days, such that a statistically significant correlation links the East Asian region to Europe with a lag of -3. Then the signal in the downwind direction becomes strong and significant, reaching the North Pacific source region and almost the West Coast of North America (lags 0 and 3). Meanwhile, the wave signals from the Caspian Sea reach the East Asian region. A dipole wave pattern first establishes six days earlier (from day 0) over the Caspian Sea and Europe (Fig. C1 g, lag -6). Three days later (lag -3), another negative phase appears to the east, then another positive phase over China, reaching the East Asian Monsoon source.

Sardeshmukh and Hoskins (1988) suggested another diagnostic for Rossby wave sources. They linearized equation C1 to solve for the time tendency of perturbation absolute vorticity to identify the source terms. Doing so, they suggested to partition the winds into rotational (\mathbf{v}_{Ψ}) and divergent (\mathbf{v}_{χ}) components when diagnosing Rossby wave sources, particularly in the tropics, so that one does not overlook the contribution of vorticity advection by the divergent winds:

$$\frac{\partial \eta}{\partial t} + \mathbf{v}_{\Psi} \cdot \nabla \eta = -\mathbf{v}_{\chi} \cdot \nabla \eta - \eta \left(\nabla \cdot \mathbf{v}_{\chi} \right), \tag{C15}$$

where advection by the rotational and divergent winds is separated, and the latter is moved to the right-hand side as a forcing. Linearizing the equation, we have:

$$\frac{\partial \eta'}{\partial t} + \overline{\mathbf{v}}_{\Psi} \cdot \nabla \eta' + \mathbf{v'}_{\Psi} \cdot \nabla \overline{\eta} = -\nabla \cdot \left(\mathbf{v}_{\chi}' \overline{\eta}\right) - \nabla \cdot \left(\overline{\mathbf{v}}_{\chi} \eta'\right) \\
= -\overline{\eta} (\nabla \cdot \mathbf{v}_{\chi}') - \mathbf{v'}_{\chi} \cdot \nabla \overline{\eta} - \eta' (\nabla \cdot \overline{\mathbf{v}}_{\chi}) - \overline{\mathbf{v}}_{\chi} \cdot \nabla \eta' \tag{C16}$$

The left-hand side is the change of the perturbation absolute vorticity following the rotational winds. The right-hand side now has four terms: the first and third are stretching of the mean and perturbation vorticities by the perturbation and mean divergence, respectively. The second and fourth terms are the advection of the mean and perturbation vorticity by the perturbation and mean divergent winds, respectively. The right-hand-side terms are referred to as the Rossby Wave Source (RWS) (S'). Note that here RWS is defined for the perturbation vorticity, not the mean vorticity. Lin (2009) found the first two terms in the second line in eqn. C16 dominate other source terms. These are shown in Fig. C2, showing that all the source regions mentioned above exhibit strong magnitudes of either source term.





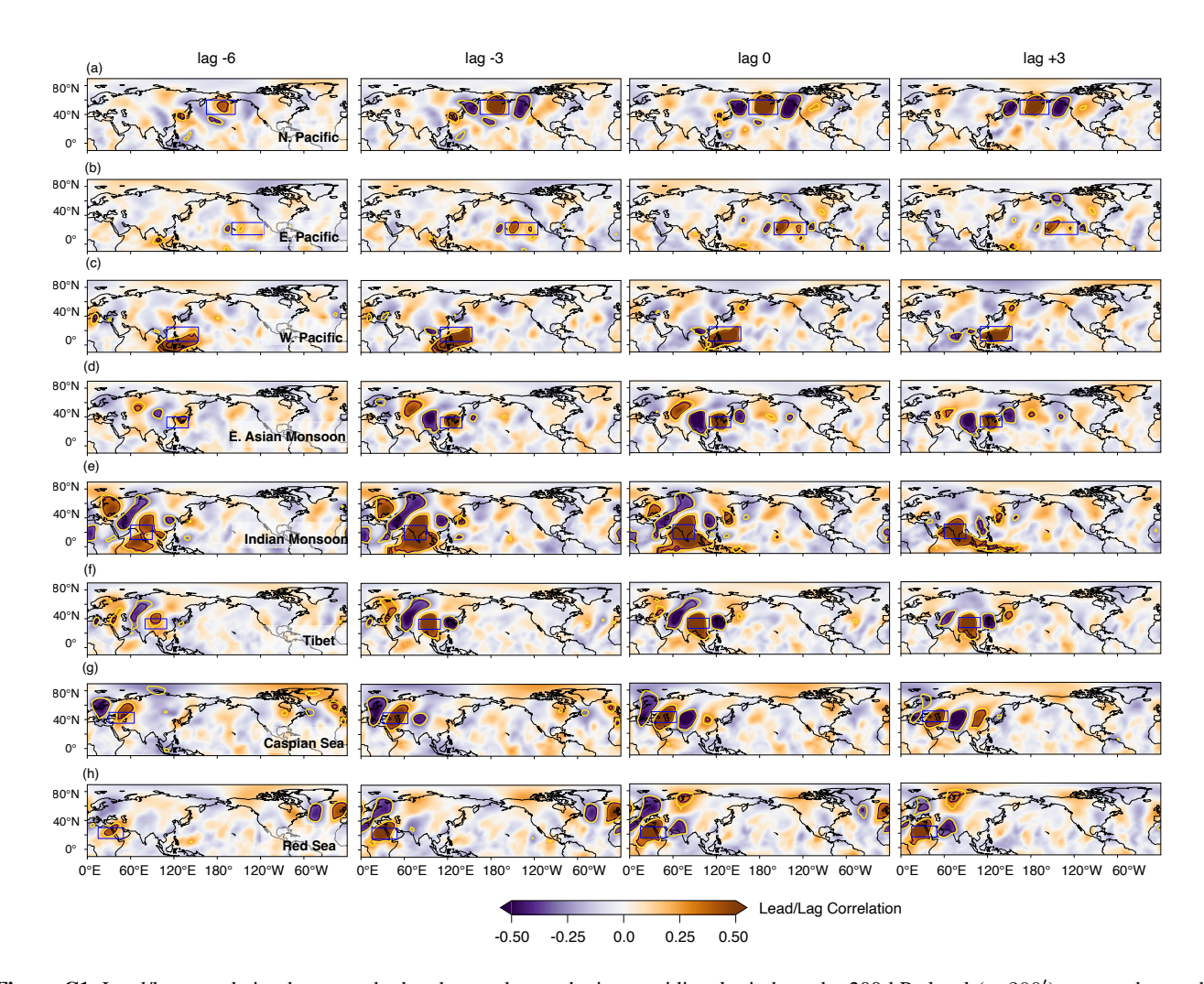


Figure C1. Lead/lag correlation between the band-passed perturbation meridional winds at the 200 hPa level (va200') averaged over the source regions (denoted by the blue rectangles) and all the other grid points. Each row represents different source locations: (a) North Pacific, (b) East Pacific, (c) West Pacific, (d) East Asian Monsoon, (e) Indian Monsoon, (f) Tibetan Plateau, (g) Caspian Sea, and (h) Red Sea.





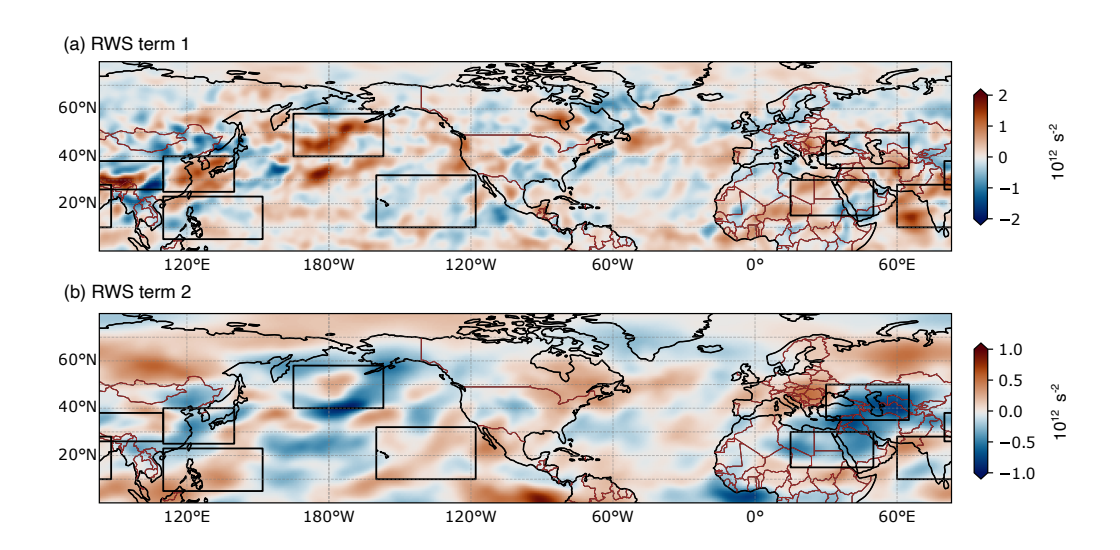


Figure C2. The first (a) and second (b) terms in the Rossby wave source (equation C16) calculated from ERA Interim



860

865



Author contributions. KS performed the analysis/plots and wrote the article. SM processed some of the model data and helped KS with coding and analysis. LRL supervised the work by providing general guidance for the article's direction and structure. MB provided technical information about the RegCM4 and WRF model configurations in the NA-CORDEX archive. SM, LRL, MB, and RM guided science questions and provided feedback on the analyses. ZC and CCC provided the technical background and literature on Rossby waves and their impact on extreme events. YL provided the ray tracing code and provided guidance on its use and interpretation. All authors reviewed and provided feedback on the article.

Competing interests. The authors declare that they have no conflict of interest.

Acknowledgements. This work is supported by the Department of Energy Office of Science award number DE-SC0016605, "A Framework for Improving Analysis and Modeling of Earth System and Intersectoral Dynamics at Regional Scales." We acknowledge the general direction and programmatic support from Dr. Linda Mearns, who deceased on January 23, 2025. This research used resources of the National Energy Research Scientific Computing Center, a DOE Office of Science User Facility supported by the Office of Science of the U.S. Department of Energy under Contract No. DE-AC02-05CH11231 using NERSC awards BER-ERCAP0024296 and BER-ERCAP0032096.





References

870

875

- Abatzoglou, J. T. and Magnusdottir, G.: Planetary Wave Breaking and Nonlinear Reflection: Seasonal Cycle and Interannual Variability, Journal of Climate, 19, 6139–6152, https://doi.org/10.1175/JCLI3968.1, 2006.
- Alexandru, A., de Elia, R., Laprise, R., Separovic, L., and Biner, S.: Sensitivity Study of Regional Climate Model Simulations to Large-Scale Nudging Parameters, Monthly Weather Review, 137, 1666–1686, https://doi.org/10.1175/2008MWR2620.1, 2009.
 - Ambrizzi, T., Hoskins, B. J., and Hsu, H.-H.: Rossby Wave Propagation and Teleconnection Patterns in the Austral Winter, Journal of the Atmospheric Sciences, 52, 3661–3672, https://doi.org/10.1175/1520-0469(1995)052<3661:RWPATP>2.0.CO;2, 1995.
 - Bacmeister, J. T., Wehner, M. F., Neale, R. B., Gettelman, A., Hannay, C., Lauritzen, P. H., Caron, J. M., and Truesdale, J. E.: Exploratory High-Resolution Climate Simulations Using the Community Atmosphere Model (CAM), Journal of Climate, 27, 3073–3099, https://doi.org/10.1175/JCLI-D-13-00387.1, 2014.
- Balaji, V., Boville, B., Cheung, S., Collins, N., Cruz, C., Silva, A., Deluca, C., Fainchtein, R. D., Eaton, B., Hallberg, B., Henderson, T., Hill, C., Iredell, M., Jacob, R., Jones, P., Kluzek, E., Kauffman, B., Larson, J., Li, P., Liu, F., Michalakes, J., Murphy, S., Neckels, D., Kuinghttons, R. O., Oehmke, B., Panaccione, C., Rosinski, J., Sawyer, W., Schwab, E., Smithline, S., Spector, W., Stark, D., Suarez, M., Swift, S., Theurich, G., Trayanov, A., Vasquez, S., Wolfe, J., Yang, W., Young, M., and Zaslavsky, L.: Earth System Modeling Framework ESMF Reference Manual for Fortran Version 7.1.0r, Tech. rep., The Earth System Modeling Framework, 2018.
- Barriopedro, D., García-Herrera, R., Ordóñez, C., Miralles, D. G., and Salcedo-Sanz, S.: Heat Waves: Physical Understanding and Scientific Challenges, Reviews of Geophysics, 61, e2022RG000780, https://doi.org/10.1029/2022RG000780, 2023.
- Bell, G. D. and Janowiak, J. E.: Atmospheric Circulation Associated With the Midwest Floods of 1993, Bulletin of the American Meteorological Society, 76, 681–696, 1995.
- Bogenschutz, P. A., Gettelman, A., Hannay, C., Larson, V. E., Neale, R. B., Craig, C., and Chen, C.-C.: The Path to CAM6: Coupled Simulations with CAM5.4 and CAM5.5, Geoscientific Model Development, 11, 235–255, https://doi.org/10.5194/gmd-11-235-2018, 2018.
 - Branstator, G.: Long-Lived Response of the Midlatitude Circulation and Storm Tracks to Pulses of Tropical Heating, Journal of Climate, 27, 8809–8826, https://doi.org/10.1175/JCLI-D-14-00312.1, 2014.
- Branstator, G. and Teng, H.: Tropospheric Waveguide Teleconnections and Their Seasonality, Journal of the Atmospheric Sciences, 74, 1513–1532, https://doi.org/10.1175/JAS-D-16-0305.1, 2017.
 - Bukovsky, M. S. and Mearns, L. O.: Regional Climate Change Projections from NA-CORDEX and Their Relation to Climate Sensitivity, Climatic Change, 162, 645–665, https://doi.org/10.1007/s10584-020-02835-x, 2020.
 - Bukovsky, M. S., McCrary, R. R., Seth, A., and Mearns, L. O.: A Mechanistically Credible, Poleward Shift in Warm-Season Precipitation Projected for the U.S. Southern Great Plains?, Journal of Climate, 30, 8275–8298, https://doi.org/10.1175/JCLI-D-16-0316.1, 2017.
- Bumbaco, K. A., Dello, K. D., and Bond, N. A.: History of Pacific Northwest Heat Waves: Synoptic Pattern and Trends, Journal of Applied Meteorology and Climatology, 52, 1618–1631, https://doi.org/10.1175/JAMC-D-12-094.1, 2013.
 - Castro, C. L., Pielke, R. A., and Leoncini, G.: Dynamical Downscaling: Assessment of Value Retained and Added Using the Regional Atmospheric Modeling System (RAMS), Journal of Geophysical Research D: Atmospheres, 110, 1–21, https://doi.org/10.1029/2004JD004721, 2005.
- Castro, C. L., Pielke, R. A., Adegoke, J. O., Schubert, S. D., and Pegion, P. J.: Investigation of the Summer Climate of the Contiguous United States and Mexico Using the Regional Atmospheric Modeling System (RAMS). Part II: Model Climate Variability, Journal of Climate, 20, 3866–3887, https://doi.org/10.1175/JCLI4212.1, 2007.



910



- Castro, C. L., Chang, H. I., Dominguez, F., Carrillo, C., Schemm, J. K., and Juang, H. M. H.: Can a Regional Climate Model Improve the Ability to Forecast the North American Monsoon?, Journal of Climate, 25, 8212–8237, https://doi.org/10.1175/JCLI-D-11-00441.1, 2012.
- Chang, C.-C., Lubis, S. W., Balaguru, K., Leung, L. R., Hagos, S. M., and Klotzbach, P. J.: An Extratropical Pathway for the Madden–Julian Oscillation's Influence on North Atlantic Tropical Cyclones, Journal of Climate, 36, 8539–8559, https://doi.org/10.1175/JCLI-D-23-0251.1, 2023a.
 - Chang, C.-C., Wang, Z., Ting, M., and Ming, Z.: Summertime Subtropical Stationary Waves in the Northern Hemisphere: Variability, Forcing Mechanisms, and Impacts on Tropical Cyclone Activity, Journal of Climate, 36, 753–773, https://doi.org/10.1175/JCLI-D-22-0233.1, 2023b.
 - Chang, C.-C., Zhao, M., Lubis, S. W., Chen, Z., Balaguru, K., Hagos, S., Leung, L. R., and Zhou, W.: Are North Atlantic Tropical Cyclones Modulated by the Madden–Julian Oscillation in HighResMIP AGCMs?, Journal of Climate, 38, 2891–2916, https://doi.org/10.1175/JCLI-D-24-0509.1, 2025.
- Chang, H.-i., Castro, C. L., Carrillo, C. M., and Dominguez, F.: The More Extreme Nature of U.S. Warm Season Climate in the Recent Observational Record and Two "Well-performing" Dynamically Downscaled CMIP3 Models, Journal of Geophysical Research: Atmospheres, 120, 8244–8263, https://doi.org/10.1002/2015JD023333, 2015.
 - Chen, T.-C. and Chen, J.-M.: On the Maintenance of Stationary Eddies in Terms of the Streamfunction Budget Analysis, Journal of the Atmospheric Sciences, 47, 2818–2824, 1990.
- Chen, X., Leung, L. R., Wigmosta, M., and Richmond, M.: Impact of Atmospheric Rivers on Surface Hydrological Processes in Western
 U.S. Watersheds, Journal of Geophysical Research: Atmospheres, 124, 8896–8916, https://doi.org/10.1029/2019JD030468, 2019.
 - Chen, Z., Lu, J., Chang, C. C., Lubis, S. W., and Leung, L. R.: Projected Increase in Summer Heat-Dome-like Stationary Waves over Northwestern North America, npj Climate and Atmospheric Science, 6, 1–10, https://doi.org/10.1038/s41612-023-00511-2, 2023.
 - Choi, N. and Stan, C.: Large-Scale Surface Air Temperature Bias in Summer over the CONUS and Its Relationship to Tropical Central Pacific Convection in the UFS Prototype 8, Journal of Climate, 38, 129, https://doi.org/10.1175/JCLI-D-24-0078.1, 2024.
- 925 CORDEX: Experiment Protocol CORDEX-CMIP5 RCMs, https://cordex.org/experiment-guidelines/cordex-cmip5/experiment-protocol-cordex-cmip5-rcms/, 2009.
 - Coumou, D., Petoukhov, V., Rahmstorf, S., Petri, S., and Schellnhuber, H. J.: Quasi-Resonant Circulation Regimes and Hemispheric Synchronization of Extreme Weather in Boreal Summer, Proceedings of the National Academy of Sciences of the United States of America, 111, 12331–12336, https://doi.org/10.1073/pnas.1412797111, 2014.
- 930 Dai, A.: Precipitation Characteristics in Eighteen Coupled Climate Models, Journal of Climate, 19, 4605–4630, 2006.
 - Davies, H. C.: A Lateral Boundary Formulation for Multi-Level Prediction Models, Quarterly Journal of the Royal Meteorological Society, 102, 405–418, 1976.
 - Denis, B., Côté, J., and Laprise, R.: Spectral Decomposition of Two-Dimensional Atmospheric Fields on Limited-Area Domains Using the Discrete Cosine Transform (DCT), Monthly Weather Review, 130, 1812–1829, https://doi.org/10.1175/1520-0493(2002)130<1812:SDOTDA>2.0.CO;2, 2002a.
 - Denis, B., Laprise, R., Caya, D., and Côté, J.: Downscaling Ability of One-Way Nested Regional Climate Models: The Big-Brother Experiment, Climate Dynamics, 18, 627–646, https://doi.org/10.1007/s00382-001-0201-0, 2002b.
 - Denis, B., Laprise, R., and Caya, D.: Sensitivity of a Regional Climate Model to the Resolution of the Lateral Boundary Conditions, Climate Dynamics, 20, 107–126, https://doi.org/10.1007/s00382-002-0264-6, 2003.





- Diez-Sierra, J., Iturbide, M., Gutiérrez, J. M., Fernández, J., Milovac, J., Cofiño, A. S., Cimadevilla, E., Nikulin, G., Levavasseur, G., 940 Kjellström, E., Bülow, K., Horányi, A., Brookshaw, A., García-Díez, M., Pérez, A., Baño-Medina, J., Ahrens, B., Alias, A., Ashfaq, M., Bukovsky, M., Buonomo, E., Cabos, W. D., Caluwaerts, S., Chou, S. C., Christensen, O. B., Ciarlò, J. M., Coppola, E., Corre, L., Demory, M.-E., Djurdjevic, V., Evans, J. P., Fealy, R., Feldmann, H., Jacob, D., Jayanarayanan, S., Katzfey, J., Keuler, K., Kittel, C., Kurnaz, M. L., Laprise, R., Lionello, P., McGinnis, S., Mercogliano, P., Nabat, P., Önol, B., Ozturk, T., Panitz, H.-J., Paquin, D., Pieczka, I., Raffaele, F., 945 Remedio, A. R., Scinocca, J., Sevault, F., Somot, S., Steger, C., Tangang, F., Teichmann, C., Termonia, P., Thatcher, M., Torma, C., van
- Meijgaard, E., Vautard, R., Warrach-Sagi, K., Winger, K., and Zittis, G.: CORDEX Model Component Description, 2022a.
 - Diez-Sierra, J., Iturbide, M., Gutiérrez, J. M., Fernández, J., Milovac, J., Cofiño, A. S., Cimadevilla, E., Nikulin, G., Levavasseur, G., Kjellström, E., Bülow, K., Horányi, A., Brookshaw, A., García-Díez, M., Pérez, A., Baño-Medina, J., Ahrens, B., Alias, A., Ashfaq, M., Bukovsky, M., Buonomo, E., Caluwaerts, S., Chou, S. C., Christensen, O. B., Ciarlò, J. M., Coppola, E., Corre, L., Demory, M.-E.,
- 950 Djurdjevic, V., Evans, J. P., Fealy, R., Feldmann, H., Jacob, D., Jayanarayanan, S., Katzfey, J., Keuler, K., Kittel, C., Kurnaz, M. L., Laprise, R., Lionello, P., McGinnis, S., Mercogliano, P., Nabat, P., Önol, B., Ozturk, T., Panitz, H.-J., Paquin, D., Pieczka, I., Raffaele, F., Remedio, A. R., Scinocca, J., Sevault, F., Somot, S., Steger, C., Tangang, F., Teichmann, C., Termonia, P., Thatcher, M., Torma, C., van Meijgaard, E., Vautard, R., Warrach-Sagi, K., Winger, K., and Zittis, G.: The Worldwide C3S CORDEX Grand Ensemble: A Major Contribution to Assess Regional Climate Change in the IPCC AR6 Atlas, Bulletin of the American Meteorological Society, 103, 955 E2804-E2826, https://doi.org/10.1175/BAMS-D-22-0111.1, 2022b.
 - Dimitrijevic, M. and Laprise, R.: Validation of the Nesting Technique in a Regional Climate Modeland Sensitivity Tests to the Resolution of the Lateral Boundary Conditionsduring Summer, Climate Dynamics, 25, 555-580, https://doi.org/10.1007/s00382-005-0023-6, 2005.
 - Ding, Q. and Wang, B.: Circumglobal Teleconnection in the Northern Hemisphere Summer, Journal of Climate, 18, 3483-3505, https://doi.org/10.1175/JCLI3473.1, 2005.
- European Centre for Medium-Range Weather Forecasts: ERA-Interim Project, https://doi.org/10.5065/D6CR5RD9, 2009. 960
 - Eyring, V., Bock, L., Lauer, A., Righi, M., Schlund, M., Andela, B., Arnone, E., Bellprat, O., Brötz, B., Caron, L.-P., Carvalhais, N., Cionni, I., Cortesi, N., Crezee, B., Davin, E. L., Davini, P., Debeire, K., de Mora, L., Deser, C., Docquier, D., Earnshaw, P., Ehbrecht, C., Gier, B. K., Gonzalez-Reviriego, N., Goodman, P., Hagemann, S., Hardiman, S., Hassler, B., Hunter, A., Kadow, C., Kindermann, S., Koirala, S., Koldunov, N., Lejeune, Q., Lembo, V., Lovato, T., Lucarini, V., Massonnet, F., Müller, B., Pandde, A., Pérez-Zanón, N., Phillips, A.,
- 965 Predoi, V., Russell, J., Sellar, A., Serva, F., Stacke, T., Swaminathan, R., Torralba, V., Vegas-Regidor, J., von Hardenberg, J., Weigel, K., and Zimmermann, K.: Earth System Model Evaluation Tool (ESMValTool) v2.0 - an Extended Set of Large-Scale Diagnostics for Quasi-Operational and Comprehensive Evaluation of Earth System Models in CMIP, Geoscientific Model Development, 13, 3383–3438, https://doi.org/10.5194/gmd-13-3383-2020, 2020.
- Gao, Y., Leung, L. R., Zhao, C., and Hagos, S.: Sensitivity of U.S. Summer Precipitation to Model Resolution and Convective Param-970 eterizations across Gray Zone Resolutions, Journal of Geophysical Research, 122, 2714-2733, https://doi.org/10.1002/2016JD025896, 2017.
 - Garfinkel, C. I., Chen, W., Li, Y., Schwartz, C., Yadav, P., and Domeisen, D.: The Winter North Pacific Teleconnection in Response to ENSO and the MJO in Operational Subseasonal Forecasting Models Is Too Weak, Journal of Climate, https://doi.org/10.1175/JCLI-D-22-0179.1,
- Giorgi, F. and Anyah, R. O.: The Road towards RegCM4, Climate Research, 52, 3-6, https://doi.org/10.3354/cr01089, 2012. 975



985



- Giorgi, F., Marinucci, M. R., Bates, G. T., and De Canio, G.: Development of a Second-Generation Regional Climate Model (RegCM2). Part II: Convective Processes and Assimilation of Lateral Boundary Conditions, Monthly Weather Review, 121, 2814–2832, https://doi.org/10.1175/1520-0493(1993)121<2814:DOASGR>2.0.CO;2, 1993.
- Giorgi, F., Coppola, E., Solmon, F., Mariotti, L., Sylla, M. B., Bi, X., Elguindi, N., Diro, G. T. G., Nair, V., Giuliani, G., Turuncoglu, U. U. U.,
 Cozzini, S., Güttler, I., O'Brien, T., Tawfik, A., Shalaby, A., Zakey, A., Steiner, A., Stordal, F., Sloan, L., and Brankovic, C.: RegCM4: Model Description and Preliminary Tests over Multiple CORDEX Domains, Climate Research, 52, 7–29, https://doi.org/10.3354/cr01018, 2012.
 - Goldenson, N., Leung, L. R., Mearns, L. O., Pierce, D. W., Reed, K. A., Simpson, I. R., Ullrich, P., Krantz, W., Hall, A., Jones, A., and Rahimi, S.: Use-Inspired, Process-Oriented GCM Selection: Prioritizing Models for Regional Dynamical Downscaling, Bulletin of the American Meteorological Society, 104, E1619–E1629, https://doi.org/10.1175/BAMS-D-23-0100.1, 2023.
 - Harvey, B. J., Cook, P., Shaffrey, L. C., and Schiemann, R.: The Response of the Northern Hemisphere Storm Tracks and Jet Streams to Climate Change in the CMIP3, CMIP5, and CMIP6 Climate Models, Journal of Geophysical Research: Atmospheres, 125, 1–10, https://doi.org/10.1029/2020JD032701, 2020.
- Henderson, S. A., Maloney, E. D., and Son, S.-W.: Madden–Julian Oscillation Pacific Teleconnections: The Impact of the Basic State and MJO Representation in General Circulation Models, Journal of Climate, 30, 4567–4587, https://doi.org/10.1175/JCLI-D-16-0789.1, 2017.
 - Hersbach, H., Bell, B., Berrisford, P., Hirahara, S., Horányi, A., Muñoz-Sabater, J., Nicolas, J., Peubey, C., Radu, R., Schepers, D., Simmons, A., Soci, C., Abdalla, S., Abellan, X., Balsamo, G., Bechtold, P., Biavati, G., Bidlot, J., Bonavita, M., De Chiara, G., Dahlgren, P., Dee, D., Diamantakis, M., Dragani, R., Flemming, J., Forbes, R., Fuentes, M., Geer, A., Haimberger, L., Healy, S., Hogan, R. J., Hólm, E., Janisková, M., Keeley, S., Laloyaux, P., Lopez, P., Lupu, C., Radnoti, G., de Rosnay, P., Rozum, I., Vamborg, F., Villaume, S., and Thépaut, J. N.: The ERA5 Global Reanalysis, Quarterly Journal of the Royal Meteorological Society, 146, 1999–2049, https://doi.org/10.1002/qj.3803, 2020.
 - Holman, K. D., Lorenz, D. J., and Notaro, M.: Influence of the Background State on Rossby Wave Propagation into the Great Lakes Region Based on Observations and Model Simulations, Journal of Climate, 27, 9302–9322, https://doi.org/10.1175/JCLI-D-13-00758.1, 2014.
- Holton, J. R.: An Introduction to Dynamic Meteorology, International Geophysics Series, Elsevier Academic Press, fourth edition edn.,

 ISBN 978-0-12-354015-7, 2004.
 - Hoskins, B. and Woollings, T.: Persistent Extratropical Regimes and Climate Extremes, Current Climate Change Reports, 1, 115–124, https://doi.org/10.1007/s40641-015-0020-8, 2015.
 - Hoskins, B. J. and Ambrizzi, T.: Rossby Wave Propagation on a Realistic Longitudinally Varing Flow, Journal of the Atmospheric Sciences, 50, 1661–1671, 1993.
- Hoskins, B. J. and Karoly, D. J.: The Steady Linear Response of a Spherical Atmosphere to Thermal and Orographic Forcing, Journal of the Atmospheric Sciences, 38, 1179–1196, 1981.
 - Hu, X.-M., Xue, M., McPherson, R. A., Martin, E., Rosendahl, D. H., and Qiao, L.: Precipitation Dynamical Downscaling Over the Great Plains, Journal of Advances in Modeling Earth Systems, 10, 421–447, https://doi.org/10.1002/2017MS001154, 2018.
- Huang, C. S. Y. and Nakamura, N.: Local Wave Activity Budgets of the Wintertime Northern Hemisphere: Implication for the Pacific and Atlantic Storm Tracks, Geophysical Research Letters, 44, 5673–5682, https://doi.org/10.1002/2017GL073760, 2017.
 - Imberger, M., Guo Larsén, X., Davis, N., and Du, J.: Approaches toward Improving the Modelling of Midlatitude Cyclones Entering at the Lateral Boundary Corner in the Limited Area WRF Model, Quarterly Journal of the Royal Meteorological Society, 146, 3225–3244, https://doi.org/10.1002/qj.3843, 2020.



1025

1040



- Jin, F. and Hoskins, B. J.: The Direct Response to Tropical Heating in a Baroclinic Atmosphere, Journal of Atmospheric Sciences, 52, 307–319, https://doi.org/10.1175/1520-0469(1995)052<0307:TDRTTH>2.0.CO;2, 1995.
 - Joseph, P. V. and Srinivasan, J.: Rossby Waves in May and the Indian Summer Monsoon Rainfall, Tellus A, 51, 854–864, https://doi.org/10.1034/j.1600-0870.1999.00021.x, 1999.
 - Kang, I.-S. and Held, I. M.: Linear and Nonlinear Diagnostic Models of Stationary Eddies in the Upper Troposphere during Northern Summer, Journal of the Atmospheric Sciences, 43, 3045–3057, 1986.
- 1020 Kornhuber, K., Petoukhov, V., Petri, S., Rahmstorf, S., and Coumou, D.: Evidence for Wave Resonance as a Key Mechanism for Generating High-Amplitude Quasi-Stationary Waves in Boreal Summer, Climate Dynamics, 49, 1961–1979, https://doi.org/10.1007/s00382-016-3399-6, 2017.
 - Laprise, R., de Elía, R., Caya, D., Biner, S., Lucas-Picher, P., Diaconescu, E., Leduc, M., Alexandru, a., and Separovic, L.: Challenging Some Tenets of Regional Climate Modelling, Meteorology and Atmospheric Physics, 100, 3–22, https://doi.org/10.1007/s00703-008-0292-9, 2008
 - Lau, K.-M. and Weng, H.: Recurrent Teleconnection Patterns Linking Summertime Precipitation Variability over East Asia and North America, Journal of the Meteorological Society of Japan. Ser. II, 80, 1309–1324, https://doi.org/10.2151/jmsj.80.1309, 2002.
 - Leung, L. R., Ringler, T. D., Collins, W. D., Taylor, M. A., Ashfaq, M., and Framework, A. H. E.: A Hierarchical Evaluation of Regional Climate Simulations, EOS, 94, 297–298, https://doi.org/10.1002/2013EO340001, 2013.
- 1030 Li, Y.: Enhanced Poleward Propagation of Barotropic Rossby Waves by the Free-Surface Divergent Effect, Scientific Online Letters on the Atmosphere, 16, 92–96, https://doi.org/10.2151/sola.2020-016, 2020.
 - Li, Y., Li, J., Jin, F. F., and Zhao, S.: Interhemispheric Propagation of Stationary Rossby Waves in a Horizontally Nonuniform Background Flow, Journal of the Atmospheric Sciences, 72, 3233–3256, https://doi.org/10.1175/JAS-D-14-0239.1, 2015.
- Li, Y., Feng, J., Li, J., and Hu, A.: Equatorial Windows and Barriers for Stationary Rossby Wave Propagation, Journal of Climate, 32, 6117–6135, https://doi.org/10.1175/JCLI-D-18-0722.1, 2019.
 - Lin, H.: Global Extratropical Response to Diabatic Heating Variability of the Asian Summer Monsoon, Journal of the Atmospheric Sciences, 66, 2697–2713, https://doi.org/10.1175/2009JAS3008.1, 2009.
 - Liu, C., Ikeda, K., Rasmussen, R., Barlage, M., Newman, A. J., Prein, A. F., Chen, F., Chen, L., Clark, M., Dai, A., Dudhia, J., Eidhammer, T., Gochis, D., Gutmann, E., Kurkute, S., Li, Y., Thompson, G., and Yates, D.: Continental-Scale Convection-Permitting Modeling of the Current and Future Climate of North America, Climate Dynamics, 49, 71–95, https://doi.org/10.1007/s00382-016-3327-9, 2017.
 - Lubis, S. W., Chen, Z., Lu, J., Hagos, S., Chang, C.-C., and Leung, L. R.: Enhanced Pacific Northwest Heat Extremes and Wildfire Risks Induced by the Boreal Summer Intraseasonal Oscillation, npj Climate and Atmospheric Science, 7, 232, https://doi.org/10.1038/s41612-024-00766-3, 2024.
- Luo, F., Selten, F., Wehrli, K., Kornhuber, K., Le Sager, P., May, W., Reerink, T., Seneviratne, S. I., Shiogama, H., Tokuda, D., Kim, H., and Coumou, D.: Summertime Rossby Waves in Climate Models: Substantial Biases in Surface Imprint Associated with Small Biases in Upper-Level Circulation, Weather and Climate Dynamics, 3, 905–935, https://doi.org/10.5194/wcd-3-905-2022, 2022.
 - Ma, H. Y., Klein, S. A., Xie, S., Zhang, C., Tang, S., Tang, Q., Morcrette, C. J., Van Weverberg, K., Petch, J., Ahlgrimm, M., Berg, L. K., Cheruy, F., Cole, J., Forbes, R., Gustafson, W. I., Huang, M., Liu, Y., Merryfield, W., Qian, Y., Roehrig, R., and Wang, Y. C.: CAUSES: On the Role of Surface Energy Budget Errors to the Warm Surface Air Temperature Error Over the Central United States, Journal of Geophysical Research: Atmospheres, 123, 2888–2909, https://doi.org/10.1002/2017JD027194, 2018.



1060



- Manola, I., Selten, F., De Vries, H., and Hazeleger, W.: "Waveguidability" of Idealized Jets, Journal of Geophysical Research Atmospheres, 118, 10,432–10,440, https://doi.org/10.1002/jgrd.50758, 2013.
- McGinnis, S. and Mearns, L.: Building a Climate Service for North America Based on the NA-CORDEX Data Archive, Climate Services, 22, 100 233, https://doi.org/10.1016/j.cliser.2021.100233, 2021.
- Mearns, L. O., McGinnis, S., Korytina, D., Scinocca, J. F., Kharin, S., Jiao, Y., Qian, M., Lazare, M., Winger, K., Christensen, O. B., Nikulin, G., Arritt, R. W., Herzmann, D., Bukovsky, M. S., Chang, H.-I., Castro, C., Frigon, A., and Gutowski, W. J. J.: The NA-CORDEX Dataset, Version 1.0., https://doi.org/10.5065/D6SJ1JCH, 2017.
 - Miguez-Macho, G., Stenchikov, G. L., and Robock, A.: Spectral Nudging to Eliminate the Effects of Domain Position and Geometry in Regional Climate Model Simulations, Journal of Geophysical Research D: Atmospheres, 109, 1–15, https://doi.org/10.1029/2003JD004495, 2004.
 - Morcrette, C. J., Van Weverberg, K., Ma, H. Y., Ahlgrimm, M., Bazile, E., Berg, L. K., Cheng, A., Cheruy, F., Cole, J., Forbes, R., Gustafson, W. I., Huang, M., Lee, W. S., Liu, Y., Mellul, L., Merryfield, W. J., Qian, Y., Roehrig, R., Wang, Y. C., Xie, S., Xu, K. M., Zhang, C., Klein, S., and Petch, J.: Introduction to CAUSES: Description of Weather and Climate Models and Their Near-Surface Temperature Errors in 5 Day Hindcasts Near the Southern Great Plains, Journal of Geophysical Research: Atmospheres, 123, 2655–2683, https://doi.org/10.1002/2017JD027199, 2018.
 - Nakamura, N. and Huang, C. S.: Atmospheric Blocking as a Traffic Jam in the Jet Stream, Science, 361, 42–47, https://doi.org/10.1126/science.aat0721, 2018.
 - NCAR: The NCAR Command Language, UCAR/NCAR/CISL/TDD, https://doi.org/10.5065/D6WD3XH5, 2017.
- Neduhal, V., Žagar, N., Lunkeit, F., Polichtchouk, I., and Zaplotnik, Ž.: Decomposition of the Horizontal Wind Divergence Associated With the Rossby, Mixed Rossby-Gravity, Inertia-Gravity, and Kelvin Waves on the Sphere, Journal of Geophysical Research: Atmospheres, 129, e2023JD040427, https://doi.org/10.1029/2023JD040427, 2024.
 - Nie, Y., Zhang, Y., Yang, X.-Q., and Ren, H.-L.: Winter and Summer Rossby Wave Sources in the CMIP5 Models, Earth and Space Science, 6, 1831–1846, https://doi.org/10.1029/2019EA000674, 2019.
- Park, H.-S., Xie, S.-P., and Son, S.-W.: Poleward Stationary Eddy Heat Transport by the Tibetan Plateau and Equatorward Shift of Westerlies during Northern Winter, Journal of the Atmospheric Sciences, 70, 3288–3301, https://doi.org/10.1175/JAS-D-13-039.1, 2013.
 - Park, M. and Lee, S.: Is the Stationary Wave Bias in CMIP5 Simulations Driven by Latent Heating Biases?, Geophysical Research Letters, 48, e2020GL091 678, https://doi.org/10.1029/2020GL091678, 2021.
- Park, S.-H., Klemp, J. B., and Skamarock, W. C.: A Comparison of Mesh Refinement in the Global MPAS-A and WRF Models Using an Idealized Normal-Mode Baroclinic Wave Simulation, Monthly Weather Review, 142, 3614–3634, https://doi.org/10.1175/MWR-D-14-00004.1, 2014.
 - Petoukhov, V., Rahmstorf, S., Petri, S., and Schellnhuber, H. J.: Quasiresonant Amplification of Planetary Waves and Recent Northern Hemisphere Weather Extremes, Proceedings of the National Academy of Sciences, 110, 5336–5341, https://doi.org/10.1073/pnas.1222000110, 2013.
- Pyper, B. J. and Peterman, R. M.: Comparison of Methods to Account for Autocorrelation in Correlation Analyses of Fish Data, Canadian Journal of Fisheries and Aquatic Sciences, 55, 2127–2140, https://doi.org/10.1139/f98-104, 1998.
 - Qin, H., Klein, S. A., Ma, H.-Y., Van Weverberg, K., Feng, Z., Chen, X., Best, M., Hu, H., Leung, L. R., Morcrette, C. J., Rumbold, H., and Webster, S.: Summertime Near-Surface Temperature Biases Over the Central United States in Convection-Permitting Simulations, Journal of Geophysical Research: Atmospheres, 128, e2023JD038 624, https://doi.org/10.1029/2023JD038624, 2023.



1095

1100



- Robock, A. and Mao, J.: The Volcanic Signal in Surface Temperature Observations, Journal of Climate, 8, 1086–1103, 1995.
- 1090 Rodwell, M. J. and Hoskins, B. J.: Monsoons and the Dynamics of Deserts, Quarterly Journal of the Royal Meteorological Society, 122, 1385–1404, 1996.
 - Rodwell, M. J., Magnusson, L., Bauer, P., Bechtold, P., Bonavita, M., Cardinali, C., Diamantakis, M., Earnshaw, P., Garcia-Mendez, A., Isaksen, L., Källén, E., Klocke, D., Lopez, P., McNally, T., Persson, A., Prates, F., and Wedi, N.: Characteristics of Occasional Poor Medium-Range Weather Forecasts for Europe, Bulletin of the American Meteorological Society, 94, 1393–1405, https://doi.org/10.1175/BAMS-D-12-00099.1, 2013.
 - Sakaguchi, K.: Scripts for Rossby Wave Evaluation of Dynamical Downscaling over North America, https://doi.org/10.5281/zenodo.17458434, 2025.
 - Sakaguchi, K., Lu, J., Leung, L. R., Zhao, C., Li, Y., and Hagos, S.: Sources and Pathways of the Upscale Effects on the Southern Hemisphere Jet in MPAS-CAM4 Variable-Resolution Simulations, Journal of Advances in Modeling Earth Systems, 8, 1786–1805, https://doi.org/doi:10.1002/2016MS000743., 2016.
 - Sakaguchi, K., Leung, L. R., Zarzycki, C. M., Jang, J., McGinnis, S., Harrop, B. E., Skamarock, W. C., Gettelman, A., Zhao, C., Gutowski, W. J., Leak, S., and Mearns, L.: Technical Descriptions of the Experimental Dynamical Downscaling Simulations over North America by the CAM–MPAS Variable-Resolution Model, Geoscientific Model Development, 16, 3029–3081, https://doi.org/10.5194/gmd-16-3029-2023, 2023.
- 1105 Sardeshmukh, P. D. and Hoskins, B. J.: The Generation of Global Rotational Flow by Steady Idealized Tropical Divergence, Journal of the Atmospheric Sciences, 45, 1228–1251, 1988.
 - Schneidereit, A., Schubert, S., Vargin, P., Lunkeit, F., Zhu, X., Peters, D. H. W., and Fraedrich, K.: Large-Scale Flow and the Long-Lasting Blocking High over Russia: Summer 2010, Monthly Weather Review, 140, 2967–2981, https://doi.org/10.1175/MWR-D-11-00249.1, 2012.
- 1110 Schubert, S., Wang, H., and Suarez, M.: Warm Season Subseasonal Variability and Climate Extremes in the Northern Hemisphere: The Role of Stationary Rossby Waves, Journal of Climate, 24, 4773–4792, https://doi.org/10.1175/JCLI-D-10-05035.1, 2011.
 - Simpson, I. R., Bacmeister, J., Neale, R. B., Hannay, C., Gettelman, A., Garcia, R. R., Lauritzen, P. H., Marsh, D. R., Mills, M. J., Medeiros, B., and Richter, J. H.: An Evaluation of the Large-Scale Atmospheric Circulation and Its Variability in CESM2 and Other CMIP Models, Journal of Geophysical Research: Atmospheres, 125, 1–42, https://doi.org/10.1029/2020JD032835, 2020.
- 1115 Skamarock, W. C., Klemp, J. B., Dudhi, J., Gill, D. O., Barker, D. M., Duda, M. G., Huang, X.-Y., Wang, W., and Powers, J. G.: A Description of the Advanced Research WRF Version 3, Tech. Rep. June, University Corporation for Atmospheric Research, Boulder, CO, United States, ISBN NCAR/TN-468+STR, ISSN 1477870X, https://doi.org/10.5065/D6DZ069T, 2008.
 - Skamarock, W. C., Klemp, J. B., Duda, M. G., Fowler, L. D., Park, S.-H., and Ringler, T. D.: A Multiscale Nonhydrostatic Atmospheric Model Using Centroidal Voronoi Tesselations and C-grid Staggering, Monthly Weather Review, 140, 3090–3105, https://doi.org/10.1175/MWR-D-11-00215.1, 2012.
 - Skamarock, W. C., Klemp, J. B., Dudhia, J., Gill, D. O., Liu, Z., Berner, J., Wang, W., Powers, J. G., Duda, M. G., Barker, D. M., and Huang, X.-Y.: A Description of the Advanced Research WRF Version 4, Tech. rep., National Center for Atmospheric Research, Boulder, Colo., 2019
- Srivastava, A. K., Ullrich, P. A., Rastogi, D., Vahmani, P., Jones, A., and Grotjahn, R.: Assessment of WRF (v 4.2.1) Dynamically Downscaled Precipitation on Subdaily and Daily Timescales over CONUS, Geoscientific Model Development, 16, 3699–3722, https://doi.org/10.5194/gmd-16-3699-2023, 2023.



1135



- Stan, C., Kollapaneni, S., Jenney, A., Wang, J., Wu, Z., Zheng, C., Kim, H., Garfinkel, C., and Singh, A.: A Python Diagnostics Package for Evaluation of MJO-Teleconnections in S2S Forecast Systems, EGUsphere, pp. 1–22, https://doi.org/10.5194/egusphere-2025-1142, 2025.
- Staniforth, A.: Meteorology and Atmospheric Physics Regional Modeling: A Theoretical Discussion, Meteorology and Atmospheric Physics, 63, 15–29, 1997.
 - Stensrud, D. J.: Upscale Effects of Deep Convection during the North American Monsoon, Journal of the Atmospheric Sciences, 70, 2681–2695, https://doi.org/10.1175/JAS-D-13-063.1, 2013.
 - Sy, S., Madonna, F., Serva, F., Diallo, I., and Quesada, B.: Assessment of NA-CORDEX Regional Climate Models, Reanalysis and in Situ Gridded-Observational Data Sets against the U.S. Climate Reference Network, International Journal of Climatology, 44, 305–327, https://doi.org/10.1002/joc.8331, 2024.
 - Takaya, K. and Nakamura, H.: A Formulation of a Wave-Activity Flux for Stationary Rossby Waves on a Zonally Varying Basic Flow, Geophysical Research Letters, 24, 2985–2988, https://doi.org/10.1029/97GL03094, 1997.
 - Takaya, K. and Nakamura, H.: A Formulation of a Phase-Independent Wave-Activity Flux for Stationary and Migratory Quasigeostrophic Eddies on a Zonally Varying Basic Flow, Journal of the Atmospheric Sciences, 58, 608–627, 2001.
- 1140 Teng, H. and Branstator, G.: Connections Between Heat Waves and Circumglobal Teleconnection Patterns in the Northern Hemisphere Summer, in: Climate Extremes, chap. 11, pp. 177–193, American Geophysical Union (AGU), ISBN 978-1-119-06802-0, https://doi.org/10.1002/9781119068020.ch11, 2017.
 - Teng, H. and Branstator, G.: Amplification of Waveguide Teleconnections in the Boreal Summer, Current Climate Change Reports, 5, 421–432, https://doi.org/10.1007/s40641-019-00150-x, 2019.
- Teng, H., Branstator, G., Wang, H., Meehl, G. A., and Washington, W. M.: Probability of US Heat Waves Affected by a Subseasonal Planetary Wave Pattern, Nature Geoscience, 6, 1056–1061, https://doi.org/10.1038/ngeo1988, 2013.
 - Teng, H., Branstator, G., Tawfik, A. B., and Callaghan, P.: Circumglobal Response to Prescribed Soil Moisture over North America, Journal of Climate, 32, 4525–4545, https://doi.org/10.1175/JCLI-D-18-0823.1, 2019.
- Ting, M.: Maintenance of Northern Summer Stationary Waves in a GCM, Journal of the Atmospheric Sciences, 51, 3286–3308, https://doi.org/10.1175/1520-0469(1994)051<3286:MONSSW>2.0.CO;2, 1994.
 - Trenberth, K. E., Branstator, G. W., Karoly, D., Kumar, A., Lau, N.-C., and Ropelewski, C.: Progress during TOGA in Understanding and Modeling Global Teleconnections Associated with Tropical Sea Surface Temperatures, Journal of Geophysical Research: Oceans, 103, 14291–14324, https://doi.org/10.1029/97JC01444, 1998.
- Vallis, G. K.: Atmospheric and Oceanic Fluid Dynamics, Cambridge University Press, 2nd edition edn., ISBN 978-1-107-06550-5, https://doi.org/10.1017/9781107588417, 2017.
 - Wallace, J. M. and Gutzler, D. S.: Teleconnections in the Geopotential Height Field during the Northern Hemisphere Winter, Monthly Weather Review, 109, 784–812, https://doi.org/10.1175/1520-0493(1981)109<0784:TITGHF>2.0.CO;2, 1981.
 - Wang, B., Wu, R., and Lau, K.-M.: Interannual Variability of the Asian Summer Monsoon: Contrasts between the Indian and the Western North Pacific–East Asian Monsoons, Journal of Climate, 14, 4073–4090, https://doi.org/10.1175/1520-0442(2001)014<4073:IVOTAS>2.0.CO;2, 2001.
 - Wang, Z., Chang, C.-P., and Wang, B.: Impacts of El Niño and La Niña on the U.S. Climate during Northern Summer, Journal of Climate, 20, 2165–2177, https://doi.org/10.1175/JCLI4118.1, 2007.
 - Wang, Z., Wu, R., Duan, A., and Qu, X.: Influence of Eastern Tibetan Plateau Spring Snow Cover on North American Air Temperature and Its Interdecadal Change, Journal of Climate, 33, 5123–5139, https://doi.org/10.1175/JCLI-D-19-0455.1, 2020.



1175



- Weaver, S. J. and Nigam, S.: Variability of the Great Plains Low-Level Jet: Large-Scale Circulation Context and Hydroclimate Impacts, Journal of Climate, 21, 1532–1551, https://doi.org/10.1175/2007JCLI1586.1, 2008.
 - White, R. H., Kornhuber, K., Martius, O., and Wirth, V.: From Atmospheric Waves to Heatwaves: A Waveguide Perspective for Understanding and Predicting Concurrent, Persistent, and Extreme Extratropical Weather, Bulletin of the American Meteorological Society, 103, E923–E935, https://doi.org/10.1175/BAMS-D-21-0170.1, 2022.
- White, R. H., Anderson, S., Booth, J. F., Braich, G., Draeger, C., Fei, C., Harley, C. D. G., Henderson, S. B., Jakob, M., Lau, C.-A., Mareshet Admasu, L., Narinesingh, V., Rodell, C., Roocroft, E., Weinberger, K. R., and West, G.: The Unprecedented Pacific Northwest Heatwave of June 2021, Nature Communications, 14, 727, https://doi.org/10.1038/s41467-023-36289-3, 2023.
 - Whitham, G. B.: A Note on Group Velocity, Journal of Fluid Mechanics, 9, 347–352, https://doi.org/10.1017/S0022112060001158, 1960.
 - Wills, R. C., White, R. H., and Levine, X. J.: Northern Hemisphere Stationary Waves in a Changing Climate, Current Climate Change Reports, 5, 372–389, https://doi.org/10.1007/s40641-019-00147-6, 2019.
 - Wirth, V.: Waveguidability of Idealized Midlatitude Jets and the Limitations of Ray Tracing Theory, Weather and Climate Dynamics, 1, 111–125, https://doi.org/10.5194/wcd-1-111-2020, 2020.
 - Wirth, V., Riemer, M., Chang, E. K. M., and Martius, O.: Rossby Wave Packets on the Midlatitude Waveguide—A Review, Monthly Weather Review, 146, 1965–2001, https://doi.org/10.1175/MWR-D-16-0483.1, 2018.
- Wolf, G., Brayshaw, D. J., Klingaman, N. P., and Czaja, A.: Quasi-Stationary Waves and Their Impact on European Weather and Extreme Events, Quarterly Journal of the Royal Meteorological Society, 144, 2431–2448, https://doi.org/10.1002/qj.3310, 2018.
 - Yang, Y.: Rossby Wave Ray Tracing and Ray Flux, 2025.
 - Yang, Y. and Li, J.: Novel Monsoon Indices Based on Vector Projection and Directed Angle for Measuring the East Asian Summer Monsoon, Climate Dynamics, 63, 210, https://doi.org/10.1007/s00382-025-07696-7, 2025.
- Yuan, J., Li, W., and Deng, Y.: Amplified Subtropical Stationary Waves in Boreal Summer and Their Implications for Regional Water Extremes, Environmental Research Letters, 10, 104 009, https://doi.org/10.1088/1748-9326/10/10/104009, 2015.
 - Zhang, C., Golaz, J.-C., Forsyth, R., Vo, T., Xie, S., Shaheen, Z., Potter, G. L., Asay-Davis, X. S., Zender, C. S., Lin, W., Chen, C.-C., Terai, C. R., Mahajan, S., Zhou, T., Balaguru, K., Tang, Q., Tao, C., Zhang, Y., Emmenegger, T., Burrows, S., and Ullrich, P. A.: The E3SM Diagnostics Package (E3SM Diags v2.7): A Python-based Diagnostics Package for Earth System Model Evaluation, Geoscientific Model Development, 15, 9031–9056, https://doi.org/10.5194/gmd-15-9031-2022, 2022.
 - Zhang, G. and Wang, Z.: North Atlantic Extratropical Rossby Wave Breaking during the Warm Season: Wave Life Cycle and Role of Diabatic Heating, Monthly Weather Review, 146, 695–712, https://doi.org/10.1175/MWR-D-17-0204.1, 2018.
 - Zhang, Y., Pan, Y., Xue, Y., Diallo, I., Zeng, X., Li, S., Neelin, J. D., Lau, W. K. M., Boone, A. A., Vitart, F., Yao, T., Tang, Q., Sato, T., Koo, M.-S., Ardilouze, C., Saha, S. K., Yang, J., Materia, S., Lin, Z., Qi, X., Qin, Y., Nakamura, T., Nobre, P., Peano, D., Senan, R., Takaya, Y.,
- Wang, H., Zhang, H., Zhan, Y., Zhao, M., Mechoso, C. R., Bao, Q., Bottino, M. J., Hong, S., Lin, Y., Xie, S., Pan, X., Nayak, H. P., Chou, S. C., and Guo, W.: Near-Global Summer Circulation Response to the Spring Surface Temperature Anomaly in Tibetan Plateau the GEWEX/LS4P First Phase Experiment, Climate Dynamics, 62, 2907–2924, https://doi.org/10.1007/s00382-024-07210-5, 2024.
 - Zhao, S., Li, J., and Li, Y.: Dynamics of an Interhemispheric Teleconnection across the Critical Latitude through a Southerly Duct during Boreal Winter, Journal of Climate, 28, 7437–7456, https://doi.org/10.1175/JCLI-D-14-00425.1, 2015.
- 1200 Zhou, W., Leung, L. R., and Lu, J.: Linking Large-Scale Double-ITCZ Bias to Local-Scale Drizzling Bias in Climate Models, Journal of Climate, 35, 7965–7979, https://doi.org/10.1175/JCLI-D-22-0336.1, 2022.





Zienkiewicz, O. C. and Zhu, J. Z.: Superconvergence and the Superconvergent Patch Recovery, Finite Elements in Analysis and Design, 19, 11–23, https://doi.org/10.1016/0168-874X(94)00054-J, 1995.